

Diss. ETH No. 18338

Large-scale imprinting of silver submicrometer structures and studies of their optical and mechanical properties

A dissertation submitted to the

ETH ZURICH

for the degree of

Doctor of Sciences

presented by

STEFANO BUZZI

Dipl. Ing. ETH

Born June 19th, 1979

citizen of Porza TI

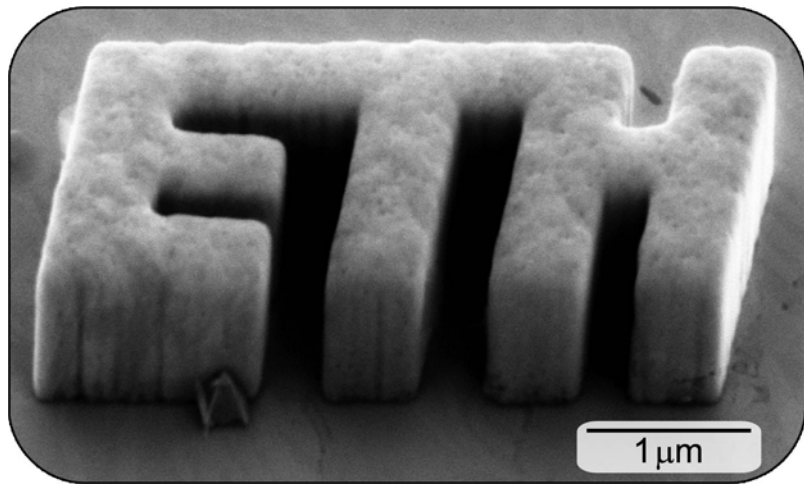
accepted on the recommendation of

Prof. Dr. Jörg F. Löffler, examiner

Prof. Dr. Ralph Spolenak, co-examiner

Prof. Dr. Cynthia A. Volkert, co-examiner

2009



Acknowledgments

I am grateful to Prof. Jörg F. Löffler for giving me the opportunity to spend the last few years in his group doing a Ph.D. on a very interesting topic, for his great confidence and guidance, and for the freedom he presented to me in determining some of my research directions.

I also would like to thank Prof. Cynthia A. Volkert and Prof. Ralph Spolenak for co-refereeing this work. Favored by the proximity of our offices, I could often profit from Prof. Spolenak's valuable suggestions during the course of the project.

All former and present members of the LMPT group contributed significantly to my indelible, positive memories of the last 4½ years at the Höggerberg. With them I shared both technical questions and my twin passions of mountaineering and photography. In particular, I am indebted to Erwin Fischer, who gave me invaluable technical support and was always ready to face new challenges with infectious enthusiasm; to Prof. Peter Uggowitzer, for very useful discussions; to Alberto Castellero, reliable partner both in the lab and on the mountains, and to Katherine Hahn Halbheer, who rendered my English texts more pleasant for the reader.

I have also enjoyed the support and friendship of several members of Prof. Spolenak's group; I should especially mention Marianne Dietiker and Flavio Mornaghini for the numerous hours they invested helping me.

Prof. Christian Hafner is acknowledged for initiating the INIT collaboration project, which was the motivation for starting this thesis and ensured part of its funding. Among the INIT partners, I benefited especially from decisive inputs by Franck Robin, Mario Agio and Victor Callegari. Karsten Kunze of EMEZ also played a crucial role in the EBSD analysis and the interpretation of its results.

Finally, sincere thanks go to my roommates, especially Seraina and Barbara, to Patrizia, and to my family for their continuous encouragement and serenity.

Contents

Acknowledgments	I
Summary	IV
Riassunto	VI
Zusammenfassung	VIII
1. Introduction	1
1.1. Motivation	1
1.2. Metal microfabrication techniques	3
1.2.1. Electroless metal deposition and electrodeposition	6
1.2.2. PVD: Physical vapor deposition (evaporation/sputtering)	7
1.2.3. CVD: Chemical vapor deposition	8
1.2.4. Microforming (nanoimprinting)	9
1.2.5. Other techniques	9
1.2.6. Selection of the fabrication method	11
1.3. Microforming (imprinting): State of the art	12
1.4. Scaling and size effects	17
1.5. Aims and outline of the thesis project	18
1.5.1. Development of the nanoimprinting process	19
1.5.2. Suitability for optical devices	19
1.5.3. Mechanical characterization of imprinted pillars	19
1.6. References	20
2. Microstructure characterization techniques	23
2.1. Scanning electron microscopy (SEM)	24
2.2. Electron backscattered diffraction (EBSD)	24
2.3. Focused ion beam (FIB)	24
2.4. Other techniques	25
3. Development of the nanoimprinting technique	26
3.1. Dielectric mold: material selection and fabrication procedure	27
3.2. Metal selection	29
3.3. Preliminary investigation of the necessary forming conditions (imprinting temperature)	31
3.4. Imprinting setup and metal plate preparation	34
3.5. Mold release	37
3.6. Removal of excess metal to produce Si – Ag photonic crystals	40
3.7. Nanoimprinting results (formability)	44
3.7.1. Obtained structures and potential of the nanoimprinting technique for large-scale production	44

3.7.2. Filling behavior	45
3.7.3. Texture in imprinted structures	47
3.8. Summary and review of best fabrication parameters	50
3.9. References	51
4. <i>Optical properties: Suitability of direct nanoimprinting for producing metal-containing optical devices</i>	53
4.1. Introduction	54
4.2. Experimental procedure	56
4.3. Results and discussion	57
4.4. Conclusions	67
4.5. References	67
5. <i>Mechanical properties: Deformation behavior of silver submicrometer-pillars prepared by nanoimprinting</i>	69
5.1. Introduction	70
5.2. Experimental procedure	72
5.2.1. Sample preparation	72
5.2.2. Compression tests and characterization	73
5.3. Results	74
5.3.1. Sample preparation	74
5.3.2. Compression tests	75
5.4. Discussion	79
5.4.1. Deformation behavior of single pillars	79
5.4.2. Flow strength as a function of pillar diameter	85
5.5. Conclusions	90
5.6. References	91
6. <i>Conclusions and outlook</i>	93
6.1. General conclusions	93
6.1.1. Metal nanoimprinting	93
6.1.2. Suitability for optical applications	94
6.1.3. Mechanical properties	94
6.2. General outlook	95
Appendix	97
Curriculum Vitae	98
Publications	98
Conference contributions	99

Summary

In this thesis project the imprinting (embossing) technique is studied in detail and pushed towards its limits in terms of small size and high aspect ratio. The process itself is not complicated: it involves compressing a ductile metal against a structured rigid mold, which results in the reproduction of the corresponding topography into the metallic surface by means of plastic deformation. The study focuses mainly on silver, and secondly on gold, motivated by the innovative optical effects which can be obtained with the combination of metallic and dielectric subwavelength structures. Silver and gold are the best candidates for such applications because they are the metals with the lowest light absorption. Since they also possess outstanding malleability, a microfabrication technique based on forming appears particularly attractive and with great potential for success.

A process for silver and gold imprinting has thus been established which solves several technological challenges and reliably produces structures of dimensions down to 130 nm and aspect ratios of up to 13, with excellent uniformity over extended areas. Increased formability is obtained by imprinting at a temperature above the metal recrystallization temperature, enabling application of relatively mild forming conditions. These in turn make possible the use of molds consisting of uncoated, easily-microstructured silicon wafers, which show no wear and do not break during the imprinting process despite the material's brittleness, even where there are deep grooves or considerable porosity.

The imprinting process makes possible not only rapid production of large quantities of freestanding silver and gold submicrometer structures, but also metallization of deep trenches in a structured dielectric. This approach has been applied to fabricate a two-dimensional Si–Ag photonic crystal consisting of periodic silver nanopillars embedded in a silicon wafer. The quality and uniformity of the structures is confirmed by the angle-resolved reflectance of these composites in the near infrared, which shows strong resonances due to the interaction of light with the periodic subwavelength structures.

The development of this forming process is also a great opportunity to study the deformation mechanisms in ductile metals at the submicrometer scale, together with

the related size effects. These investigations focus in particular on the mechanical response of imprinted micro- and submicrometer silver pillars subjected to uniaxial compression. The results partially confirm literature observations concerning pillars prepared by focused-ion beam milling, verifying that the size effects noted in those samples are not just artifacts generated by ion-induced surface damage. In submicrometer pillars, strength is in fact seen to scale in a manner inversely proportional to the diameter. The deformation is very inhomogeneous, generally occurring with ample, localized strain bursts. Polycrystalline pillars larger than 1 μm instead show a nearly constant strength and homogeneous deformation. In addition to dislocation slip, twinning and slip on preexisting twin boundaries are also observed to play a significant role in deformation, a consequence of the low stacking fault energy of silver.

The imprinting process developed in this thesis therefore provides a competitive method both for metalizing high-aspect-ratio holes and for producing high-strength metallic micro- and nanoparts. While the metallization of high-aspect-ratio holes may find wide application in future optical and electronic devices, the production of high-strength metallic micro- and nanoparts is expected to increase in application in the rapidly-expanding field of microelectromechanical systems (MEMS).

Riassunto

In questa tesi la tecnica dell'imprinting (goffratura) è studiata in dettaglio e spinta verso i suoi limiti per quanto concerne dimensioni e aspect ratio (rapporto tra altezza e diametro). Il processo in sé non è complicato: consiste nel premere un metallo malleabile contro uno stampo strutturato rigido, cosicché la corrispondente struttura viene trasferita nella superficie metallica tramite deformazione plastica. Lo studio focalizza essenzialmente sull'argento, e secondariamente sull'oro; la scelta è motivata dalle innovative proprietà ottiche che possono essere ottenute combinando strutture di materiali metallici e dielettrici dalle dimensioni comparabili alla lunghezza d'onda della radiazione. Argento e oro sono i candidati più idonei per tali applicazioni in quanto sono i metalli che posseggono il minor assorbimento di luce. Il fatto che essi posseggano pure un'eccezionale malleabilità rende una tecnica di micro fabbricazione basata sulla deformazione plastica particolarmente attrattiva e con grande potenziale di successo.

Un procedimento per l'imprinting di argento ed oro è così stato sviluppato, superando varie sfide tecnologiche e permettendo una produzione riproducibile di strutture dalle dimensioni minime di 130 nm e dall'aspect ratio fino a 13, con un'uniformità eccellente su estese aree. Una formabilità migliorata è ottenuta lavorando ad una temperatura superiore alla temperatura di ricristallizzazione, permettendo in tal modo l'utilizzo di una pressione relativamente contenuta. Questa ha dal canto suo reso possibile l'uso di stampi costituiti da dischi standard (wafers) di silicio non rivestiti, che possono essere facilmente microstrutturati; questi non mostrano usura né si rompono durante il processo di imprinting nonostante la fragilità del materiale, nemmeno nel caso di profondi tagli o di abbondante porosità.

Il processo di imprinting non solo permette la rapida produzione di grandi quantità di strutture submicrometriche di oro e argento free-standing, ma pure la metallizzazione di profondi intagli in un dielettrico strutturato. Questo approccio è stato utilizzato per la produzione di cristalli fotonici bidimensionali Si-Ag, che consistono in nanocolonne d'argento distribuite periodicamente in un disco di silicio. La qualità e regolarità delle strutture è confermata dalla riflettanza di questi compositi

misurata nel vicino infrarosso in funzione dell'angolo d'incidenza della luce, che mostra marcate risonanze dovute all'interazione della luce con le strutture periodiche.

Lo sviluppo del processo di imprinting è al tempo stesso un'ottima opportunità per studiare i meccanismi di deformazione nei metalli duttili a dimensioni submicrometriche, in combinazione con gli effetti di scala ad essi legati. Questa ricerca focalizza in modo particolare sulla risposta meccanica di strutture micro- e submicrometriche quando vengono sottoposte a compressione uniassiale. I risultati confermano parzialmente le osservazioni della letteratura concernenti colonne preparate tramite bombardamento tramite un fascio ionico focalizzato (FIB), verificando che gli effetti di scala non sono semplicemente degli artefatti prodotti dal danneggiamento della superficie causato dall'impatto degli ioni. In colonne submicrometriche la resistenza allo snervamento è in effetti risultata inversamente proporzionale al diametro. La deformazione è altamente disomogenea in quanto è caratterizzata da un andamento non continuo e seghettato, ed è generalmente localizzata. Colonne policristalline di diametro superiore al micron mostrano invece una resistenza pressoché indipendente dalle dimensioni e una deformazione omogenea. In aggiunta allo scorrimento di dislocazioni, anche la geminazione e lo scorrimento su bordi di geminato preesistenti svolgono un ruolo importante nella deformazione, in conseguenza della bassa energia dei difetti d'impilaggio nell'argento.

Il processo di imprinting sviluppato in questa tesi fornisce quindi un metodo competitivo sia per metallizzare buchi d'alta aspect ratio, sia per produrre micro- e nanocomponenti metalliche d'alta resistenza. Mentre la metallizzazione di buchi può trovare ampia applicazione in apparecchi ottici ed elettronici, la produzione di micro- e nanoparti di metallo può fornire una valida soluzione per la preparazione di sistemi micro-elettromeccanici (MEMS), un campo in rapida espansione.

Zusammenfassung

Diese Doktorarbeit befasst sich mit einer detaillierten Untersuchung der Prägetechnik und deren Grenzen bezüglich Grösse und Achsenverhältnis. Der Prägeprozess an sich ist eine einfache Methode: ein duktiles Metall wird gegen eine starre, strukturierte Form gepresst, wobei durch plastische Verformung des Metalls die Oberflächentopographie der Form auf der Metalloberfläche als Relief reproduziert wird. Die Motivation für diese Studie liegt vor allem im Bereich neuartiger optischer Effekte, die durch Kombination von metallischen und dielektrischen Strukturen mit Dimensionen vergleichbar zur Wellenlänge der verwendeten Strahlung erzielt werden können. Als metallisches Material werden dabei vor allem Silber und im Weiteren auch Gold verwendet, da sich beide Metalle durch eine sehr geringe Lichtabsorption auszeichnen. Hinzu kommt eine ausserordentliche Formbarkeit dieser Metalle – eine für diese Mikrofabrikationstechnik vielversprechende Eigenschaft.

Ein Prägeverfahren für Silber und Gold wurde darauf hin entwickelt, das eine grosse Anzahl von technologischen Herausforderungen bewältigt und mit welchem sehr homogene Strukturen bis zu Dimensionen von 130 nm und Achsenverhältnissen von bis zu 13 reproduzierbar hergestellt werden können. Erhöhte Verformbarkeit bei der Prägung kann dabei durch Prozesstemperaturen oberhalb der Rekristallisationstemperatur des Metalls erreicht werden, was ein relativ sanftes Umformen ermöglicht. Dies erlaubt wiederum die Verwendung von Formen aus unbeschichteten, einfach strukturierbaren Siliziumscheiben, die trotz ihrer Sprödigkeit und selbst bei tiefen Furchen oder erheblicher Porosität beim Prägen weder Abnutzung zeigen, noch zu Bruch gehen.

Das Prägeverfahren erlaubt nicht nur die effiziente Herstellung von grossen Mengen von freistehenden Silber- und Goldstrukturen mit Dimensionen im unteren Mikrometerbereich, sondern auch eine Metallisierung von tiefen Furchen in strukturierten, dielektrischen Materialien. Diese Vorgehensweise wird angewendet, um zweidimensionale photonische Si–Ag Kristalle herzustellen, die eine periodische Anordnung von in einer Siliziumscheibe eingebetteten Silbersäulen aufweisen. Die Qualität und Gleichmässigkeit der Strukturen dieser Verbunde konnte durch winkelaufgelöste Reflexion im nahen Infrarotbereich bestätigt werden, welche

aufgrund der Wechselwirkung von Licht mit den periodischen Submikrometer-Strukturen starke Resonanzen zeigt.

Das hier entwickelte Formgebungsverfahren bietet zudem die Möglichkeit, Verformungsmechanismen von duktilen Metallen im unteren Mikrometerbereich mit den zugehörigen Grösseneffekten zu studieren. In diesem Projekt wurde dazu vor allem das mechanische Verhalten von geprägten Säulen im Mikrometerbereich oder kleiner unter einachsiger Kompression untersucht. Die Ergebnisse bestätigen teilweise jene in der Literatur geschilderten Beobachtungen an Säulen, die mittels fokussierter Ionenstrahlung hergestellt wurden. Damit konnte gezeigt werden, dass die Grösseneffekte, die in derartig hergestellten Säulen beobachtet wurden, keine durch den Ionenbeschuss hervorgerufenen Artefakte sind. In Submikrometer-Säulen zeigt die Festigkeit eine umgekehrt proportionale Abhängigkeit vom Durchmesser. Die Verformung ist sehr inhomogen, was lokal vermehrt zu Verformungsspitzen führen kann. Polykristalline Säulen, die grösser als 1 μm sind, weisen dagegen eine fast grössenunabhängige Festigkeit und eine homogene Deformation auf. Es wurde festgestellt, dass zusätzlich zum Versetzungsgleiten auch Zwillingsbildung und Gleitung auf bereits existierenden Zwillingsgrenzen eine wichtige Rolle bei der Deformation spielen, was auf die tiefe Stapelfehlerenergie von Silber zurückzuführen ist.

Damit bietet das hier entwickelte Prägeverfahren eine wettbewerbsfähige Methode zur Metallisierung von Vertiefungen mit hohem Achsenverhältnis und für die Fabrikation hochfester metallischer Mikro- und Nanoteile. Während die Metallisierung von Vertiefungen mit hohem Achsenverhältnis breite Anwendung in optischen und elektronischen Bauteilen finden könnte, wird erwartet, dass die Fabrikation von hochfesten metallischen Mikro- und Nanoteilen im rasch wachsenden Gebiet der mikroelektromechanischen Systeme (MEMS) zu vermehrter Anwendung kommt.

1. Introduction

1.1. Motivation

Gold and silver were, with copper, the first metals available to mankind. This is due to their outstanding chemical stability, which makes them accessible in nature in the metallic state; their use was thus not dependent on the laborious extraction from minerals, as was the case for other metals. Because they are shiny these materials have always attracted people's curiosity and have been used in nearly every culture for producing ornaments. Their formability was immediately recognized and exploited to create artwork of impressive quality. The metals were valuable, and rapidly became the standard material for making coins. To differentiate coins and verify their origins, characteristic patterns were imprinted on their surfaces (Fig. 1). This ancient, widespread forming process of transferring micropatterns from a stamp onto a metal surface by pressing them together is therefore also called *coining*.



Fig. 1.1. Silver coin made in Athens around 480 BC [1].

It is fascinating to observe that this ancient process is still extensively applied today, and that despite its long history and widespread application it is not yet completely understood. In particular, problems arise when dimensions are reduced to the micrometer scale, because there the materials behave differently than they do on

the macroscale. In fact, at very small sizes the metal can no longer be considered a homogeneous continuum. This reduces the reliability of microforming simulations and complicates prediction of the necessary forming parameters (setting of so-called “size effects”, see section 1.4).

In this study the formability of gold and silver was investigated for pattern dimensions in the micro- and especially submicrometer range in order to produce high-aspect-ratio structures. The goal was to achieve a more detailed understanding of the imprinting process, and to obtain comprehension and control of the process parameters to produce high-quality structures, thereby demonstrating that this technique is suitable for fabricating metal-containing optical devices. The motivation for this research grew out of a collaborative effort of several ETH and EMPA groups: the INIT project on *Composite Doped Metamaterials*. The goal of this project was to investigate the optical properties of micro- and nanostructured metallo-dielectric composites by combining the simulation, fabrication (our task) and characterization experience of the various groups. Interestingly, the peculiar optical properties of silver and gold, which reflect nearly all light, were the reason for their first use by mankind. But precisely the optical properties of these metals have attracted renewed enthusiasm in recent years, via theoretical proposals and preliminary experimental observations of several potential groundbreaking applications which may revolutionize information technology and other central aspects of our lives. This thesis therefore offered the intriguing prospect of applying a technique with thousands of years of history, using the same metals employed since the Neolithic and inspired by the same outstanding optical properties which attracted our ancestors, while at the same time targeting applications which are extremely up-to-date if not still imaginary, such as the invisibility which might be obtained using a composite material with a negative refractive index. In the meantime, this project has offered an optimal opportunity to investigate the mechanisms governing plastic deformation in ductile materials.

The first part of the project therefore took a mainly application-oriented approach, the goal being to produce uniform, high-aspect-ratio structures of maximum quality, which is required for low-loss optical devices. The shape of the structures produced was, however, also ideal for mechanical characterization by uniaxial compression. A significant part of the project was therefore devoted to investigating the mechanical

properties of metallic pillars at submicrometer scales. These mechanical tests are of particular interest because they are among the first studies performed on pillars not produced by focused-ion beam milling, enabling a differentiation between fabrication (ion-induced) artifacts and effective property changes at the microscale caused by size effects.

1.2. Metal microfabrication techniques

Today a large, rapidly-growing market exists for devices consisting of freestanding metallic microstructures or of micropatterned dielectric materials, whose cavities are filled with metals. Some examples are molds for polymer embossing, microreactors, micro heat-exchangers, and metal interconnects (vias) in the integrated circuit (IC) technology. In this context several fabrication methods have been developed.

In this section some of the available processes are presented along with their strengths and limitations (see also Ref. [2]), and our choice of the nanoimprinting technique explained on this basis. Some methods are based on IC technology and are already well-known, while others are innovative and not yet widely applied. The criteria for selecting the fabrication technique stemmed from the goal of metalizing with pure metals (ideally silver and/or gold) grooves and cylindrical holes of very high aspect ratio in dielectrics. The dielectric can afterwards be removed in the case that freestanding high-aspect-ratio metallic structures are aimed. All of the presented methods are able to process several structures in parallel, making possible high production rates and reduced costs in industrial applications. The preliminary dielectric micropatterning is usually performed using photolithographic techniques, which are widely available because they are the habitual patterning tool in the IC industry. The standard lithographic method is ultraviolet (UV) lithography. Here a thin photosensitive polymer film (a “photoresist”) is first deposited on a wafer by spin coating. The photoresist is then locally irradiated by shining UV light through a mask (Fig. 1.2a). If the film is a *positive* photoresist the chemical bonds of the polymer chains are partially broken by the UV radiation, and the irradiated regions thus become much more soluble in a specific chemical solution (developer). All the resists

used in the study were of this type; negative photoresists, in which irradiated regions become more cross-linked and therefore stable, are, however, also available. After exposure, the soluble part of the resist is removed by immersion in the developer solution, which leaves the exposed regions of the wafer unprotected for subsequent local etching. For small-scale production of high-resolution patterns, the standard technique is, however, electron beam (e-beam) lithography. Here the photoresist is locally irradiated via electron beam scanning of the surface regions to be exposed. This technique enables the design of discretionary patterns without the production of expensive masks, but it is slow due to its serial nature.

After resist development, the wafer can be structured by wet or dry etching techniques. Wet etching, which is cheaper, is either isotropic or anisotropic (only for single-crystalline wafers). For silicon typical anisotropic wet etching is obtained using a KOH aqueous solution; the (111) planes are etched considerably slower than the others, producing V-shaped holes with 54.7° -sloped walls for (100) wafers or parallel grooves with vertical walls for (110) wafers. In order to transfer the resist pattern into the wafer without the strict geometrical restraints of wet etching, dry etching is applied; this was also done in this thesis project. Dry etching can be physical or chemical. In the former, where etching essentially proceeds via ion bombardment, the process generates good wall verticality but has little selectivity, such that the protective layer is rapidly destroyed and high-aspect-ratio holes cannot be achieved. In chemical etching, in contrast, good selectivity can be obtained but etching is usually rather isotropic, resulting in near-spherical holes and mask undercut (the cavity in the wafer is larger than the photoresist opening on the surface). The solution making it possible to produce deep holes with vertical walls is to use an optimally-balanced combination of both physical and chemical etching. An additional technique, enabling the achievement of extremely high aspect ratio with nearly vertical walls, is exploited in the “Bosch process”, or ICP-DRIE (deep reactive ion etching with inductively coupled plasma), where short etching steps are alternated with rapid wall passivation steps. This technique, however, produces very rough walls (Fig. 1.2b) because of the nearly isotropic etching steps.

The etch depth of high-aspect-ratio cavities depends among other things on the pattern width, because of the diffusion-limited mobility of reactants and etching products as well as the surface charges in deep thin holes. On the same wafer

(comprising the imprinting molds in this study) the thinner grooves are therefore not as deep as the larger ones (Fig. 1.2b). This phenomenon is called *ARDE* (aspect ratio dependent etching).

More information on today's most common microfabrication methods can be found in a detailed overview by M. Madou [2].

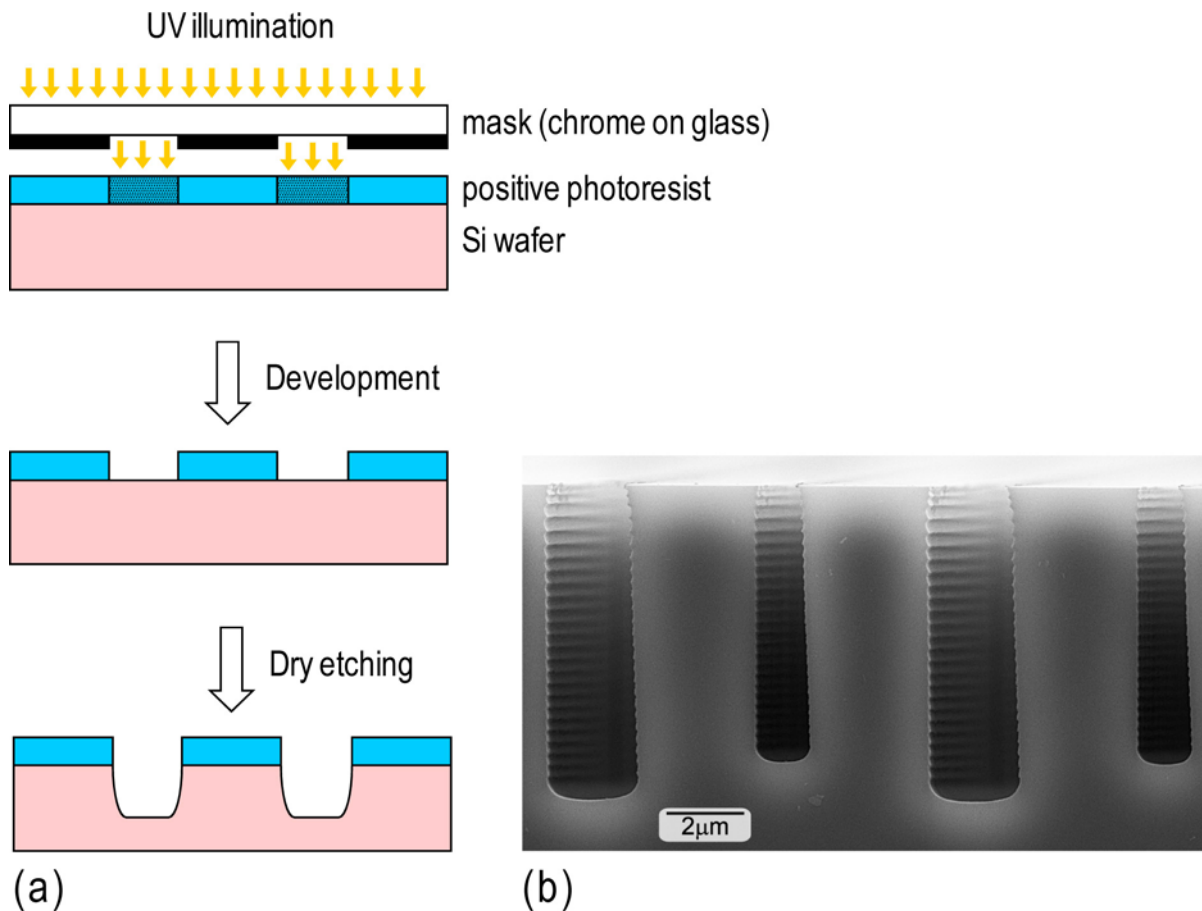


Fig. 1.2. (a) Sketch of UV lithography. UV light is shone only on selected parts of a photosensitive polymer by using a mask. The exposed parts are modified by the radiation, and in a positive photoresist they become more soluble to the developer solution. After development (removal of the soluble parts by immersion in the developer solution), the dielectric is no longer protected in the patterned regions and can be locally etched using wet or dry methods. (b) 1- and 2- μm -wide, 7- or respectively 8- μm -deep grooves etched in a silicon wafer via the ICP-DRIE process. 26 rapid cycles of etching and passivation steps were used, which resulted in rough walls with just as many horizontal lines. The etching depth also depends on the opening width.

1.2.1. Electroless metal deposition and electrodeposition

Both methods are based on a REDOX (reduction-oxidation) reaction; the sample is immersed in a solution containing metallic ions which are reduced and precipitated on the sample surface to form a metallic film.

In electroless metal deposition the solution is thermodynamically unstable and the metal tends to precipitate, so the solution stability and deposition rate are controlled with chemical additives. The advantages of this technique are the broad experience resulting from its widespread use in IC technology; its potential for depositing on both conductors and nonconductors; its limited operational costs; and the possibility of depositing several metals and even alloys. Compared to electrodeposition this technique is also easier (no plating electrode required) and creates less internal stress in the metallic structures. Electroless metal deposition's disadvantages, shared also by electrodeposition, are its use of wet chemistry (vacuum processes are generally preferred in IC technology) and toxic substances (for gold and silver the typical plating bath contains cyanides [2-5]).

In electrodeposition the reactions involve a flow of electric current under an imposed bias, which controls the deposition rate. The anodic and cathodic reactions take place at separated electrodes, in contrast to electroless deposition. Electrodeposition has the advantage of also filling cavities with very high aspect ratio. The superconformal bottom-up filling by electrodeposition (filling starting from the hole bottom, enabling complete filling without voids) is nowadays the most popular method for interconnect copper metallization [6-9], and recipes for superconformal filling with silver are also available [3, 8]. The metal in excess is then removed by chemical mechanical polishing (CMP), a process where the mechanical abrasion is sustained by chemical etching, enabling a good selectivity of the material being removed and achieving optimal planarity. The whole process is called damascene patterning. Another application of electrodeposition is the production of nickel micromolds for polymer embossing, fabricated using the LIGA process ("Lithographie-Galvanoformung-Abformung" [10]): in this process nickel is electrodeposited in the cavities of a thick photoresist, patterned with very high aspect ratio via synchrotron radiation. Use of the synchrotron makes the fabrication of a mold very expensive, but once the first piece is made countless identical nickel molds

and polymer parts can be produced by reciprocal embossing and electrodeposition. The main disadvantage of electrodeposition, in addition to the wet chemistry and toxic compounds analogous to the electroless deposition, is the need for a conductive substrate. In the case of insulators, a thin adhesion layer followed by a conductive seed layer must be deposited by other techniques (usually chemical vapor deposition) prior to electroplating.

1.2.2. PVD: Physical vapor deposition (evaporation/sputtering)

To deposit metal films two techniques belonging to the PVD family are widely used: thermal evaporation and sputtering.

In the thermal evaporation process the metal is usually evaporated with an electron beam in order to minimize contamination. The chamber pressure is very low, such that most atoms reach the sample in a straight direction, without being scattered by collisions with other particles. A disadvantage of this technique is therefore a strong susceptibility to shadowing effects if there are topographical steps on the sample. The virtues of thermal evaporation lie in the possibilities it presents for a very high deposition rate and excellent purity. In addition, the impact of the atoms with the substrate is low-energy, so that no surface damage occurs (except for some x-ray radiation in cases of e-beam deposition); the low impact energy also implies, however, reduced adhesion of the film to the substrate.

During sputtering, a plasma with positively charged Ar^+ ions is created in the deposition chamber. The ions are accelerated towards a negatively-charged plate consisting of the metal to be deposited (target). Due to momentum transfer, metallic atoms are sputtered away from the target and are deposited on the sample, placed in front of it. Sputtering has the advantage over evaporation of functioning with a wider range of materials, of having a better step coverage due to a higher chamber pressure (resulting in very short mean free path of the sputtered atoms), and of demonstrating better adhesion to the substrate because of the atoms' high impact energy. In addition, good uniformity can be achieved over large areas. Deposition rates are, however, lower and there is a greater tendency to incorporate impurities into the film due to the vacuum in the deposition chamber, which is worse than that in thermal evaporation.

PVD is also employed extensively to produce metallic micropatterns on a wafer, with the so-called *lift-off* process. In this technique the metal is deposited by PVD on a wafer partially covered by a patterned photoresist, which is afterwards chemically removed. Only the metal deposited in the photoresist openings remains on the wafer.

Both PVD techniques share the disadvantage, significant in the context of this project, of only filling completely grooves with low aspect ratio (usually limited to 0.5-1) [8].

1.2.3. CVD: Chemical vapor deposition

In chemical vapor deposition the precursors of the film to be deposited are introduced into the chamber in gaseous form and react with each other, preferentially on or close to the heated substrate, to form the solid film and gaseous byproducts. CVD has the advantages of being very versatile, of working with several materials, and of also enabling high-purity deposition, so that it is extensively used in the semiconductor industry. To activate the chemical reaction, energy must be supplied; the energy source can be thermal (the most common case), radio frequency (plasma-enhanced CVD), or photon radiation. The deposition rate is limited by either the mass-transport or the reaction rate, depending in particular on temperature and chamber pressure. The process is slow, so that CVD is usually used for thin layers of tens to a few hundreds of nanometers.

With the correct choice of chamber pressure (i.e. particle mean free path), substrate temperature (atom surface migration rate) and arrival angle of the reacting molecules, it is possible to achieve conformal step coverage even where there are deep trenches, useful for example for depositing barrier and seed layers for electrodeposition. For optimal filling of high-aspect-ratio holes, superconformal filling is used instead. Recipes are available for copper [11], and CVD copper metallization (instead of wet electrodeposition after CVD of the seed layer) is gaining popularity in the IC industry because it enables complete processing under vacuum. No recipes are, however, currently available for superconformal deposition of silver [8].

1.2.4. Microforming (nanoimprinting)

Metal microforming, as mentioned in the motivation section, is an old and relatively simple technique but has seldom been applied to fill submicrometer cavities with metals. The process is based on irreversible plastic deformation of a metallic plate, analogous to the popular polymer embossing (also called nanoimprinting). The details of this technique are discussed in section 1.3, but here we summarize the strengths and weaknesses of the process, enabling a comparison with the other techniques and clarifying its selection for the fabrication of the microstructures. Its strengths are simplicity, reduced costs, absence of toxic substances, the possibility of using pure metals, and the capability of applying the same method both for filling grooves in a dielectric material and producing freestanding metallic microstructures. Its weaknesses are the use of high pressure and its limitation to unordinary amorphous alloys or to very ductile metals (this point is, however, not very problematic because the most interesting metals for optical applications, silver and gold, both show outstanding malleability). Another difficulty is the limited knowledge of the limits (dimensions, aspect ratio) and mechanisms forming the basis of this technique. The reasons are, on the one hand, the appearance of size effects, hindering straightforward predictions of microscopic behavior based on macroscopic know-how, and on the other the little available literature, stemming partially from government secrecy surrounding the coining process [12].

1.2.5. Other techniques

In addition to the well-established techniques previously described, several processes for metal microfabrication have been tested on a small scale but have not yet found wide application. Here we report some promising methods:

(i) *Microcasting*. Casting is a technique similar to forging, but which exploits the liquid state of the metals to fill molds of very complex shape. At the submillimeter scale, molds with holes of a diameter of 230 μm and aspect ratios of up to 90 have been successfully filled with a gold alloy [13], and smaller dimensions are certainly possible, at least with lower aspect ratio.

It is, however, very difficult to apply this technique to high-aspect-ratio structures with dimensions of a few microns or less. The surface effects in this case become

extremely important. Good wetting between metal and mold is necessary to push the metal into thin cavities with moderate pressures, but good wetting is often correlated with significant reactivity between the two materials; unconventional mold materials may therefore be required, for which no standard microstructuring procedures are available. In addition, metal crystallization shrinkage reduces shape accuracy and can generate internal stresses. Finally, to use the best optical metals (silver and gold) in the liquid state very high temperatures would be needed, making particular demands on the casting machine and the mold material. Nevertheless, a sophisticated casting method which avoids some of these issues was recently presented by Cui *et al.* [14], who were able to fill 100 nm holes of aspect ratio 5 with molten copper. In their process a metal film is first deposited on the structured silicon wafer by PVD. The film is pressed with a transparent glass and melted very rapidly using a 20 ns laser pulse. The metal is expected to fill the holes within some 100 ns and quickly solidify, hopefully fast enough to avoid possible reactions, which were not investigated. Significant local stresses due to rapid cooling are, however, expected.

(ii) *Colloidal nanoparticles.* This method, applied by Zhang *et al.* for fabricating one- and two-dimensional gold-dielectric photonic crystals [15-16], exploits differences in surface tension to concentrate colloidal gold nanoparticles during solvent evaporation in periodic holes made in the dielectric (photoresist on glass). The sample is then annealed to melt the nanoparticles, obtaining dense metallic microstructures. Pillars with a diameter of 100 nm and an aspect ratio of 2 have been produced with this technique. It should also be possible to extend it and fill only selected holes, either by controlling the local surface tension or by locally depositing the suspension with a microcapillary.

The advantages of this method are its simplicity, high processing speed and low cost, while potential issues lie in possible porosity and solvent residue trapped in the metal, incorporation of surface impurities into the metallic structures, and strong constraints on pattern design (only regular patterns with constant structure sizes and compatible ratios between size and period of the structures are feasible to enable all particles to reach a hole during solvent evaporation).

(iii) *Direct metal etching.* In all previously-described methods the first step is to microstructure a dielectric using lithography and dry etching techniques; then the

cavities are filled via one of the processes described. If the goal is to fabricate freestanding metallic structures, the dielectric is afterwards removed. Here it would, however, be faster to microstructure a metal film directly via a dry etching process, after masking the parts to be protected. This approach would save a fabrication step. Direct gold dry etching was applied by Guo *et al.* [17] to prepare low-aspect-ratio gold-dielectric photonic crystals, using photoresist as mask material and ion milling for good anisotropy. To achieve a high aspect ratio, however, a large selectivity between the metal and the mask material is needed, which is difficult to obtain with noble metals. Aspect ratios as high as 10 have instead been demonstrated in titanium [18], and large arrays of 50 nm aluminum lines with aspect ratio 4 have been shown [19]. Cheaper wet etching techniques would only work for very low aspect ratios, because they usually etch isotropically; for anisotropic wet etching the grain size and orientation of the metal should be controlled extremely precisely.

(iv) *Transfer printing*. This technique, like others in the family of soft lithographic processes [20], is an additive method for depositing arrays of microstructures on a wafer. The structures are placed temporarily on a flexible film, whose elasticity favors the demolding. Arrays of gold nanocones were recently prepared by Kim *et al.* using transfer printing [21]. The gold cones were produced by thermal evaporation on a patterned polymer mold, which was then slightly pressed onto the wafer. By controlling the adhesion forces between gold and mold, or gold and wafer, respectively, they managed to transfer the gold cones onto the wafer. The aspect ratio of the structures is, however, limited by the use of PVD for the gold deposition and the demolding forces which tear off high-aspect-ratio structures, although these issues may be overcome by modifying the process.

1.2.6. Selection of the fabrication method

Based on the peculiarities of the various fabrication methods presented in the previous sections, it was decided to focus on metal nanoimprinting (embossing) for the following reasons: its potential to fill high-aspect-ratio holes (a requirement which excluded PVD methods); its intrinsic simplicity and its suitability for working with high-purity silver and gold, exploiting their outstanding ductility; the currently limited state of process know-how (where several questions concerning deformation mechanisms, size effects and fabrication limits remain open, offering an opportunity

in the context of this study to contribute significantly to a better understanding of the process); the possibility of applying the same process to both metalizing dielectric voids and producing freestanding structures; and finally the availability in our group of background knowledge and machines which could be conveniently converted to imprinting devices.

1.3. Microforming (imprinting): State of the art

Metal microforming is a broad concept which includes several techniques, all based on plastic deformation, which enable the production of microparts, generally defined as structures with at least two dimensions in the submillimeter range [22]. The forming techniques embrace forging, extrusion, punching, bending and embossing (imprinting/coining); the last method is the one which was applied in this study.

In the embossing process the ductile material is pressed against a structured hard material (mold) and deforms plastically, assuming the corresponding topography. The deformation is essentially limited to the material part lying close to the surface in contact with the mold. After embossing, the mold is usually removed to obtain freestanding microstructures, but the same process can also be exploited to fill the cavities of a structured hard material with a softer one, without subsequent separation, to produce a two-dimensional composite.

On the macroscale, embossing is widely applied to introduce surface textures in metals, polymers and inorganic glasses. Typical advantages of the embossing technique, and of forming processes in general, are high processing rate, very limited or no waste of material, and for metals the possibility of adjusting the final mechanical properties to the desired application, controlling the hardening mechanisms involved in the deformation.

On the submicrometer scale this process has been applied almost exclusively to polymers (essentially amorphous thermoplastics), for example to produce security holograms. The reasons are material uniformity down to very small scales and easy control of the mechanical properties of thermoplastics via temperature modification

or UV curing, making possible rapid and low-pressure forming in a low-viscosity state and subsequent demolding in a stable, solid state [23-25]. Accurate reproduction of extremely small dimensions in polymer thin films has been demonstrated (lateral sizes below 10 nm [25]). Due to its high resolution and low cost this technique is a promising candidate for becoming a leading future lithographic method (it is therefore often called nanoimprint lithography). Silicon molds have been widely tested for small-scale production due to their easy microfabrication [24, 26-30], but the typical mold material for commercial production of microembossed polymer components is nickel (and its alloys), usually prepared by LIGA if high aspect ratios are required.

The substitution of polymers with metals implies some complications: the pressure required is usually considerably higher (resulting in increased mold wear and more expensive machines), the elastic limit is lower (complicating the demolding), and great interdiffusion or possible reactivity at elevated temperatures limit the availability of compatible metal/mold combinations. The first two issues are less problematic in metallic glasses, a class of metallic alloys characterized by an amorphous structure [31-33]. Analogous to amorphous polymers, these materials present a radical change in mechanical properties (viscosity) when the temperature exceeds the glass transition temperature T_g . Above T_g metallic glasses can be deformed superplastically (the suitable temperature range for processing is, however, rather small, limited by the crystallization temperature), while at lower temperatures they are stiff and can be demolded while maintaining their shape. Their amorphous structure has the additional advantage of isotropicity and uniformity down to very small scales, in contrast to polycrystalline superplastic alloys, where superplasticity at elevated temperatures is mainly carried out by grain-boundary sliding. These crystalline superplastic alloys are characterized by a fine grain size, which remains nearly constant during deformation. Even though it is small, the grain size is not negligible when the mold cavities have dimensions of a few micrometers or less; in this case accurate mold reproduction is only possible via grain deformation. In this case polycrystalline superplastic alloys have no advantages compared to conventional polycrystalline metals, showing the same issues of high pressure requirements and inhomogeneous behavior [34]. Not surprisingly, most research on metal microembossing therefore focused on metallic glasses [see, for example, 26, 27, 34-

37]. These alloys can then even be used as appropriate mold materials for polymer embossing or metallic glasses with lower T_g , if applied in the rigid state. Accurate reproduction of submicrometer structures in metallic glasses, with dimensions below 100 nm, has been demonstrated. These alloys are, however, not attractive for optical applications because of their large absorption (see section 3.2).

In standard crystalline metals, such as gold and silver, the main mechanism for plastic deformation is dislocation gliding. The dislocation mobility, which controls the necessary formability during imprinting and the mechanical stability of the structures after forming can be strongly influenced by the temperature. In cold-forming, the dislocation density increases with ongoing deformation and the metal becomes harder, because an increasing number of dislocations hinder each other's motion. The mechanical properties of the final structures can therefore be optimized for the desired application by controlling the local forming degree. In warm-forming, better formability and reduced scattering can be achieved because of thermally-activated processes such as dislocation climbing, diffusion, and allocation of additional slip systems [38, 39]. Finally, in hot-forming, defined as deformation at a temperature above the metal recrystallization temperature, the material can dynamically recrystallize and continuously recover its maximal ductility. Recrystallization enables the highest formability and lowest process forces but often leads to the worse surface quality. Correct control of the imprinting temperature is therefore crucial for working at a moderate pressure (limiting mold wear and deformation) and achieving high-quality products.

Nowadays one of the few important applications of metal microforming is *wire bonding*, a process where different microchip components are connected electrically by bending and sticking metal wires (typically made of gold) with diameters down to 10 μm . Embossing is rarely applied commercially for structure dimensions smaller than 100 μm , which is the lower limit for coin microstructures; below this size, especially for high aspect ratios, this technique is essentially limited to scientific investigations. An exception involving the industrial application of metal microembossing is the imprinting on gold bars of periodic line arrays with widths on the order of 1 μm , deployed by the Swiss company Argor Heraeus [40] as certification marks for ingots (Fig. 1.3). A low microstructure aspect ratio is sufficient to produce light interference effects, resulting in a macroscopic pattern which changes

color depending on the observation angle; the pattern both guarantees the origin of the bar and provides a nice aesthetic effect. However, the potential applications of metal micro- and nanoimprinting are numerous in the present rapidly-growing microproducts market. The process would be, for example, ideal for producing components for microfluidics and microreactors, an emerging technology where small amounts of liquids are merged and react in a controlled way; the reactor material (e.g. gold or platinum, another ductile metal with strong catalytic effects) could even act as reaction catalysts. Other applications may lie in heat exchangers [41-42], or electromagnetic relays for high power applications [43].

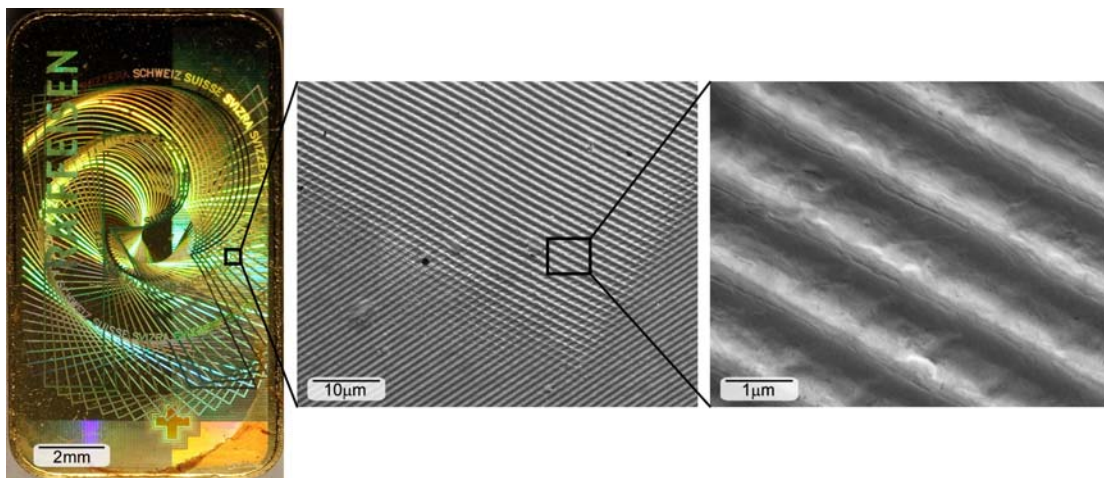


Fig.1.3. Microembossed gold bar, commercialized with the trade name Kinebar[®], where the interference effects are generated by periodic variations in the surface topography, illustrated in the close-up electron microscopy images. The goal is both a decorative effect and to guarantee the bar origin.

Research on ductile metal embossing at small scale was initiated in 1998 by Pang *et al.*, who imprinted aluminum plates at room temperature [44]. Using molds made of SiC, a material harder than silicon and therefore less prone to break, they showed the imprinting of holes with lateral sizes as small as 40 nm; the hole depth could, however, not be precisely measured. Producing cavities in the metal by imprinting is nevertheless considered easier than the inverse (producing projections using a mold with holes), because the metal to be formed is in direct contact locally with the mold projections and less material must be deformed [12].

Pang indicated that a relatively low pressure of 115 MPa is enough for imprinting, but Böhm *et al.*, also working with aluminum at room temperature, showed that even

a pressure of 800 MPa is not sufficient to achieve perfect mold filling where there are metal microprojections, and preexisting scratches on the plate were still visible on the top surfaces of the formed structures, confirming the increased difficulty to fill mold cavities with metal compared to making holes in the metallic plate [28]. Böhm also showed that silicon can be used as mold material for imprinting favorable patterns in a soft metal (structures with sloped walls and without sharp edges and corners).

Hirai *et al.* achieved 200 nm periodic gold lines with an aspect ratio of 1.5 by imprinting at room temperature a gold thin film deposited on a glass substrate [29]. Extremely high pressures (1 GPa) were needed, however, partially because of the small ratio between metal thickness and structure depth, resulting in frequent mold failure.

Recently Hsieh *et al.* tried to improve metal formability to make possible a reduction of the required embossing pressure, by imprinting aluminum thin films at a temperature above the recrystallization temperature [45]. The metal, however, showed a rough microstructure, attributed to grain growth, and they concluded that a lower processing temperature should be used for high-quality imprinting.

A different strategy for imprinting metals at low pressure was proposed by Chen *et al.*, who deposited the metal film to be imprinted on a deformable polymer material (photoresist) [46]. Only very low aspect ratios were achieved, however.

The different backgrounds of the researchers investigating metal microembossing produced several names which describe nearly identical processes, generating some confusion. In particular, two communities are working on this topic. Metallurgists approach the process from the angle of macroscopic metal forming and are mainly interested in the size effects which appear when the dimensions are reduced; they usually call the process “microcoining”, “microembossing”, “microforging”, or “microforming”. Microelectronic engineers, familiar with polymer embossing (nanoimprint lithography), approach the field by substituting the polymers with metals; they generally use the terms “nanoimprinting” or “compression molding”. In this thesis the terms “nanoimprinting” and “embossing” are used as synonyms for the same process.

1.4. Scaling and size effects

In component miniaturization one often observes a non-linear scaling of various properties, such that the material behavior at micro- and nanoscales cannot always be easily extrapolated from the macroscopic properties. One important reason for this is the increasing ratio of surface area to volume, correlated with object shrinking, which makes surface effects more influential. This has a significant effect on several phenomena such as diffusion, evaporation rate and capillary forces (caused by surface tension) [2].

In forming processes, and in general when mechanical properties of metals are involved, size effects are often already noticeable at relatively large scales (submillimeter range), mainly because of the reduced grain number involved in the deformation [38, 47]. In common macroscopic objects the structure size is much larger than the grain size, so the material can be approximated to a continuum and behaves nearly isotropically (or according to a preexisting texture). When forming into small cavities, on the other hand, only one or just a few grains are concerned; the formability depends on the orientation of the single grains, resulting in scattering in the forming behavior and inhomogeneous properties in the formed material (the most favorably-oriented grains are more heavily deformed, becoming harder with cold work, and different grain numbers and orientation in the structures produce different mechanical properties). In this context metallic glasses have the significant advantage over crystalline metals of remaining isotropic down to very small scales because of their amorphous structures, as mentioned in the previous section.

In addition to the microstructure (grain size), the surface topography usually does not scale linearly with the sample dimensions, resulting in changes in the tribological properties. This phenomenon is especially relevant when forming is performed with a lubricant layer; enhanced friction is then observed in smaller samples [22, 38].

At very small scales (on the order of a few micrometers and lower), the approach of structure sizes to the dislocation interaction distance and sometimes also the presence of strong strain gradients [48] also produce additional size effects; macroscopic phenomena such as work hardening may therefore assume a different efficacy at submicrometer scales. In addition, the inhomogeneous number, quality

and position of defects (e.g. preexisting dislocations) at very small scales are the origin of significant scattering in the mechanical properties. These effects are discussed in detail during the investigation of the mechanical properties of micro- and submicrometer silver pillars presented in Chapter 5.

Finally, size effects have direct effects on manufacturing costs: in microfabrication the detrimental effect of dust, which is negligible for large components, necessitates the use of expensive clean rooms. Moreover, the precision required for mold fabrication, measurement and handling techniques sets additional challenges for cheap production at the micro- and nanoscale [38].

1.5. Aims and outline of the thesis project

As mentioned in section 1.1, the motivation for this thesis project was a collaborative project among several groups from ETH Zurich and EMPA Dübendorf. This was the INIT project on Composite Doped Metamaterials, involving the Laboratory for Electromagnetic Fields and Microwave Electronics (D-ITET), the Electronics Laboratory (D-ITET), the Laboratory of Metal Physics and Technology (D-MATL), the Laboratory of Physical Chemistry (D-CHEM), and the Electronics/Metrology Institute at EMPA. The goal was to conceive, simulate, fabricate and characterize optical devices containing periodic, high-aspect-ratio metallic structures working in the near infrared (and especially around the typical telecom wavelength of $1.5\ \mu\text{m}$, thus requiring structures with dimensions of $0.2\text{-}1.5\ \mu\text{m}$). The author's assignment was microfabrication of the metallic component.

The first task was therefore to select suitable metals and the fabrication technique. After the decision to focus on nanoimprinting (for the reasons explained in section 1.2.6) and on the two metals silver and gold (choice clarified in section 3.2), the aims of the project became the following three: (i) development of the imprinting process; (ii) investigation of the suitability of nanoimprinting for producing optical devices; (iii) investigation of deformation mechanisms and scaling laws in imprinted micro- and nanopillars.

1.5.1. Development of the nanoimprinting process

The development of the fabrication technique and characterization of the produced structures constituted the major part of the project in terms of time invested. The limits in size and aspect ratio were investigated and several setup modifications were explored in order to expand the feasible range of structure size and shape. A mold removal procedure was also developed, enabling rapid characterization of the patterns produced. The process development is described in Chapter 3. Several details and observations are added as aids to readers wishing to reproduce the fabrication technique.

1.5.2. Suitability for optical devices

After demonstrating the possibility to achieve the required structure size and aspect ratio, a silver-silicon test sample was produced and optically characterized by variable angle reflectance. This is described in Chapter 4.

1.5.3. Mechanical characterization of imprinted pillars

The deformation mechanisms in micro- and submicrometer pillars were investigated by uniaxial compression in collaboration with the Laboratory for Nanometallurgy at ETH. The investigation aimed to understand the mechanisms and scaling effects involved, as well as the influence of the fabrication method on the mechanical properties. This part of the thesis is discussed in Chapter 5.

1.6. References

- [1] British Museum, London, UK.
- [2] M. Madou, Fundamentals of Microfabrication, 2nd edition, CRC, Boca Raton, USA, 2002.
- [3] B. C. Baker, M. Freeman, B. Melnick, D. Wheeler, D. Josell, T. P. Moffata, J. Electrochem. Soc. 150 (2003) 2 C61-C66.
- [4] K. Márquez, G. Staikov, J. W. Schultze, Trans. IMF 80 (2002) 3 73-78.
- [5] Y. Okinaka, M. Hoshino, Gold bulletin 31(1998) 1 3-13.
- [6] http://domino.research.ibm.com/comm/wwwr_thinkresearch.nsf/pages/copper397.html (1997).
- [7] P. C. Andricacos, C. Uzoh, J. O. Dukovic, J. Horkans, H. Deligianni, IBM J. Res. Dev. 42 (1998) 567.
- [8] D. Josell, C. Burkhard, Y. Li, Y.-W. Cheng, R. R. Keller, C. A. Witt, D. R. Kelley, J. E. Bonevich, B. C. Baker, T. P. Moffat, J. Appl. Phys. 96 (2004) 1 759-768.
- [9] P. Moon, V. Chikarmane, K. Fischer, R. Grover, T. A. Ibrahim, D. Ingerly, K. J. Lee, C. Litteken, T. Mule, S. Williams, Intel Tech. Journal, 12 (2008) 2 87-92.
- [10] E. W. Becker, W. Ehrfeld, P. Hagmann, A. Maner, D. Münchmeyer, Microelectronic Engineering 4 (1986) 35-56.
- [11] D. Josell, S. Kim, D. Wheeler, T. P. Moffat, and S. G. Pyo, J. Electrochem. Soc. 150 (2003) 5 C368-C373.
- [12] H. Ike, M. Plancak, J. Mater. Process. Tech. 80-81 (1998) 101-107.
- [13] G. Baumeister, K. Mueller, R. Ruprecht, J. Hausselt, Microsystem Tech. 8 (2002) 105-108.
- [14] B. Cui, W. Wu, C. Keimel, S. Y. Chou, Microelectr. Eng. 83 (2006) 1547-1550.
- [15] X. Zhang, B. Sun, R. H. Friend, H. Guo, D. Nau, H. Giessen, Nano Lett. 6 (2006) 4 651-655.
- [16] X. Zhang, B. Sun, H. Guo, N. Tetreault, H. Giessen, R. H. Friend, Appl. Phys. Lett. 90 (2007) 133114.
- [17] H. C. Guo, D. Nau, A. Radke, X. P. Zhang, J. Stodolka, X. L. Yang, S. G. Tikhodeev, N. A. Gippius, H. Giessen, Appl. Phys. B 81 (2005) 271-275.
- [18] M. F. Aimi, M. P. Rao, N. C. MacDonald, A. S. Zuruzi, and D. P. Bothman, Nat. Mater. 3 (2004) 103-105.

- [19] S. W. Ahn, K. D. Lee, J. S. Kim, S. H. Kim, J. D. Park, S. H. Lee, P. W. Yoon, *Nanotechnology* 16 (2005) 1874-1877.
- [20] Y. Xia, G. M. Whitesides, *Annu. Rev. Mater. Sci.* 28 (1998) 153-184.
- [21] T. Kim, J. Kim, S. J. Son, S. Seo, *Nanotechnology* 19 (2008) 295302.
- [22] M. Geiger, M. Kleiner, R. Eckstein, N. Tiesler, U. Engel, *Annals CIRP* 50 (2001) 445-462.
- [23] L. J. Guo, *J. Phys. D – Appl. Phys.* 37 (2004) 11 R123-R141.
- [24] S. Y. Chou, P. R. Krauss, P. J. Renstrom, *J. Vac. Sci. Technol. B* 14 (1996) 4129-4133.
- [25] S. Y. Chou, P. R. Krauss, *Microelectronic Engineering* 35 (1997) 237-240.
- [26] Y. Saotome, K. Itoh, T. Zhang, A. Inoue, *Scripta Mater.* 44 (2001) 1541-1545.
- [27] Y. Saotome, K. Imai, S. Shioda, S. Shimizu, T. Zhang, A. Inoue, *Intermetallics* 10 (2002) 1241-1247.
- [28] J. Böhm, A. Schubert, T. Otto, T. Burkhardt, *Microsyst. Tech.* 7 (2001) 191-195.
- [29] Y. Hirai, T. Ushiro, T. Kanakugi, T. Matsuura, *Proc. SPIE* 5220 (2003) 74-81.
- [30] H. Becker, U. Heim, *Sensors and Materials* 11 (1999) 297-304.
- [31] W. L. Johnson, *MRS Bull.* 24 (1999) 42-56.
- [32] T. Zhang, A. Inoue, T. Masumoto, *Mater Trans JIM* 32 (1991) 1005-10.
- [33] J. F. Löffler, *Intermetallics* 11 (2003) 529-540.
- [34] Y. Saotome, T. Zhang, A. Inoue, *Microforming of MEMS parts with amorphous alloys*, *Mater. Res. Soc. Proc.* 554 (1999) 385-390.
- [35] J. Schroers, *JOM* 57 (2005) 35-39.
- [36] J. P. Chu, H. Wijaya, C. W. Wu, T. R. Tsai, C. S. Wei, T. G. Nieh, J. Wadsworth, *Appl. Phys. Lett.* 90 (2007) 034101.
- [37] G. Kumar, H. X. Tang, and J. Schroers, *Nature* 457 (2009) 868-872.
- [38] U. Engel, R. Eckstein, *J. Mater. Proc. Tech.* 125-126 (2002) 35-44.
- [39] B. Eichenhueller, E. Egerer, U. Engel, *Int. J. Adv. Manuf. Technol.* 33 (2007) 119-124.
- [40] www.argor.com
- [41] F. Arias, S. R. J. Oliver, B. Xu, R. E. Holmlin, G. M. Whitesides, *J. Microelectromech. Syst.* 10 (2001) 1 107-112.

- [42] J. Jiang, F. Mei, W. J. Meng, G. B. Sinclair, S. Park, *Microsyst. Technol.* 14 (2008) 815-819.
- [43] J. D. Williams, W. Wang, *Microsyst. Technol.* 10 (2004) 10 699-705.
- [44] S. W. Pang, T. Tamamura, M. Nakao, A. Ozawa, H. Masuda, *J. Vac. Sci. Technol. B* 16 (1998) 1145-1149.
- [45] C. W. Hsieh, H. Y. Hsiung, Y. T. Lu, C. K. Sung, W. H. Wang, *J. Phys. D – Appl. Phys.* 40 (2007) 3440-3447.
- [46] H. L. Chen, S. Y. Chuang, H. C. Cheng, C. H. Lin, T. C. Chu, *Microelectr. Eng.* 83 (2006) 893-896.
- [47] C. J. Wang, D. B. Shan, J. Zhou, B. Guo, L. N. Sun, *J. Mater. Process. Tech.* 187-188 (2007) 256-259.
- [48] N. A. Fleck, G. M. Muller, M. F. Ashby, J. W. Hutchinson, *Acta Metall. Mater.* 42 (1994) 2 475-487.

2. Microstructure characterization techniques

This chapter describes the main methods applied to characterize samples after nanoimprinting. The descriptions (e.g. of the combined FIB-EBSD measurements) are presented in more detail, with the aim of saving precious time for other researchers facing the same challenges. The techniques applied to investigate optical and mechanical properties, i.e. variable angle reflectance and nanoindentation, respectively, will be described in Chapters 4 (optical properties) and 5 (mechanical properties).

2.1. Scanning electron microscopy (SEM)

Scanning electron microscopy (Leo 1530, Zeiss, Germany) was deployed as the main characterization tool for evaluating the quality of the microstructures produced. Imaging was performed with an secondary electron (SE) detector, which enables better topographical contrast. SEM images were also generally used to measure the structure dimensions.

2.2. Electron backscattered diffraction (EBSD)

Electron backscattered diffraction was applied to characterize grain size and orientation in the structured metal. It was performed using an SEM (Quanta 200 FEG, FEI, USA) equipped with an OIMTM system (Hikari detector, AMETEK-EDAX, USA). In particular, detailed scans were performed on the top surfaces of single pillars with diameters down to 130 nm, using a minimum step size of 10 nm for pillars smaller than 250 nm. Selected scans are presented in Chapter 5 as processed orientation maps, indicating grain shapes and crystal orientations. Drift effects due to local charge accumulation were minimized by scanning in low vacuum mode (30 Pa), with an acceleration voltage of 20 kV.

2.3. Focused ion beam (FIB)

A focused ion beam system was used to evaluate the filling quality of the metal in the mold and to investigate the grain distribution within the pillars. In the first case a groove was cut in the mold, after the removal of the excess silver lying on the silicon surface after imprinting, using a Strata DB235 (FEI, USA) or the newer NVision40 (Zeiss, Germany). The grain distribution within the pillars was investigated by slicing shallow-angle cross-sections with the NVision40 FIB system; the contrast in crystal orientation was visualized by SEM SE images and measured in-situ by EBSD (OIM Digiview detector, AMETEK-EDAX, USA). To perform both slicing and measuring in-situ one needs to overcome challenging geometrical constraints (the fixed angle of

54° between the ion gun and the electron gun; an optimal surface tilt angle for EBSD of 70° relative to the e-gun; the tilt angle of FIB cuts of 90° relative to the ion gun; and the shadowing effects of other parts of the sample on the trajectories between guns, pillar and detector).

The solution we found for achieving high-quality measurements was to mount the sample on a 56°-sloped (pre-tilted) sample holder and to make the FIB cuts with a stage tilt angle of 22° (acceleration voltage 30 kV, current 10 pA for both imaging and milling), followed by application of a low-voltage “shower” with 2 kV and 80 pA at a tilt angle of 27° (for 10 s on an area of 20 × 10 μm) to remove the damaged (amorphous) layer prior to the very surface-sensitive EBSD measurements. Then we rotated the stage by 180° and performed EBSD measurements of the cut surfaces with a tilt angle of -6°, while carrying out measurements on non-cut surfaces (pillar top surfaces or base material) with a tilt angle of 14° (EBSD parameters: working distance: 10 mm, acceleration 15 kV, dynamic background and normalized intensities). Examples of these measurements are shown in Figs. 5.5 and 5.6.

2.4. Other techniques

Optical microscopy was used regularly as a rapid technique for evaluating structure quality for dimensions larger than 1 micrometer. In addition, X-ray diffraction (XRD, PW 1729 x-ray generator with Cu-source, Philips, Netherland) was applied to confirm the uniform orientation of silver single crystals and to orient them before cutting in plates with defined orientation. To measure film thicknesses, either a surface step profiler (Alpha-Step 500, Tencor Instruments, USA) or ellipsometry (M-2000F spectroscopic ellipsometer, J.A. Woollam Co. Inc, USA) was used, the latter also being applied to investigate the complex dielectric function of metallic plates.

3. Development of the nanoimprinting technique¹

This chapter describes the development of a setup and experimental procedure for nanoimprinting, presented in combination with some preliminary results which significantly influenced the evolution of the fabrication procedure.

The outline of the chapter reflects the work schedule followed to develop the fabrication process, the goal of which was to develop a microstructuring method based on metal forming, capable of producing high-aspect-ratio metallic structures suitable for optical devices. The chapter begins by describing the selection of the material used for producing the mold and its microfabrication procedure, followed by a description of the suitable metals chosen. A preliminary investigation of the necessary forming conditions determined the characteristics of the imprinting setup employed. Then the removal of the mold or the metal in excess and the challenges associated with them are described. The chapter concludes with a rapid overview and discussion of the structures obtained, and a review of the most important process parameters applied.

¹S. Buzzi, F. Robin, V. Callegari, J. F. Löffler, “Metal direct nanoimprinting for photonics”, Microelectr. Eng. 85 (2008) 419-424.

3.1. Dielectric mold: material selection and fabrication procedure

The criteria for selecting the mold material were mainly based on the following requirements: sufficient thermal and mechanical stability for sustaining the imprinting conditions; chemical stability in contact with the metals; microstructuring capabilities; and optical (dielectric) properties.

Silicon was the first choice, since it satisfies outstandingly all the above-mentioned conditions [1-4], and it is by far the dielectric with the most numerous microfabrication processes and infrastructure tested. In addition, it can be easily removed by wet etching in a KOH aqueous solution, a medium which does not etch noble metals such as silver or gold [5] (but see also the related difficulties presented in section 3.5). Besides the material's brittleness, which hinders any repeated use of the molds where there are high-aspect-ratio structures but is not too problematic for single imprints with soft metals, the only limitation for silicon is its light absorption at visible wavelengths, due to the band gap of 1.1 eV, which limits its use in optical devices to infrared radiation. Silicon was therefore adopted generally as mold material, but tests were also performed with silicon wafers covered by a layer of either 1.5 μm thermally grown SiO_2 or 1.2 μm SiN_x deposited by plasma-enhanced chemical vapor deposition (PECVD), materials which are also transparent to visible light. The success of these tests demonstrates that the fabrication possibilities of the nanoimprinting technique, demonstrated in this project using silicon molds, can be easily extended to other mold materials possessing sufficient chemical, thermal and mechanical stability (Fig. 3.1).

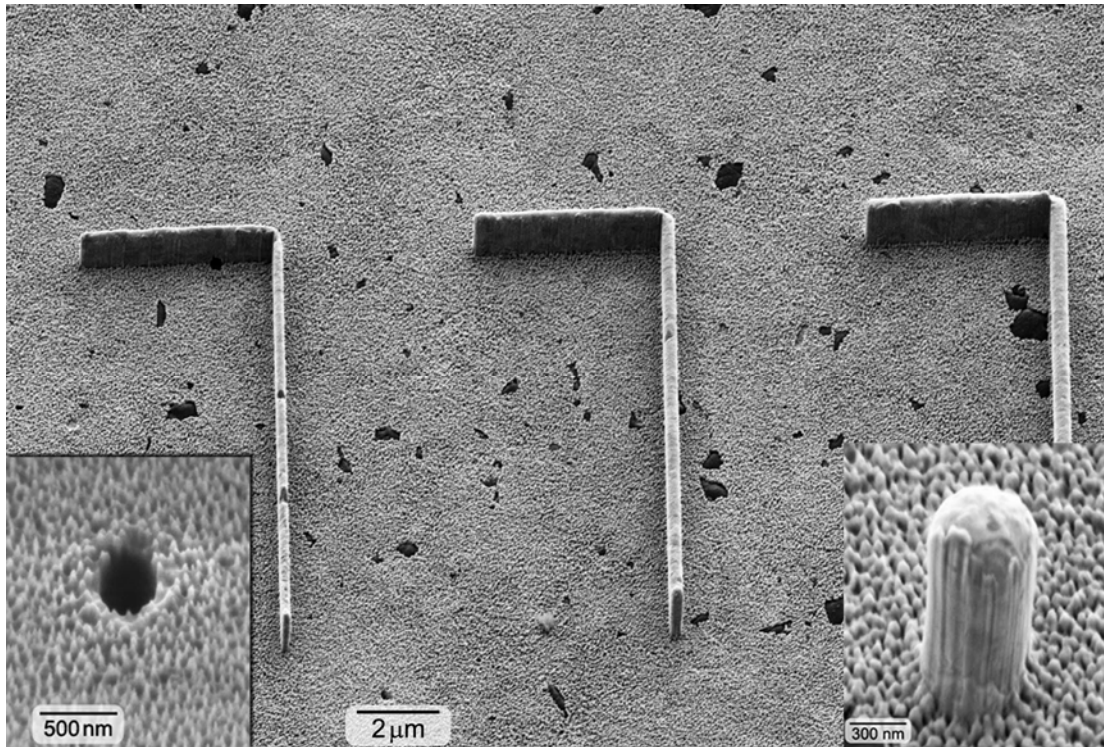


Fig. 3.1: Gold plate showing “L”-shaped lines (widths 250, 350 and 410 nm) and a pillar (diameter 560 nm), prepared by nanoimprinting at 400°C under a pressure of 300 MPa in a SiN_x mold, after mechanical removal of the mold. The surface roughness of the base material is the result of overetching of the photoresist mask during preparation of the SiN_x mold (inset, bottom left), and was also accurately reproduced by the metal. The mechanical removal resulted in slight mechanical damage, seen as stripes on the structures. The dark particles visible in the base material are SiC particles caused by insufficient surface etching after polishing during the gold plate preparation (see section 3.4).

For mold fabrication, silicon (100) wafers were patterned by lithography and dry etching techniques. Where the minimum structure dimension was larger than 1 μm conventional UV lithography was employed, with a chromium mask and a 1.4 μm photoresist (Shipley S1813). A typical design consisted of lines with widths of 1 and 2 μm and squared holes with a width of 4 μm, etched in the silicon wafer by ICP-DRIE (Fig. 3.3a, discussed later). As discussed in section 1.2, this process enables the production of deep cavities with vertical side walls in the silicon by alternating etching and passivation steps, but it generates pronounced wall roughness (horizontal lines corresponding to the etch steps, as shown in Fig 1.2b and the inset to Fig. 3.3a, where 26 etching cycles were used, resulting in a structure depth of 7-8 μm).

To produce submicrometer structures, electron-beam lithography was used (RAITH150, Raith GmbH, Germany). This tool makes possible the design of

discretionary patterns, which were written with 30 kV acceleration voltage in a PMMA (polymethylmethacrylate) layer with a thickness of 50-200 nm, deposited on the wafer by spin coating. This layer had the dual function of acting as a photoresist and as a protective mask for subsequent mold etching. After photoresist development, where regions irradiated by the electron beam were dissolved in a solution of 25% methyl isobutyl ketone (MIBK) and 75% isopropanol, the patterns were transferred to the dielectric (usually silicon) by dry etching. To obtain smoother walls, etching was generally performed in this case by RIE (reactive ion etching), a process which involves a single etching step. The minimum lateral size achieved was 130 nm for cylindrical holes and 110 nm for lines. The structured wafers were finally covered with a protective photoresist layer and sawn into $5 \times 5 \text{ mm}^2$ pieces. Before imprinting, the protective layer was removed and the wafers cleaned by ultrasonic bath in acetone and ethanol.

3.2. Metal selection

The two main requirements considered in evaluating the metal were extensive formability and good optical properties (low light absorption).

Gold and especially silver are known for having the lowest light absorption in the near infrared [6]. These metals also exhibit very extensive malleability and have a long history of processing by forming, characteristics which make them optimal candidates. However, at the outset of this study it was not known whether these metals could be formed to reliably produce pillars at the desired small sizes and high aspect ratios, because of the limited literature and the possible size effects which appear in crystalline materials when the structure dimensions are reduced to sizes comparable to the grain dimensions (see section 1.4).

On the other hand, as mentioned in section 1.3 the recently-developed bulk metallic glasses [7-9] have demonstrated good formability, also at the submicrometer scale [10-12]. These alloys have two significant advantages in microforming processes: they possess an amorphous structure, and as such are not subjected to the size effects observed in crystalline metals; and they can be superplastically formed at low pressure within a specific temperature range. However, at the beginning of this

project their optical properties were almost unknown, limited to a few measurements in thin film metallic glasses [13-15].

A preliminary investigation of the optical properties of metallic glasses in comparison to gold and silver was therefore performed, to clarify whether these alloys possess sufficiently low absorption to be suitable for potential applications in high-quality optical devices.

Metallic glass plates of selected compositions (Zr-, Pd-, Au- and Fe-based alloys) were prepared by arc melting, casting in a copper mold and polishing with a 3 μm diamond suspension, analogous to the sample preparation described in detail in Ref. [16]. A silver plate (Ag 99.9985%, Alfa Aesar, USA) was polished correspondingly. The permittivity (dielectric function) of the plates was measured by ellipsometry in the visible and near infrared range. At these wavelengths, metallic materials possess a complex permittivity, composed of a negative real component and an imaginary component, which corresponds to absorption losses. For optical applications it is critical to have an imaginary part as small as possible. In addition, more negative real values are desirable because they facilitate a larger permittivity contrast when the metals are associated with a dielectric material (having a positive, real permittivity), resulting in stronger optical effects. The dielectric functions of a representative metallic glass (Vit105, $\text{Zr}_{52.5}\text{Ti}_5\text{Cu}_{17.9}\text{Ni}_{14.6}\text{Al}_{10}$) and a silver plate are compared in Figure 3.2.

All materials showed the typical metal behavior, with a negative real component $\varepsilon_1(\lambda)$ and an imaginary component $\varepsilon_2(\lambda)$, both dependent on radiation wavelength. The metallic glass had considerably greater imaginary values as well as lower negative real values than silver, meaning that its application in an optical device would imply significant losses and weaker optical effects compared to devices made with silver. The other metallic glasses investigated showed behavior similar to that of Vit105. The existence of metallic glasses with better optical properties cannot be excluded, but their amorphous, disordered structure involving several components makes it unlikely that a metallic glass with properties comparable to silver will be found.

Based on these results, silver and gold were selected as metallic components and their formability at micro- and submicrometer scales was investigated.

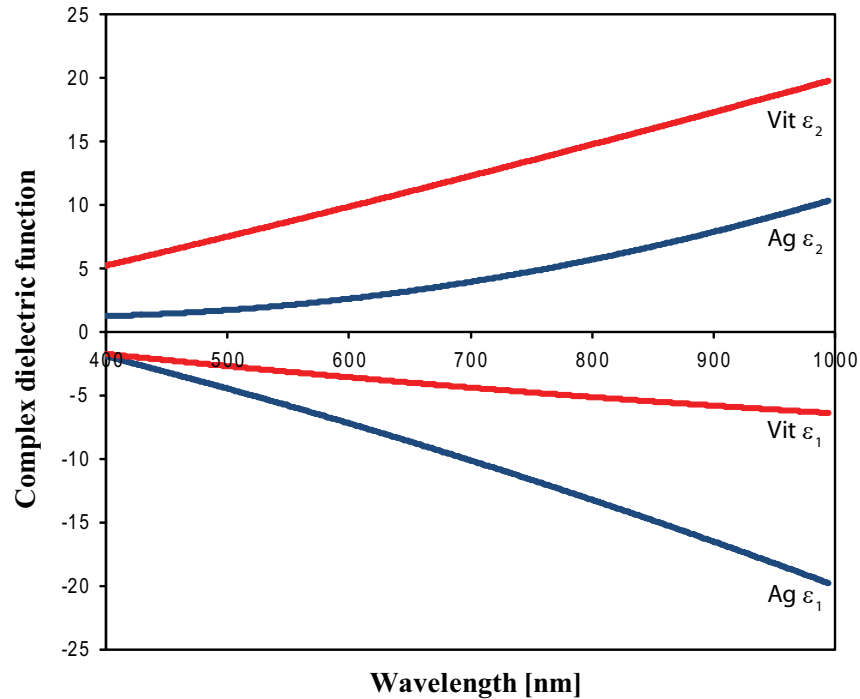


Figure 3.2. Complex permittivity (dielectric function) $\epsilon = \epsilon_1 + i\epsilon_2$ of pure silver and the metallic glass Vit 105 ($Zr_{52.5}Ti_5Cu_{17.9}Ni_{14.6}Al_{10}$) as a function of radiation wavelength.

3.3. Preliminary investigation of the necessary forming conditions (imprinting temperature)

Initial imprinting experiments were carried out on silver plates using a standard compression machine (Schenck Trebel, Germany), to investigate the minimum requirements for the forming device. Before imprinting, 0.5-mm-thick plates were polished and annealed for 30 min at 700°C in argon atmosphere, to achieve material recovery and recrystallization. The surface of the plates was then rapidly etched in 30% HNO_3 to remove contamination and a possible oxide layer. A silicon mold with 1- and 2- μm lines and 4 μm holes was used (Fig. 3.3 a).

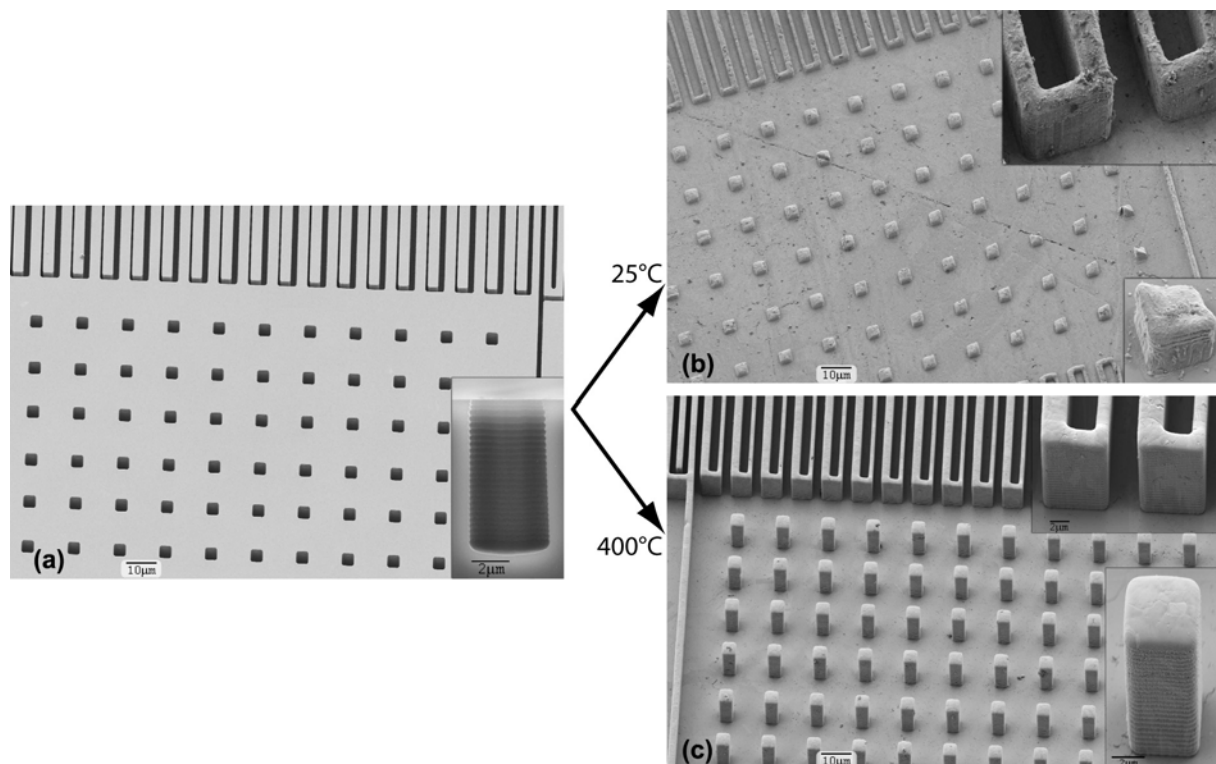


Figure 3.3. Influence of imprinting temperature on formability. (a) Silicon mold with 1- and 2- μm lines and 4- μm holes. The wall roughness (horizontal lines), visible in the cross-section of a hole (inset), is caused by the 26 etching cycles during DRIE mold preparation. (b) Ag plate after imprinting at room temperature and mold removal by wet chemical etching. Only incomplete filling and bad surface quality were achieved. (c) Ag plate after imprinting at 400°C (same maximum pressure of 300 MPa). At this temperature filling was complete in all structures and even the small wall rugosity of the molds was reproduced by the silver, indicating negligible mold wear.

Even after 2 hours at a pressure of 300 MPa, only incomplete filling associated with bad surface quality was achieved, as shown in Fig. 3.3b, which illustrates an SEM image of the silver plate after mold removal by KOH etching. This sample indicates that hot-forming is necessary to obtain complete filling, because the elevated temperature fosters dynamic recovery mechanisms which suppress the work hardening effects responsible for reduced metal formability [17-18]. A more sophisticated tensile/compression machine (Zwick 1474, Zwick GmbH, Germany) was therefore employed, enabling compression under vacuum at elevated temperatures. A silver plate imprinted at 400°C with the same mold design and the same pressure of 300 MPa is shown in Fig. 3.3c. Complete filling combined with excellent surface quality was now achieved, even reproducing the wall roughness of the holes produced by the cycled etching during mold preparation. These results indicate that high-quality microstructures with high aspect ratios can be produced by

imprinting, but that elevated temperature is a mandatory condition. This observation contrasts with imprinting experiments recently published by Hsieh *et al.* [19], who obtained rough ball-like microstructures overlapping the imprinted structures in aluminum thin films embossed at a temperature above the recrystallization temperature. These overstructures, attributed to grain growth, hindered accurate imprinting. In their case the pressure of 300 MPa was applied for only 1 minute; the metal probably did not have enough time to complete all forming and recovery processes. In the case of fast processing it is actually typical to observe better surface quality after cold-forming than after hot-forming [17-18].

The activation of dynamic recrystallization during forming at 400°C is confirmed by the various grain sizes observed by SEM in the severely-deformed regions (where crystals are smaller than the structures), and in the almost undeformed regions (which show large grains), as shown in Fig. 3.4, and the same phenomenon is observed even when starting with a single-crystalline plate (Figs. 3.13 and 5.2).

The upper limit for the imprinting temperature is given by the most restrictive condition among the following: (i) reactions between mold and metal; (ii) plastic deformation of the mold; (iii) the temperature limits of the forming setup. Using silicon molds, the maximum imprinting temperature corresponds to about 500°C for silver (onset of plastic flow in silicon under a pressure of 300 MPa [2]), but it is only 363°C for gold, because at this temperature gold and silicon form an eutectic [4].

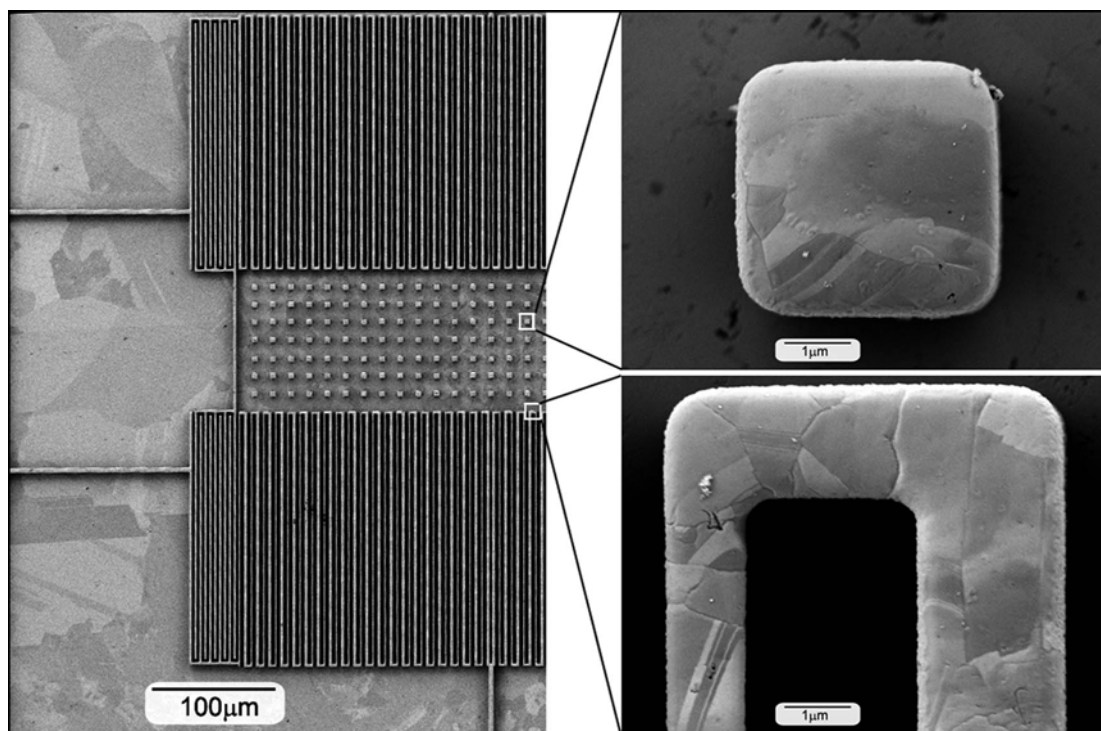


Fig. 3.4. Top view of the silver plate after imprinting in a silicon mold and subsequent mold removal (sample already shown in Fig. 3.3c, with 4- μm -wide pillars and 1- and 2- μm -wide lines). Large grains of 10-100 μm are visible in the nearly undeformed metal, on the left-hand side of the picture. In contrast, the severely deformed material forming pillars (top inset) and lines (bottom inset) presents a submicron grain size with several twins.

3.4. Imprinting setup and metal plate preparation

Because of the preliminary results presented in the previous section, the high-temperature compression machine Zwick 1474 was adopted for imprinting. To achieve maximum stress homogeneity over the whole surface (a crucial condition to prevent breakage of the brittle mold), the machine was actuated in tensile mode with an inverter, calibrated to have very parallel compression surfaces (Fig. 3.5a). A closed-die system, with a lateral confinement enveloping both silicon and silver, was added to avoid excessive metal flow on the sides, as shown in Figs. 3.5b-c.

After mounting of the sample, the compression chamber was evacuated ($p < 5 \times 10^{-5}$ mbar) to achieve complete filling and prevent oxidation; then it was preheated for 45 min at forming temperature (typically 400°C for silver and 300°C for gold) to create homogeneous starting conditions and allow the rolled metal of polycrystalline plates to recrystallize (achieving its highest ductility). An increasing

pressure of up to 300 MPa was then applied, at a constant strain rate of $5 \times 10^{-5} \text{ s}^{-1}$, and the maximum pressure was usually maintained for 10 minutes. Afterwards the chamber was cooled, maintaining the sample under pressure until it reached 50°C . The metal-mold composite was finally removed from the lateral confinement using a hand press.

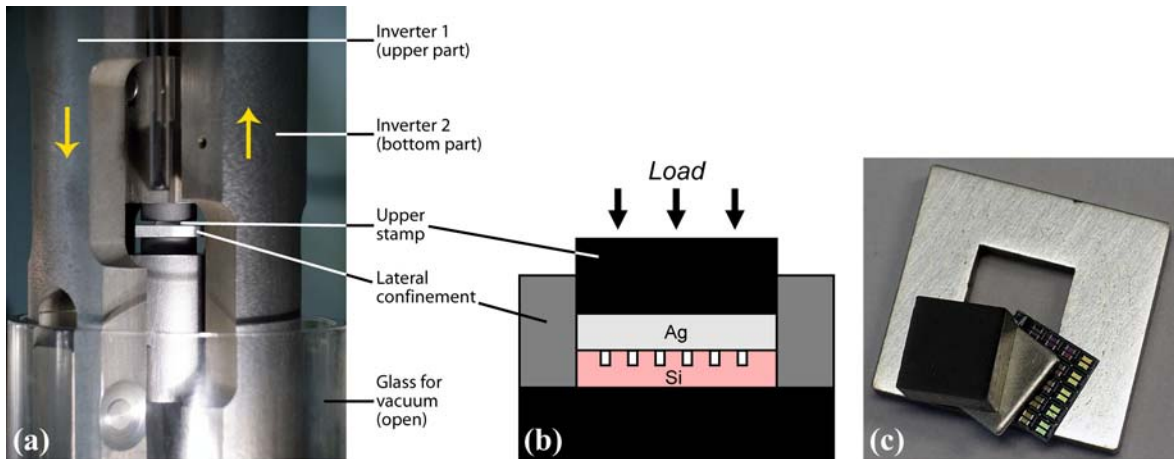


Fig. 3.5. Imprinting setup. (a) Close-up of the high-temperature compression machine. (b) Sketch and (c) picture of the closed-die imprinting system.

Metal plate preparation before imprinting consisted of rolling the metal piece to achieve the desired thickness, punching into $5 \times 5 \text{ mm}^2$ units, and parallel polishing of both surfaces with SiC4000 grinding paper. Most of the experiments were performed with a 0.5-mm-thick, high-purity silver foil (Ag 99.9985%, Alfa Aesar, USA), but commercially-pure silver (99.9%, UBS, Switzerland) and gold (99.99%, UBS, Switzerland) were also tested and showed comparable formability.

Few minutes before imprinting, the plates were etched rapidly to remove a possible oxide layer or other contamination. This step was performed by immersing the silver plates for 1 min in 30% HNO_3 and the gold plates for 5 min in aqua regia (75% HCl , 25% HNO_3), followed by rinsing in water and ethanol and drying with an air flow. Especially in the case of silver, which is rapidly etched, the surface was very rough after this step (apart from the case of single-crystalline silver plates, as discussed later), as shown in Fig. 3.6d. It was nevertheless observed that deep etching was indispensable. In fact, because gold and silver are soft metals, during polishing silicon carbide particles from the grinding paper are embedded in their surfaces [20]. If the contaminated upper layer of the plate is not completely removed, particles will

be embedded in the imprinted structures, as was the case in the sample shown in Fig. 3.1. Paradoxically, a short etching time is even worse than no etching at all, because it results in exposition of embedded particles at the surface, where they are most detrimental for the imprinting process (see Figs. 3.6a-c).

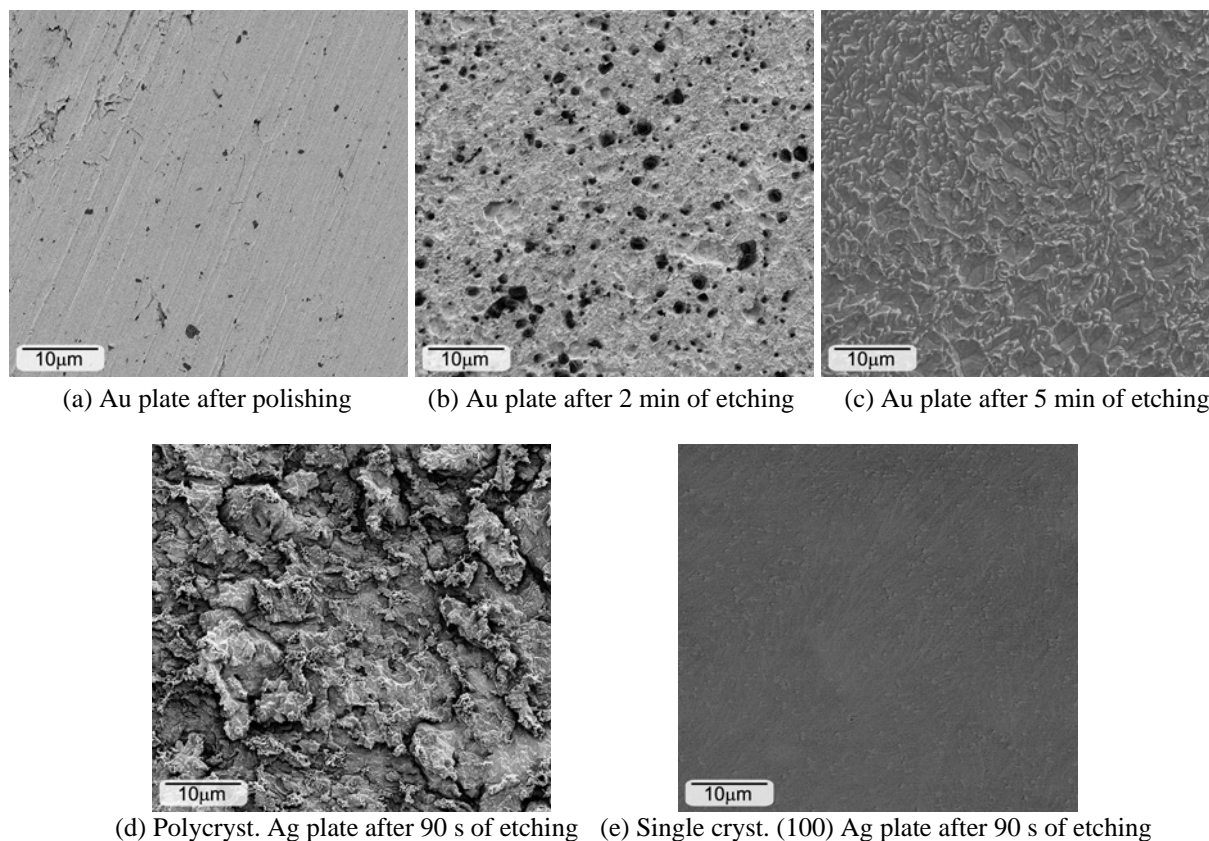


Fig. 3.6. (a)-(c) Gold plates after polishing with SiC4000 and (a) no etching; (b) 2 min of etching; (c) 5 min of etching in aqua regia. A short etching time removes the top metal layer, bringing to the surface numerous SiC particles embedded just below the metal surface (Fig. 3.6b). Sufficiently long etching time is therefore required to completely remove the upper layer containing the particles and achieve a clean surface suitable for nanoimprinting (Fig. 3.6c). (d) Polycrystalline (rolled and polished) silver plate after etching for 90 s in 30% HNO_3 . The etching rate is considerably higher than for gold in aqua regia and the plate turns matte because of the surface roughness introduced. (e) Non-polished, single-crystalline plates, on the other hand, become very smooth and shiny after nitric acid treatment because of anisotropic etching.

For a better understanding of the influence of the original lattice orientation in the plate on the formability and grain orientation in the imprinted microstructures, single-crystalline silver plates were also prepared, with two orientations: (100), which results in eight equivalent slip systems; and (321), with one particularly favored slip system. The plates were cut from a single crystal by spark erosion after crystal

alignment using X-ray diffraction (XRD). The single crystal was grown in-house using the Bridgman method starting with Ag 99.99% pellets (Metalor, Switzerland). After etching with nitric acid, these plates were very shiny and showed an extremely smooth surface (Fig. 3.6e), because of anisotropic etching and a non-deformed surface layer (these plates did not need mechanical polishing since they had already been cut with very parallel surfaces). No significant difference in formability between the two plate orientations was observed, and the samples recrystallized during imprinting. The crystal orientation in the microstructures was not uniform, but a strong texture was observed, the most frequent orientation being partially related to the original plate orientation (see section 3.7).

3.5. Mold release

The most difficult fabrication challenge to be overcome in order to reliably produce high-aspect-ratio submicrometer freestanding structures on a metallic plate (such as in Figs. 3.10, 3.14, 4.1, 4.2 and 5.1), was the removal of the silicon mold without any relative movement between the silicon and the metallic plate, which would have torn the structures away from the base plate (Fig. 3.7). A favorable size effect occurring in submicron metallic structures, which show considerably enhanced mechanical strength compared to larger structures (see Chapter 5), is not sufficient to withstand the large forces generated in this step.

Successful mold removal is particularly difficult to achieve when only a small fraction of the mold is patterned with submicrometer structures. Where there are large-area, deep cavities, such as those in Fig. 3.3 (also corresponding to the sample shown in Fig. 3.11), silver and silicon are instead sufficiently interconnected to maintain their relative positions until the silicon is completely etched. Even when they lie on the same plate, small structures are more subject to tearing off than large ones (see Fig. 3.7c, where the larger 1 μm “L” structure maintained its position with only slight damage, while the 250 nm structure was torn off). There are multiple causes for the relative movement. On the one hand, a catalytic effect of silver on the silicon etching was observed, the reaction being considerably faster at the silicon-silver interface than on the reverse side of the silicon wafer; many hydrogen bubbles

were therefore generated at the interface, starting at the sample edges, creating forces which tended to separate the plate from the wafer. On the other hand, mold and plate also separated even without bubble generation (for example when the sample was immersed in pure warm water or when the mold had a SiO_2 or SiN_x layer at the interface, as in the sample shown in Fig. 3.1; in these cases no etching takes place). Here the driving force for separation is presumably a combination of material stresses and capillary forces. While a separation of the microstructures from the base plate can be an advantage when the goal is the production of microparts, for example for MEMS (see Fig. 3.7c), this phenomenon was not desirable in the present study, which aimed at structures in a precise position to enable rapid evaluation of the imprinting process and subsequent mechanical characterization.

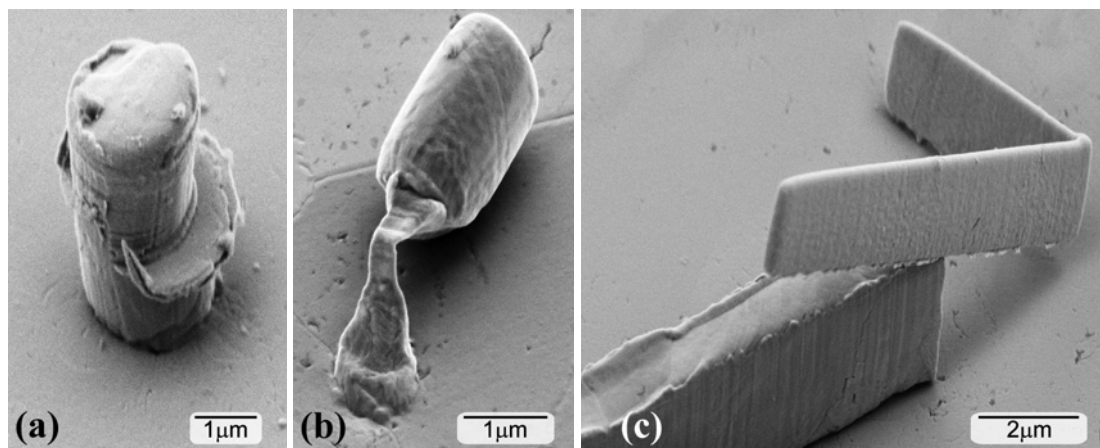


Fig. 3.7. Silver structures damaged or completely torn from the base plate by relative movement between silicon and metal plate during mold wet etching. In (c), the thinner (250 nm) “L” structure was raised and landed on a larger (1 μm) “L” structure, which maintained its position and was only slightly damaged by the silicon movement.

Two approaches were combined to avoid relative movement between the mold and the metallic plate during etching. First, during the cutting step of the silicon wafer, performed after its microstructuring to produce the $5 \times 5 \text{ mm}^2$ molds, an additional 150-200- μm -deep groove was cut with the 30- μm -thick wafer saw, close to the mold edges (Fig. 3.8a). During imprinting the metal partially fills these grooves, helping to keep the wafer in position during etching. The silicon mold is stable enough to survive the imprinting pressure despite the deep grooves, where cracks can easily originate. Second (and more effectively), the sample edges were insulated from the KOH solution and it was initially etched through the silicon mold in the central

region, where the structures were usually located. The rest of the wafer was etched in a second step, once the structures had already been released and lateral movements were no longer problematic.

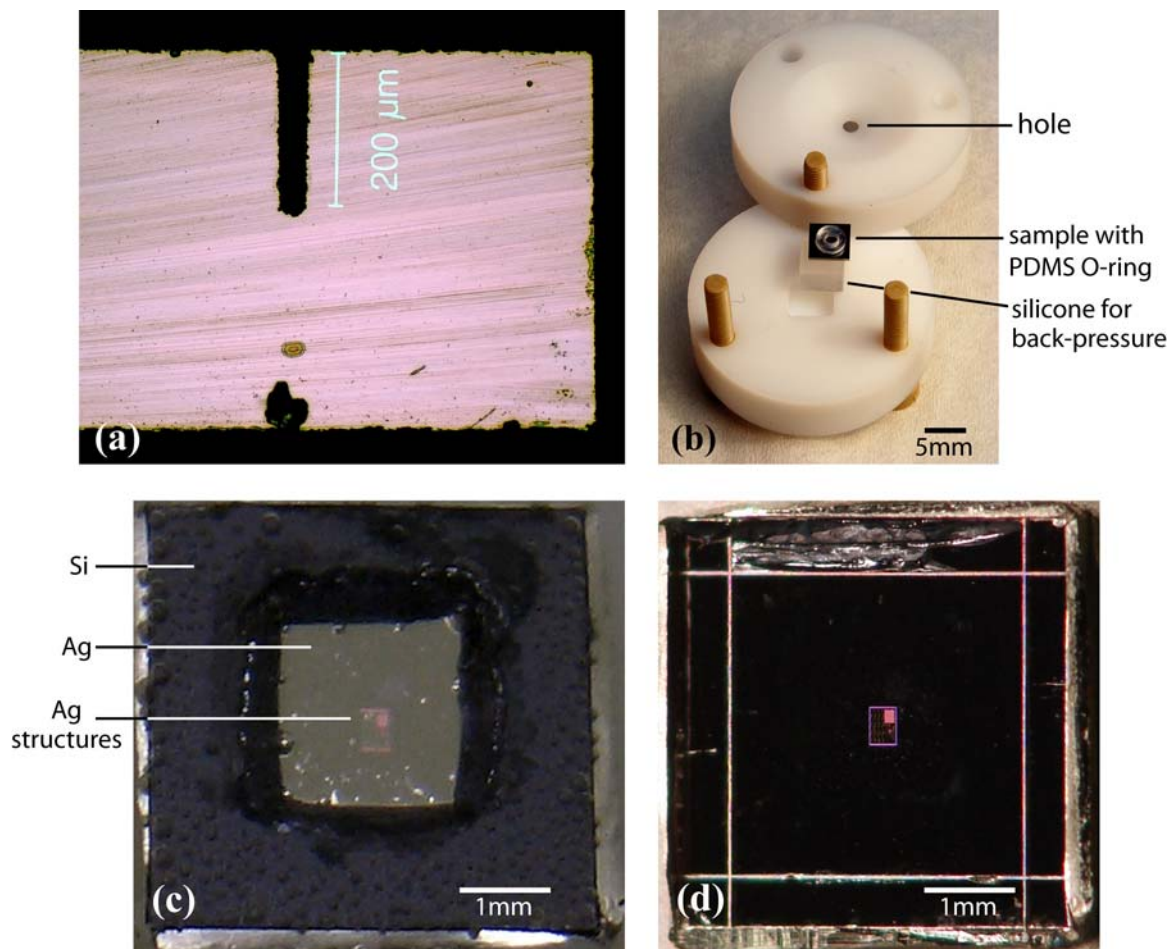


Fig. 3.8. Techniques employed to avoid structure damage during mold removal by wet etching. (a) Cross-section of the silicon mold, with a 200- μm -deep groove close to the mold edge. (b) Open Teflon holder for wet etching, with a 2 mm hole sealed by a PDMS O-ring, making it possible to etch the silicon mold only in the central region. (c) $5 \times 5 \text{ mm}^2$ silver sample after etching of the silicon in the central region. The microstructures are already visible in the middle, appearing pink because of interference effects. (d) The same silver sample of (c) after complete removal of the silicon mold. In contrast to (c), where it is grey, the silver surface appears black because the picture was shot with side illumination, to enhance the structure brightness. The straight, bright lines visible close to the edges are silver reliefs corresponding to the lateral grooves in the silicon mold shown in (a).

The insulation of the sample edges from the etching solution was complicated by the small sample size. Simple methods covering the edges with silicone, glues, sputtered gold or PECVD-deposited SiN_x failed, because the protective layers were rapidly raised and subsequently removed by the hydrogen bubbles generated.

Successful insulation was obtained by constructing a Teflon[®] holder with a 2 mm hole, corresponding to the center of the mold, sealed with a self-made PDMS (polydimethylsiloxane) O-Ring. Despite the round shape of the O-ring, anisotropic silicon etching results in a square-shaped hole (Fig. 3.8c), because the (111) surfaces are etched significantly slower than the others. Moderated back-pressure for optimal sealing was supplied by a pressed silicone cube placed below the sample (Fig. 3.8b). Due to the hydrophobicity of the Teflon and the small hole size the generated hydrogen tended to form a big, stable bubble which stuck at the holder hole, insulating the sample from the solution and significantly slowing down the etching process. The bubbles were therefore removed from the holder opening by applying a cyclic flow of the KOH solution, obtained by placing a pipette above the hole connected to a silicone tube sealed at the other end and alternately pressed by a peristaltic pump.

With the described setup a good success rate (~66%) was achieved. After etching, the samples were cleaned by immersing for 1 min in 20% acetic acid, which removed occasional dark deposits on the metal surface, and rinsed with water and ethanol before drying with a nitrogen flow. Due to interference effects, the microstructures are easily visible even to the naked eye (Fig. 3.8d).

3.6. Removal of excess metal to produce Si–Ag photonic crystals

In most samples the structured metallic plates were released from the mold after imprinting. To produce metallo-dielectric photonic crystals, however, the goal was also to exploit the mold (made of an optically-suitable material) as a component of the optical device and use the imprinting process to metalize the periodic holes. This idea implies the removal of the metal, which after imprinting was in excess on the mold surface; the same step is also required in the IC industry after interconnect metallization. As mentioned in section 1.2.1, the standard industrial procedure for removing the excess metal is chemical mechanical polishing (CMP). The main difficulty of applying this process to our samples laid in their small size, which complicated the planarization (the plate is polished faster at the edges than in the central region), in addition to the very thick metal layer to be removed. A non-

conventional approach was therefore employed, where the small size is an advantage instead of a problem: the application of a large shear force. The thickness of the silver layer on the silicon surface was at first reduced from the initial 150-500 μm (depending on the original plate thickness) to a few tens of micrometers by parallel mechanical polishing with SiC1200 and SiC4000 grinding paper, until the underlying silicon was visible at the sample edges. Then the sample was scraped with aluminum, a material which is harder than silver but softer than silicon, so that the mold was not damaged. The large shear force, introduced by scraping, cracked the imprinted silver at the level of the silicon top surface, leaving silver in the holes and removing all the metal lying above. This process works well for thin, high-aspect-ratio cavities, while in low-aspect-ratio structures a fissure forms between silver and silicon (Fig. 3.9); for aspect ratios below 0.5 the silver can sometimes even be pulled out of the cavities. This phenomenon is, however, not problematic because the targeted optical devices contain high-aspect-ratio metallic structures.

For optimal optical quality a rapid CMP step was applied to the final samples (see Chapter 4) after the previously-described procedure to remove possible small remnants of smeared silver from the silicon surface via a colloidal suspension of 30 nm silica particles (Syton SF1, Logitech, UK) [21]. Using this procedure very homogeneous periodic structures were obtained over extended surfaces, demonstrating the suitability of nanoimprinting for preparing such composites, as presented in the next chapter (see Fig. 4.3). For large-scale production, where bigger samples are used, the standard CMP would of course replace the application of shear force used here. In addition, the initial silver thickness should be optimized according to the depth and density of the cavities to be filled; a thin metallic film on the order of at most a few microns should be sufficient. Such a thin film could, for example, be deposited on the dielectric by sputtering or thermal evaporation, processes which facilitate large area coverage with pure metals but cannot fill high-aspect-ratio holes (see section 1.2.2). The metal is then forced into the holes in a subsequent imprinting step.

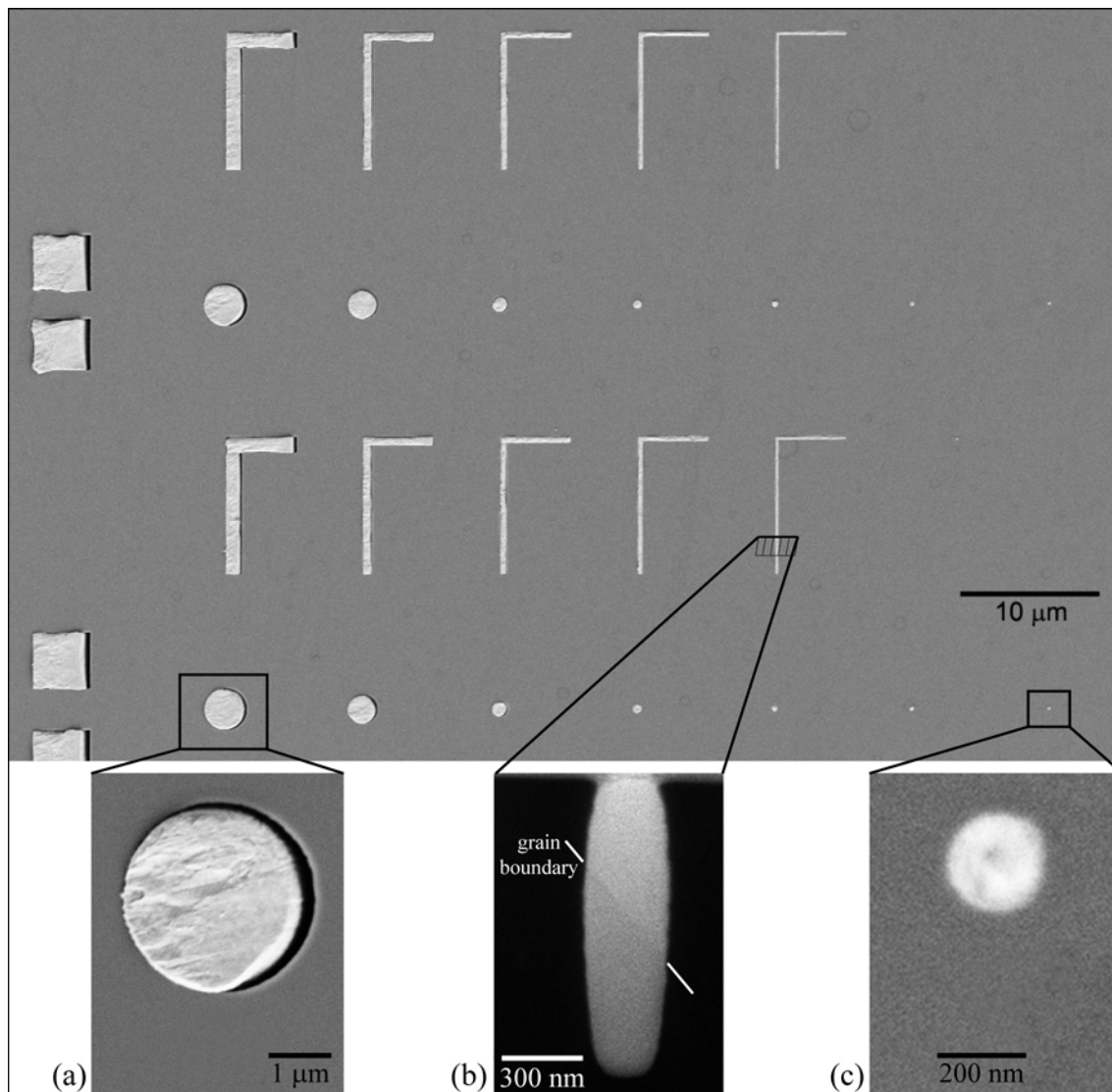


Fig. 3.9. Silicon wafer with cylindrical and “L”-shaped holes filled with silver, with widths ranging between 0.25 and 4 μm , produced by imprinting the metal at 400°C under a pressure of 200 MPa and subsequent mechanical removal of the excess silver, lying on the top of the wafer, via a large shear force. Images at bottom: (a) enlarged view of a 3 μm structure with low aspect ratio (0.8), presenting a fissure between silver and silicon; (b) FIB cross-section of the thinnest “L” line, with a maximum width of 330 nm and an aspect ratio of 5, showing complete filling and a sloped grain boundary; (c) enlarged view of a 250 nm structure with high aspect ratio (3.5), showing no gap between Ag and Si.

The FIB cross-section illustrated in Fig. 3.9b shows that with the proper imprinting conditions complete filling can be achieved, even in the thinnest cavities, with no gap between metal and silicon mold. The silver even filled the lateral voids, caused by the mold undercut during its preparation (hole broadening below the surface due to an excessive chemical component in the etching, resulting in slightly isotropic etching). This indicates on the one hand that the pressure in the hole is

multiaxial and high enough to have flow in every direction, and on the other it shows that the silicon mold's wear is negligible even in the highly-loaded regions. There is therefore no need to protect the silicon mold with a hard coating (such as SiN_x or SiC), as had to be done by several groups to imprint metals at room temperature [22-24]. To visualize the complete filling in all cavities without shear-force artifacts (gaps in low-aspect-ratio structures caused by silver polishing), it is nevertheless faster to remove the mold after imprinting. Fig. 3.10 shows the metal filling in a mold with the same pattern, but prepared with 10 etching steps by DRIE; the significant wall roughness (horizontal steps) introduced in this process did not prevent the silver from filling every void, even reproducing the wall topography, and the number of horizontal lines on the microstructures confirms the complete filling of the mold.

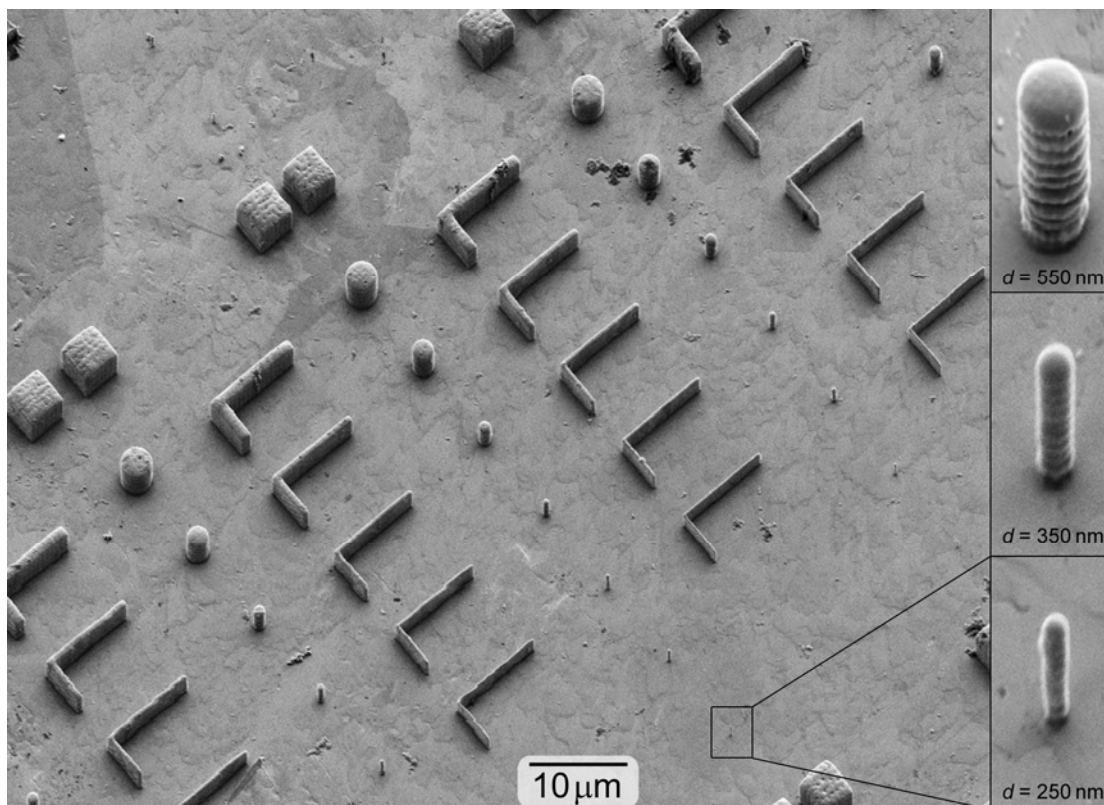


Fig. 3.10. Microstructured silver plate after forming at 400°C with a pressure of 300 MPa and removal of the silicon wafer by KOH etching. The mold was prepared by ICP-DRIE (10 cycles), resulting in great wall roughness accurately reproduced by the silver, as is also clearly seen in the enlarged views (insets) of the pillars with diameters $d = 250\text{-}550$ nm.

3.7. Nanoimprinting results (formability)

3.7.1. Obtained structures and potential of the nanoimprinting technique for large-scale production

As shown in Figs. 3.3c and 3.10, silver structures with sizes between 250 nm and 4 μm and with aspect ratios of up to 5 were successfully produced by imprinting and mold removal, and showed excellent uniformity over large areas. The nanoimprinting limits were pushed further towards smaller sizes (down to 130 nm) and higher aspect ratios (up to 13) in other samples, discussed in the following chapters (see e.g. Figs. 4.1, 4.2, 5.1); and the potential for further improvements is not yet exhausted. The uniformity of the imprinted structures over the whole die area of $5 \times 5 \text{ mm}^2$ is illustrated in Fig. 3.11, which shows an overview image of the sample represented at high magnification in Fig. 3.3c. The process developed here is therefore a valid and relatively simple technique for producing large quantities of high-aspect-ratio metallic micro- and nanostructures.

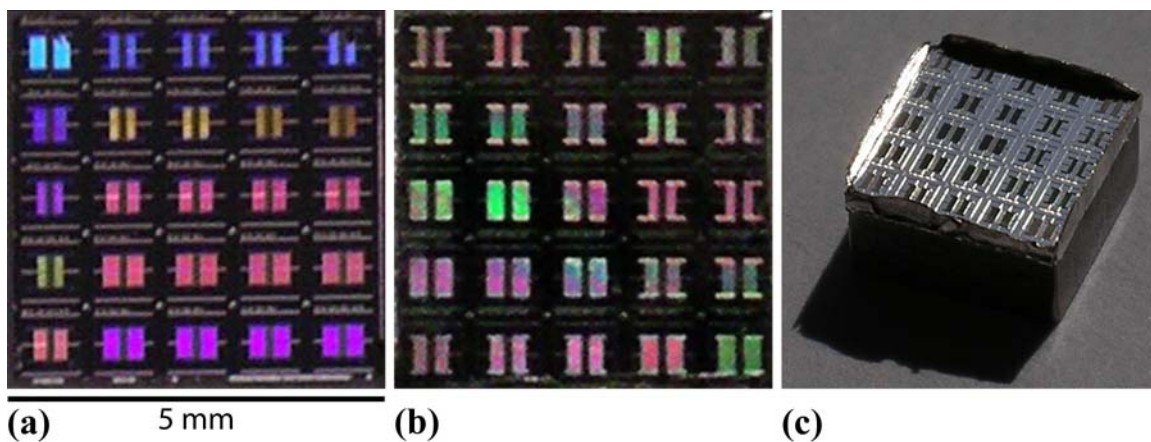


Fig. 3.11. Overview images of a silicon mold and an imprinted silver plate. (a) $5 \times 5 \text{ mm}^2$ mold. The design reproduces 25 accelerometers and was prepared in the framework of the class “Embedded MEMS Lab” (Prof. C. Hierold, ETH Zurich). (b) and (c): corresponding silver plate after imprinting and mold removal, showing good filling over the whole surface (structures consisting of 1- and 2 μm lines and 4 μm holes, see Fig. 3.3). The colors in (a) and (b) are caused by interference effects.

The technique can of course also be applied easily to structures larger and/or with lower aspect ratio. There, and if targeting an industrialization, the process should be optimized with the particular aim of fast production at reduced costs, which means in

particular repeated use of the mold, because mold fabrication comprises the most expensive and time-consuming step in the process. This result may be achieved by combining tougher mold materials, such as SiC; a favorable structure design with limited aspect ratio and sloped walls; thin lubricant layers; post-imprinting cooling without pressure (exploiting the different thermal expansion between metal and mold); and an accurate demolding procedure. Repeated use of the molds for the high-aspect-ratio structures investigated in this study is instead not considered verisimilar without seriously damaging the metallic microstructures during demolding. The quality of the structures achieved, combined with the difficulty and elevated cost of producing them via other methods, could nevertheless make this technique interesting even if the molds are used only once. If the mold itself is part of an optical (or electronic) device, it would in any case be used only once. The possibility of using silicon as mold material, which can be microstructured easily and relatively cheaply by exploiting the many microfabrication plants and techniques, would help to keep the costs of one-way molds within acceptable limits. For large-scale production e-beam lithography should also be replaced by faster and cheaper lithographic methods such as ultraviolet, nanoimprint or interference lithography. Another significant improvement to scale up the process would be to substitute uniaxial compression with isostatic compression; this upgrade would avoid alignment issues and force limitations, making possible parallel imprinting over very large areas.

3.7.2. Filling behavior

In some samples, prepared using molds with submicrometer, high-aspect-ratio holes, a fraction of the structures (pillar) showed incomplete filling. Their top surfaces presented smooth sloped faces, which correspond to low-index crystalline planes instead of reproducing the rounded tip of the mold hole (Fig. 3.12).

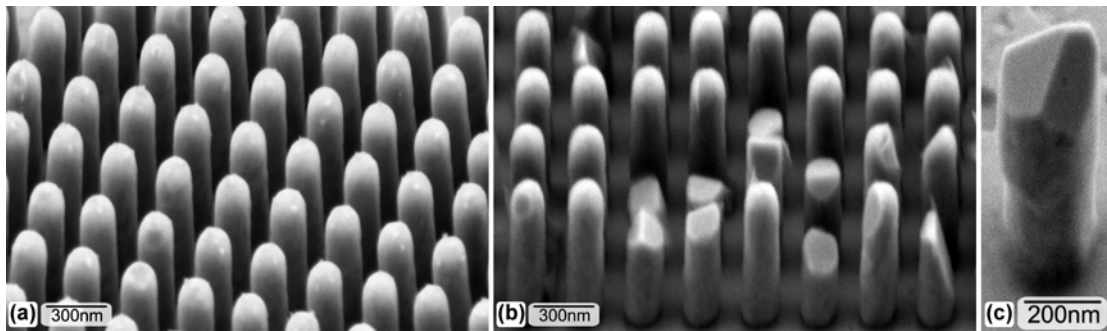


Fig. 3.12. (a)-(b) 170 nm silver pillar arrays obtained by nanoimprinting. In (a), forming was performed at 400°C, achieving complete filling in all structures; in (b), the forming temperature was 500°C and only a fraction of the pillars in the array showed complete filling. All the isolated pillars (not in a closely-packed array) in this sample (such as those shown in Fig. 5.1) were instead completely filled. Both silver plates were initially single crystalline and (100)-oriented, and apart from the temperature all imprinting parameters were similar (but sample (a) was pressed slightly longer). (c) In gold even isolated pillars sometimes showed crystalline faces.

The conditions influencing this material behavior were not investigated in detail in this project, because imprinting parameters making possible good filling had already been found for the structures of interest without the need for systematic, time-consuming experiments. The amount of data available is therefore insufficient to draw definitive conclusions concerning the exact reasons for this phenomenon, which is believed to originate in orientation-dependent formability. The differences for the various orientations are relatively small for *fcc* metals (such as silver and gold); molecular dynamics simulations of copper imprinting showed that (111) plates need about 30% more pressure than (100) plates, but the influence of the orientation depends also on the mold geometry [25]. Incomplete filling would therefore appear only when the imprinting conditions are just good enough for complete deformation of the favorably-oriented grains. Consequently, to avoid this issue one needs enough pressure, temperature and compression time for even the least favorable orientation to have enough formability to fill the desired cavities.

Further clarification would probably result from measuring the grain orientation in those pillars showing incomplete filling (however, such a measurement is difficult to perform via EBSD, because of the nearly absent horizontal top surface and the shading effects of other pillars). Some considerations based on experimental observations may nevertheless be made: (i) Incomplete filling was observed only in high-aspect-ratio pillars with diameters below 500 nm, which are geometrically very

unfavorable structures requiring excellent formability to be filled. (ii) While a minimum imprinting temperature is necessary for good formability, further increased temperature is not necessarily helpful to reduce the phenomenon of incomplete filling, instead seems to accentuate it (compare Figs. 3.12a and 3.12b). (iii) Longer compression times improve filling. (iv) Densely-packed cavities are more difficult to fill than isolated ones of the same size and shape. (v) The initial plate orientation does not play an important role, although (321)-plates appear slightly better than (100)-plates. (vi) Gold seems more subject to incomplete filling than silver, but the two metals were never compared with identical forming parameters.

3.7.3. Texture in imprinted structures

EBSD measurements of the crystallographic orientation at the upper surfaces of structure arrays showed clear preferential orientations, always associated with significant scattering. A (non-uniform) texture was always observed, independently of the single- or polycrystalline nature of the metallic plate before imprinting. This observation is not surprising, because polycrystalline plates recrystallize into large grains (mainly twins) during the preheating time preceding imprinting, such that in both cases one or very few large grains are in contact with all mold patterns (Fig. 3.13). Two samples with the same design, consisting of arrays of lines and pillars with various dimensions, were investigated extensively via EBSD. While these measurements are still statistically insufficient for drawing conclusions, they showed interesting results which are worth mentioning, and may be an incentive for further investigations to improve our knowledge on microforming mechanisms at high temperature. Before imprinting, the first sample consisted of a (100)-oriented silver single crystalline plate, while the second was a (321) single crystal. The results, illustrated in Fig. 3.14, showed completely different preferential orientations in the microstructures, indicating that the original plate orientation strongly influences the lattice orientation of the metal formed into the structures. An attempt to correlate the original orientations with the final textures was made, although we could not identify the exact reason why these textures appeared. The texture in the pillars could also not be directly correlated to the final grain orientation in the base material surrounding them.

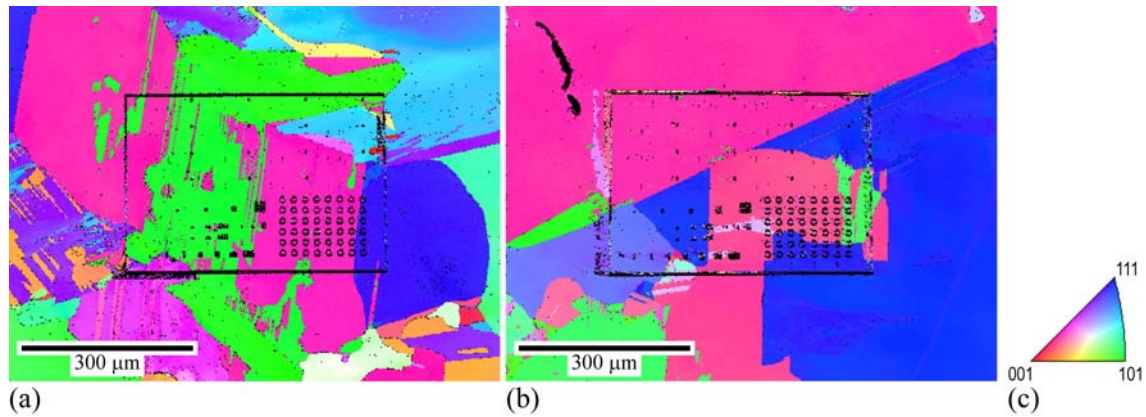


Fig. 3.13. Crystal orientation map of two initially single-crystalline silver samples after imprinting at 400°C. (a) Sample originally (100)-oriented. (b) Sample originally (321)-oriented. In both (a) and (b) the colors represent the grain orientation relative to the normal direction according to the color key shown in the standard stereographic triangle of (c).

The sample starting with a (100)-orientation, with 8 equivalent $\{111\}\langle 110\rangle$ slip systems, showed after forming a spectrum of lattice orientations which can be achieved via gradual grain rotation around a $\langle 110\rangle$ axis. Where there were line-shaped cavities, the grains rotated mostly around the axis that was parallel to the lines (Fig. 3.14a). In other words, the $\langle 110\rangle$ axis parallel to the lines remains fixed, while there are no constraints in other directions and the grain orientations are therefore about randomly distributed around this axis. Where the cavities consisted of cylindrical holes, the rotation took place along either one of the two $\langle 110\rangle$ axes in the surface plane (Fig. 3.14b).

The sample starting with an orientation close to (321) (with one $\{111\}\langle 110\rangle$ slip system particularly favorable compared to all others), instead showed a well-defined single component preferential orientation for every array, independent of the structure shape (lines or pillars). The resulting texture had an apparent relationship to the original plate orientation: during forming most material rotated around the normal direction (compression direction) by an angle which was constant among the structures of a single array but which varied among the different arrays ($\sim 5^\circ$ for all line structures, 9° or 109° for the pillar arrays). In addition, the grains rotated slightly around an in-plane axis, such that their orientation moved closer to a (110) orientation (i.e. the slip direction tends to align to the pillar axis).

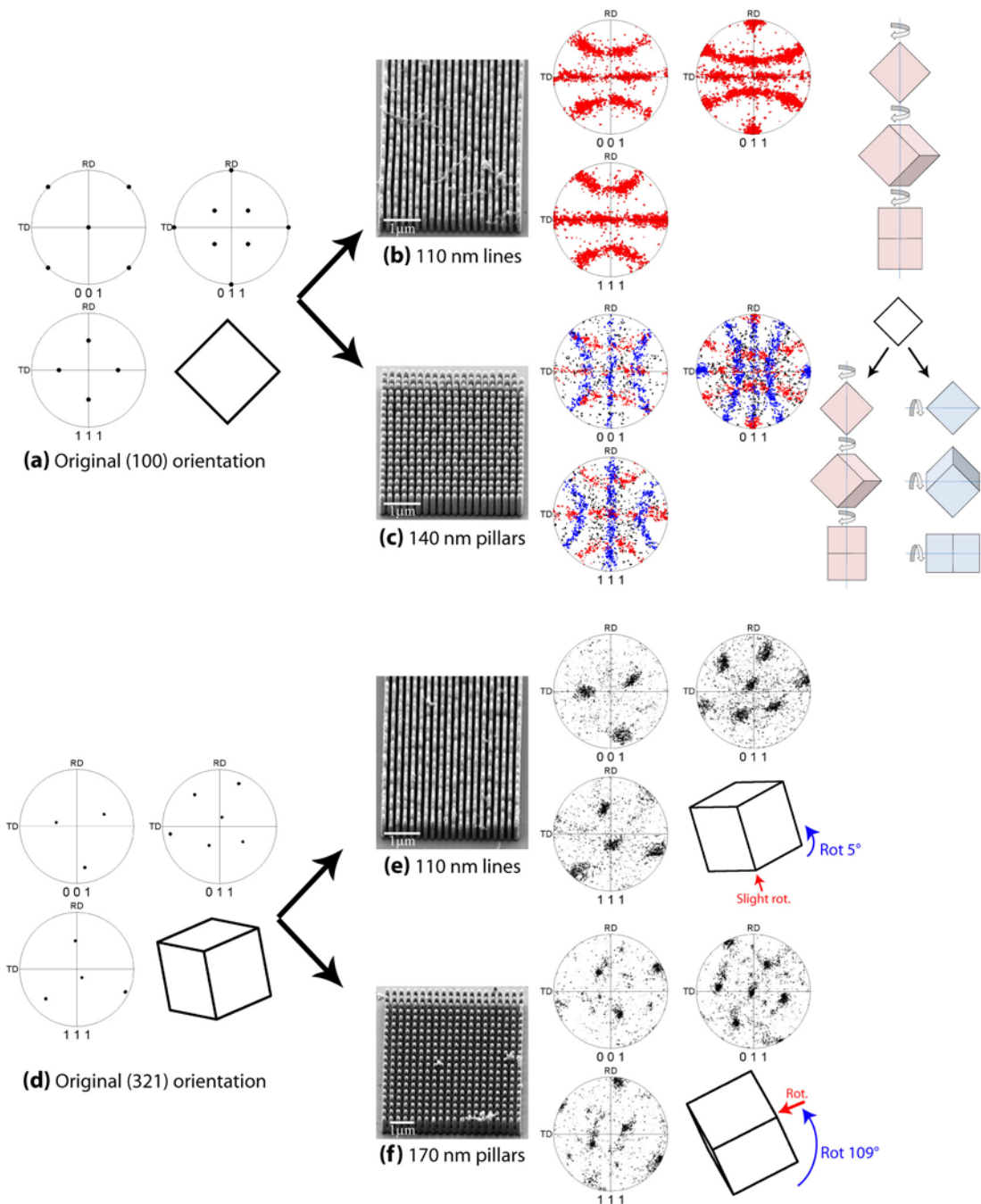


Fig. 3.14. Pillar and line arrays after imprinting and mold removal, with pole figure of the structure top surface orientations and sketch of the lattice orientations. (a) Original (100) plate orientation for (b) and (c). (b) 110 nm lines showing a gradual lattice rotation around the line axis parallel to a $\langle 110 \rangle$ direction (approaching a rotationally symmetric fiber texture). (c) 140 nm pillars showing a near-random rotation around one of the two in-plane $\langle 110 \rangle$ axes. (d) Original (321) plate orientation for (e) and (f) (the plate may, however, have been inserted in the imprinting machine rotated by an angle of 90° , 180° or 270° , or upside down; but all investigated arrays were on the same plate). (e) 110 nm lines showing a strong texture, with the orientation nearly unchanged from the original one (assuming that the plate was in fact inserted with this orientation). (d) 175 nm pillars showing a strong texture, with the original orientation rotated 109° around the normal [321]-axis (blue arrow) and slightly rotated towards (110) (red arrow).

In both samples similar textures were observed in structure arrays with different structure sizes. The textures were generally stronger for the smaller structures, which also possessed higher aspect ratio, and where twinning was less frequent. An analogous gold sample, prepared using a polycrystalline plate consisting initially of large grains of unknown orientation, showed a texture very similar to the (321) silver plate.

3.8. Summary and review of best fabrication parameters

High-quality, large-area silver and gold patterning can be achieved by nanoimprinting producing also micro- and submicrometer structures with very high aspect ratio. Silicon is a suitable mold material, but other dielectrics of comparable mechanical and chemical stability such as SiN_x and SiO_2 also work. A clean initial metallic plate surface is decisive for obtaining high-quality structures; if the plates are polished to achieve good parallelism, the contaminated surface layer must be removed. Elevated forming temperature is necessary to achieve sufficient formability and usually corresponds to 400°C for silver and 300°C for gold. In this study a maximum pressure of 300 MPa was generally used, but depending on structure size and aspect ratio, as well as compression time, lower pressure can also be sufficient (see Figs. 3.9 and 4.3). Especially in the case of thin cylindrical holes in the mold with diameters below $0.5\ \mu\text{m}$, a correct choice of forming parameters is crucial to achieve complete filling in all structures. Mold removal by chemical etching requires particular care for submicrometer structures, which can be easily torn away from the base plate. The risk of sample damage can be minimized by insulating the sample edges from the etching solution and releasing first the structures lying in the central part of the mold. As an alternative to the release of the metal microstructures, a procedure for removing the excess metal on the wafer was developed which enables the production of high-aspect-ratio metallic structures embedded in the dielectric. This is, for example, interesting for optical applications (see the next chapter). The grain orientation in the embossed structures shows a clear texture, whose direction is partially correlated to the original plate orientation.

3.9. References

- [1] M. Madou, Fundamentals of Microfabrication, 2nd edition, CRC, Boca Raton, USA, 2002.
- [2] J. Rabier, J. L. Demenet, Phys. Stat. Sol. B 222 (2000) 63-74.
- [3] G. T. Reed, Nature 427 (2004) 595-596.
- [4] R. W. Olesinski, G. J. Abbaschian, ASM International Binary Phase Diagrams (1996).
- [5] K. R. Williams, K. Gupta, M. Wasilik, J. Microelectromech. Syst. 12 (2003) 6 761-778.
- [6] J. H. Weaver, H. P. R. Frederikse, in CRC Handbook of Chemistry and Physics 87th Ed. (2006) 12 116-140.
- [7] W. L. Johnson, MRS Bull. 24 (1999) 42-56.
- [8] J. F. Löffler, Intermetallics 11 (2003) 529-540.
- [9] T. Zhang, A. Inoue, T. Masumoto, Mater. Trans. JIM 32 (1991) 1005-1010.
- [10] Y. Saotome, K. Itoh, T. Zhang, A. Inoue, Scripta Mater. 44 (2001) 1541-1545.
- [11] J. Schroers, JOM 57 (2005) 35-39.
- [12] G. Kumar, H. X. Tang, and J. Schroers, Nature 457 (2009) 868-872.
- [13] E. Hauser, R. J. Zirke, J. Tauc, J. J. Hauser, S. R. Nagel, Phys. Rev. B 19 (1979) 6331-6336.
- [14] A. Schlegel, P. Wachter, K. P. Ackermann, M. Liard, H. -J. Güntherodt, Solid State Comm. 31 (1979) 373-376.
- [15] E. Huber, M. von Allmen, Phys. Rev. B 28 (1983) 6 2979-2984.
- [16] S. Buzzi, K. Jin, P. J. Uggowitzer, S. Tosatti, I. Gerber, J. F. Löffler, Intermetallics 14 (2006) 729-734.
- [17] U. Engel, E. Egerer, Key Eng. Mat. 223-236 (2003) 449-456.
- [18] E. Egerer, Dissertation Univ. Erlangen-Nürnberg, Meisenbach Verlag (2005).
- [19] C. W. Hsieh, H. Y. Hsiung, Y. T. Lu, C. K. Sung, W. H. Wang, J. Phys. D – Appl. Phys. 40 (2007) 3440-3447.
- [20] G. F. Vander Voort, W. Van Geertruyden, Specimen preparation for Electron Backscattered Diffraction, Bühler sample preparation notes.

- [21] M. Hauder, J. Gstöttner, L. Gao, D. Schmitt-Landsiedel, *Microelectr. Eng.* 64 (2002) 73-79.
- [22] S. W. Pang, T. Tamamura, M. Nakao, A. Ozawa, H. Masuda, *J. Vac. Sci. Technol. B* 16 (1998) 1145-1149.
- [23] Y. Hirai, T. Ushiro, T. Kanakugi, T. Matsuura, *Proc. SPIE* 5220 (2003) 74-81.
- [24] J. Jiang, F. Mei, W. J. Meng, G. B. Sinclair, S. Park, *Microsyst Technol* 14 (2008) 815-819.
- [25] Q. X. Pei, C. Lu, Z. S. Liu, K. Y. Lam, *J. Phys. D – Appl. Phys.* 40 (2007) 4928-4935.

4. Optical properties: Suitability of direct nanoimprinting for producing metal-containing optical devices¹

It was shown in the previous chapter that nanoimprinting enables filling with pure metals of high-aspect-ratio holes in silicon and other dielectrics on a parallel way. By arranging regular metallic structures periodically in a dielectric over large areas, one obtains so-called “metal-containing photonic crystals”, i.e. metallo-dielectric composites with specific optical properties originating from local and collective plasmonic resonances due to the periodicity in dielectric constant. The optical response of such composites is very sensitive to the fabrication parameters, requiring maximum uniformity over large areas.

The suitability of nanoimprinting for preparing such structures is demonstrated in this chapter by the successful fabrication of dense arrays of silver pillars with diameters down to 140 nm and with aspect ratios up to 13, which show excellent regularity over very large areas. Si–Ag photonic crystals were also produced by imprinting and subsequent removal of the excess metal. Their reflectance, measured in the near-infrared as a function of light polarization and incident angle, showed strong collective resonances, confirming the sample quality and uniformity.

¹S. Buzzi, M. Galli, M. Agio, J. F. Löffler, “Silver high-aspect-ratio micro- and nanoimprinting for optical applications”, Appl. Phys. Lett. 94 (2009), in press.

4.1. Introduction

The interest in composite materials which show a periodic variation of the dielectric constant (photonic crystals) originates in their ability to control light propagation [1-2]. The diffraction-based phenomenon hinders the propagation in defined directions of photons with certain wavelengths and polarizations. Such materials also exist in nature and are, for example, responsible for the iridescence of butterfly wings or opal crystals [3]. By using materials with strong dielectric contrast (such as silicon-air, $\epsilon_{\text{Si}}:\epsilon_{\text{air}} = 12:1$) arranged in specific periodic lattices, it is even possible to hinder the propagation in every direction of the totality of the photons, whose energy lies in a range of “forbidden” values called “photonic bandgap”. The effect of photonic crystals on photons is analogous to the effect of semiconductors on electrons, where the bandgap is caused by the periodic potential due to the atomic lattice. In addition, if in semiconductors the electronic properties can be significantly changed by doping (i.e. introducing foreign atoms with a different number of valence electrons, which cause a local perturbation in the periodicity), the corresponding effect can also be achieved on photons by locally altering the periodicity in the photonic crystal. This possibility considerably extends the range of potential optical applications. For example, point defects in a photonic crystal with bandgap can localize light and be exploited to produce cavities, enabling the control of spontaneous emission; such structures are e.g. attractive for light-emitting diodes or lasers. Line defects can, instead, be used to guide light from a location to another, with the significant advantage over standard waveguides (relying on total reflection) of also making sharp bends possible without significant losses, enabling the miniaturization of optical devices and possible combination with electronic devices [4].

Introducing a metal component into the photonic system leads to enhanced or even new phenomena. Metals are in fact characterized by a negative real part of the dielectric constant (see Fig. 3.2), which contrasts with the positive values of the associated dielectric material. The resulting strong interaction of the electromagnetic radiation with groups of conduction electrons near the metal surface (“surface plasmon polaritons”) concentrates the electromagnetic field around the metal surface. This effect has attracted significant interest in sensor technology: exploiting the signal

enhancement in the order of 10^6 around metallic nanoparticles, even single molecules lying close to the metallic particles can be detected by Surface Enhanced Raman Spectroscopy (SERS) [5]. By arranging the metallic structures periodically, the resonances can be further amplified by coupling effects. Moreover, if the structure dimensions are considerably smaller than the radiation wavelength ($\sim \lambda/10$), the incident light experiences an approximately homogeneous refractive index which, for specific designs, can even be negative. The existence of this phenomenon was studied theoretically in 1968 by Veselago [6], but it has become a hot topic only in the last decade, following the proposal of a concrete device design and the experimental verification by Pendry and Smith [7-8]. The properties of such “metamaterials” may lead to ground-breaking applications such as perfect lenses (“superlenses”) [9] or invisibility [10].

An important limitation of metal-containing optical devices is their light absorption (except for very long wavelengths, as in the case of microwaves), due to the non-zero imaginary component of the dielectric constant. In order to keep losses to acceptable values, low-absorption metals should be used; these include essentially pure silver and gold, and secondary aluminum and copper [11-12]. The second obstacle to the wide use of such devices concerns fabrication difficulties, caused by the small (subwavelength) structure sizes and the high uniformity required. These issues may be overcome by direct imprinting: in the previous chapter it was shown that this micro- and nanostructuring process combines high precision and high throughput, and that it works optimally with the low-loss metals silver and gold. It was also shown (section 3.6) that the imprinting technique can be exploited to combine these metals with optically-suitable dielectric materials such as silicon, silicon oxide or silicon nitride, by leaving the metal in the mold cavities after imprinting. In this chapter we focus on the production of large-area, closely-packed arrays of silver pillars with high-aspect ratio, which are particularly challenging to produce. After investigating the process potentialities, test samples of Si–Ag photonic crystals prepared by direct nanoimprinting are optically characterized and their response is discussed with the support of numerical simulations.

4.2. Experimental procedure

Silicon wafers were microstructured by electron beam (e-beam) lithography and reactive ion etching (RIE) (see section 3.1). A macroporous silicon mold with a dense array of 1 μm holes with aspect ratio 100 was also tested. This sample was produced by Lili Zhao at the Max-Planck-Institute for Microstructure Physics in Halle, Germany [13-14] using lithographic patterning and photo-electrochemical etching. The imprinting of the silver plates, with a thickness of 0.2 or 0.5 mm, was performed at a temperature of 400°C and a mechanical pressure of 200 or 300 MPa, as described in detail in the previous chapter. At this point two alternative approaches were applied, depending on the goal. On the one hand, to observe the quality of the imprinted structures the silicon mold was chemically removed (see section 3.5). On the other, to obtain an array of silver rods embedded in the silicon wafer, which constituted the prototypes of Si–Ag photonic crystals to be optically investigated, the remaining excess silver on the silicon surface was eliminated in two steps: an initial rough mechanical removal step using polishing paper and scraping with aluminum, followed by a fine chemical mechanical polishing (CMP) step with a colloidal silica suspension (see section 3.6).

The silver–silicon photonic crystals produced were optically characterized by M. Galli at the University of Pavia (Italy) by measuring the angle- and polarization-resolved specular reflectance in the spectral range 0.4-2 eV with a Fourier-transform spectrometer (Bruker IFS66, Bruker Optics, USA), at a spectral resolution of 1 meV. Measurements were performed for both transverse-electric (TE) and transverse-magnetic (TM) polarizations, and the angle of incidence was varied in the range 5-60° with an angular resolution of 1° (see sketch in Fig. 4.4a, discussed later). A liquid-nitrogen-cooled InSb photodiode was used as the detector and a calcite Glan-Taylor prism as the polarizer.

4.3. Results and discussion

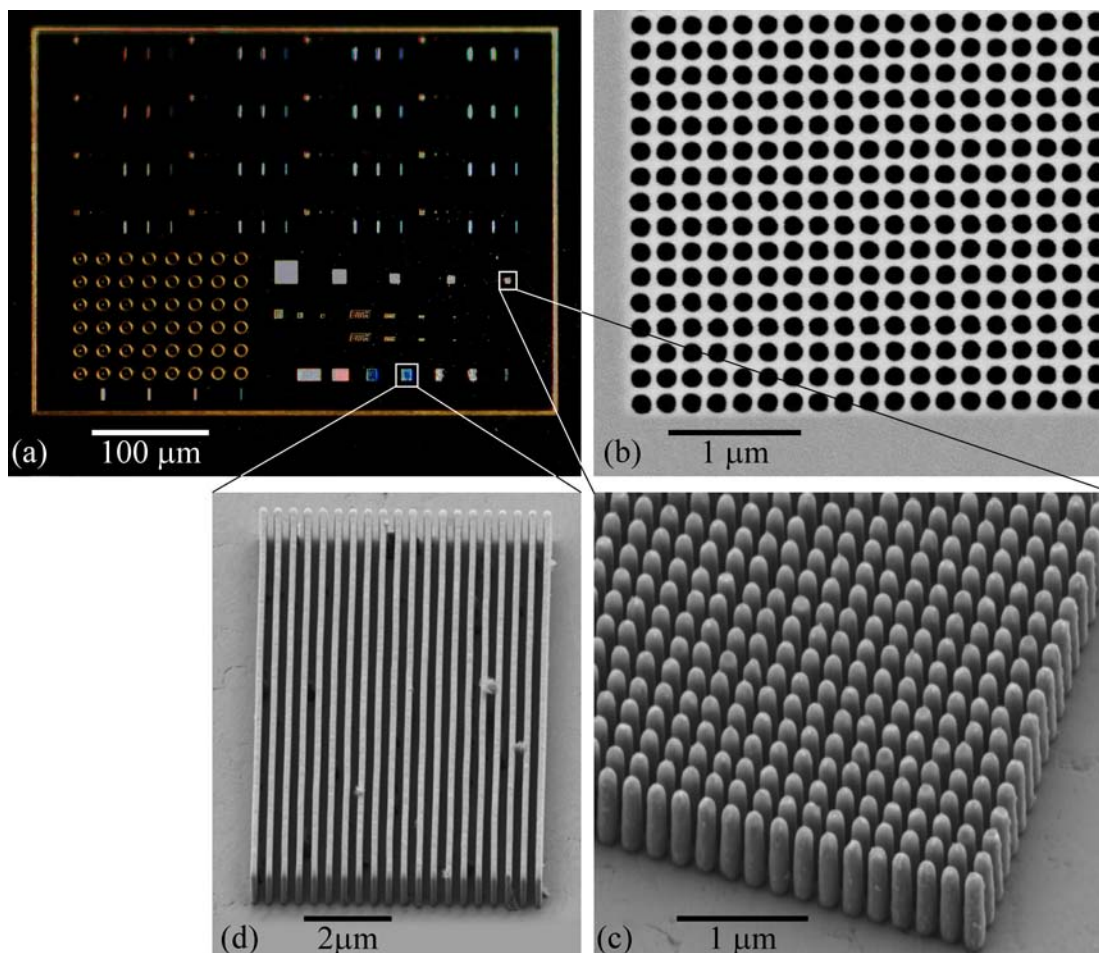


Fig. 4.1. (a) Dark-field optical microscope image showing the pattern overview on a silver sample with arrays of pillars, lines and other structures of various shapes and dimensions, after silicon mold removal. (b) Detail (SEM image) of the silicon mold used to produce the sample (a), showing an array of 140 nm holes. (c) SEM close-up image of (a) showing the array of silver pillars with diameter 140 nm, period 200 nm and height 460 nm standing on the silver plate, corresponding to the mold detail of (b). (d) SEM close-up image of (a) showing an array of silver lines with width 170 nm, period 400 nm and height 630 nm.

A confirmation of the nanoimprinting potential, already demonstrated by other samples in Chapter 3, is given by the sample illustrated in Fig. 4.1, which represents an imprinted silver plate after removal of the silicon mold. Particularly interesting for optical applications are dense arrays of pillars and lines such as those shown in the close-up pictures of Figs. 4.1c and 4.1d, which demonstrate the quality and uniformity of the structures that can be obtained. Similar pillar arrays could, for example, find applications in field-emission displays [15]. For this goal a pillar design with sloped walls (cone-shaped rods) would be ideal, and would also be more

favorable for a potential recycle of the mold, reducing the costs for large-scale production. Instead, arrays of parallel metallic lines such as those of Fig. 4.1 d may be exploited in polarization filters [16]. The demonstrated ability to fill various shapes by imprinting also makes possible the production of chiral metallic structures; this is particularly interesting for the possibility of controlling the light polarization, and it has even been proposed recently as an unconventional way to achieve negative refraction [17-18]. In this study we concentrate on high-aspect-ratio pillars with vertical walls, which are the most difficult to fabricate; the obtained results can then be easily extended to other structure designs. The pillar height in the array of Fig. 4.1 c was limited to 460 nm exclusively by the hole depth in the silicon (Fig. 4.1 b); the silver fills all holes completely. Despite the fact that the metal remains in the solid state during the whole process, it even fills structures slightly larger than the hole aperture (due to the undercut in silicon etching during mold preparation): the resulting pillars are in fact thinner at the bottom than in the central region. This observation confirms what was already observed for lines in the discussion of Fig. 3.9b: as long as the metal is embedded in the silicon there is no gap between the two materials, even in cases of imperfect hole shape. This is an important consideration simplifying the simulation of the optical properties of such composites, which are strongly influenced by the Si – Ag interface (see Fig. 4.5, discussed later).

EBSD measurements over large arrays of silver pillars indicate that most pillars with a diameter below 0.5 μm are single-crystalline, and only a minority consists of two or three twins (see section 5.3.1). The general absence of grain boundaries, at least in small pillars, is a promising indication of minimized optical losses in these dense and pure silver pillars. Moreover, EBSD scans showed sharp patterns, even when performed several months after sample fabrication, indicating that if an oxide layer develops on the silver surface it is not thicker than a very few nanometers. Again, this is a positive indication for stable, good optical properties of silver devices even where the metal is exposed to the atmosphere.

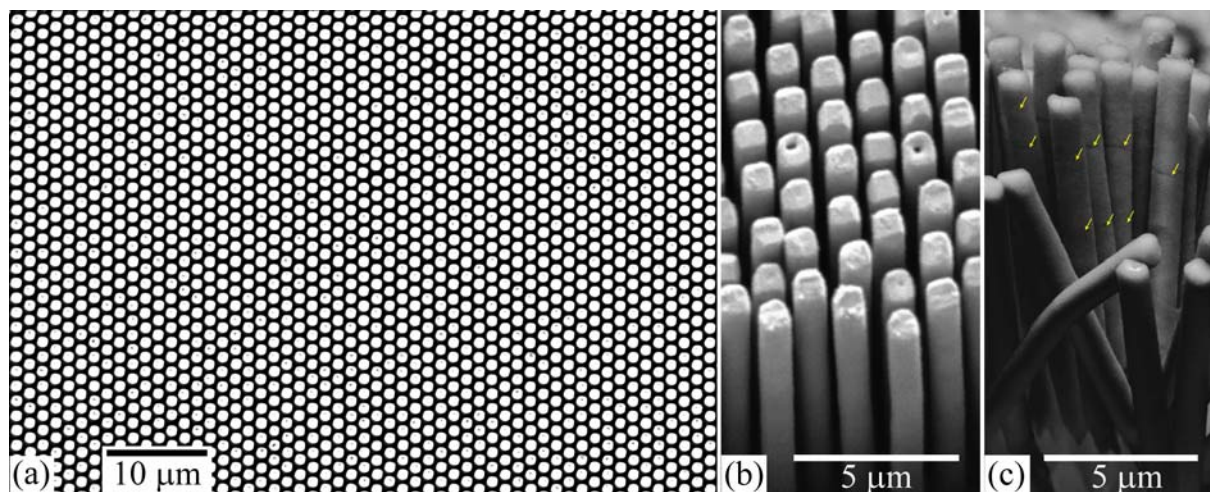


Fig. 4.2. (a) SEM image (top view) illustrating the structure regularity of a large-area array of hexagonally packed $1\ \mu\text{m}$ silver pillars with a period of $1.5\ \mu\text{m}$ and an aspect ratio of 13, standing on a silver plate after releasing from the silicon mold. (b) Tilted view (50° , with tilt correction) of a defect region where the front pillars have been bent, enabling the observation of the high aspect ratio and uniform height of the silver structures (the pillars of this region are, however, not perfectly vertical). (c) Tilted view (70° , not tilt-corrected) of torn-off pillars, where grain boundaries are indicated by arrows.

The fabrication of a homogeneous, large-area array of silver pillars with a very high aspect ratio of 13 is shown in Fig. 4.2. Since the $1\ \mu\text{m}$ holes covering the whole surface of the $5 \times 5\ \text{mm}^2$ macroporous silicon mold were extremely deep ($100\ \mu\text{m}$), the uniform ($13\ \mu\text{m} \pm 5\%$) pillar height (and therefore the aspect ratio) visible in Fig. 4.2b was limited in this sample by the silver formability and the imprinting parameters. With longer compression periods or more elevated pressures even higher aspect ratios may be achieved. As was already the case for the dense hole array of Fig. 4.1c, the silicon survived undamaged the compression during the imprinting process, despite its brittleness and great porosity. Due to the wide availability of facilities for microstructuring this semiconductor, silicon is therefore the first choice as a mold material for small-scale production of high-value metallic micro-components or for production of infrared devices.

The excellent regularity over a large area illustrated in Fig. 4.2a shows that pillars of very high aspect ratio can also be successfully released from the mold and that they possess enough mechanical stability to maintain their original straight, vertical shape. This observation is not trivial for structures with such a high aspect ratio; in fact, strong capillary forces are generated while drying with a nitrogen flow after the silicon wet-etching, such that unstable pillars would normally be bent and would stick

to each other. No special care such as supercritical point-drying was used. Nevertheless, some regions of the sample were damaged during mold release and are shown in Fig. 4.2b and c; these areas are particularly interesting because they make possible a side view of the pillars. One can thus observe the aspect ratio of the pillars and see that even if they are relatively large they are mainly composed of a few grains with a length of 2-3 μm , i.e. considerably bigger grains compared to those with the same diameter analyzed in Chapter 5, although the only difference between these samples (both initially single-crystalline and (100) oriented) was the mold design with denser pillars and much higher aspect ratio.

The sample shown in Fig. 4.2 demonstrates that nanoimprinting is suitable for producing pillars with such a large aspect ratio (above 10) that they can be optically considered quasi-two-dimensional (infinitely long wires) [19]. This property simplifies simulations and may also generate interesting applications. For example, Wang *et al.* [20] recently predicted the achievement of negative refraction for wavelengths around 50 μm using freestanding pillar pairs nearly identical to those of Fig. 4.2 but made of gold, a metal which can be formed comparably to silver (see Fig. 3.1).

In the two examples presented in Figs. 4.1 and 4.2 the silver plate was released from the mold after imprinting, enabling a rapid evaluation of the obtained filling and aspect ratio. As mentioned earlier, final mold removal is, however, not necessarily desirable: in fact, periodic arrays of metallic (e.g. Ag) pillars in a dielectric (e.g. Si) matrix can also have interesting optical applications, for example for sensing technology, where liquids containing molecules to be investigated are dispersed on the composite and their signal is enhanced by plasmonic resonances of metallic particles located nearby. In addition, by using SOI (Silicon on Insulator) wafers or other composite dielectrics it is possible to confine the light near the top surface of the wafer, where the metallic rods are located, and optically connect the metal array to other photonic components. For these applications, the excess silver is removed from the wafer surface after imprinting. Two examples of metallo-dielectric photonic crystals produced using this method are shown in Fig. 4.3, with silver pillars of diameters of 285 and 180 nm, respectively. The filling was complete and very homogeneous over the entire areas of $500 \times 500 \mu\text{m}^2$, as shown in the overview SEM picture and by the FIB cross-sections (insets of Figs. 4.3b and 4.3c). Here, the

imprinting was performed with a pressure of 200 MPa instead of the standard 300 MPa; the complete filling achieved also at this lower pressure indicates that even milder fabrication conditions could be used for delicate dielectric materials, although the previous examples showed that this care is not necessary for silicon. The samples obtained are similar in size and period to the gold pillar arrays obtained by Zhang *et al.* [21] by confining colloidal gold nanoparticles in hole arrays; this method is described in section 1.2.5. The nanoimprinting technique, however, has the potential to generate better optical properties because of the lower risk of incorporating impurities and porosity due to solvent trapped among the nanoparticles during annealing. Moreover, by imprinting one can achieve complete filling independent of cavity size and period; this peculiarity offers the possibility to locally introduce inhomogeneities in the periodicity (doping) to produce new optical effects. Despite the rough technique applied, complete removal of the excess silver from the silicon surface was achieved without damaging the structures. Nevertheless, as discussed in section 3.6, this process for removing the excess metal only makes sense for small prototype samples, while for processing entire wafers standard CMP procedures are available [22-23], and the initial thickness of the silver layer should be reduced and optimized in such a way that the mold cavities are just to be filled.

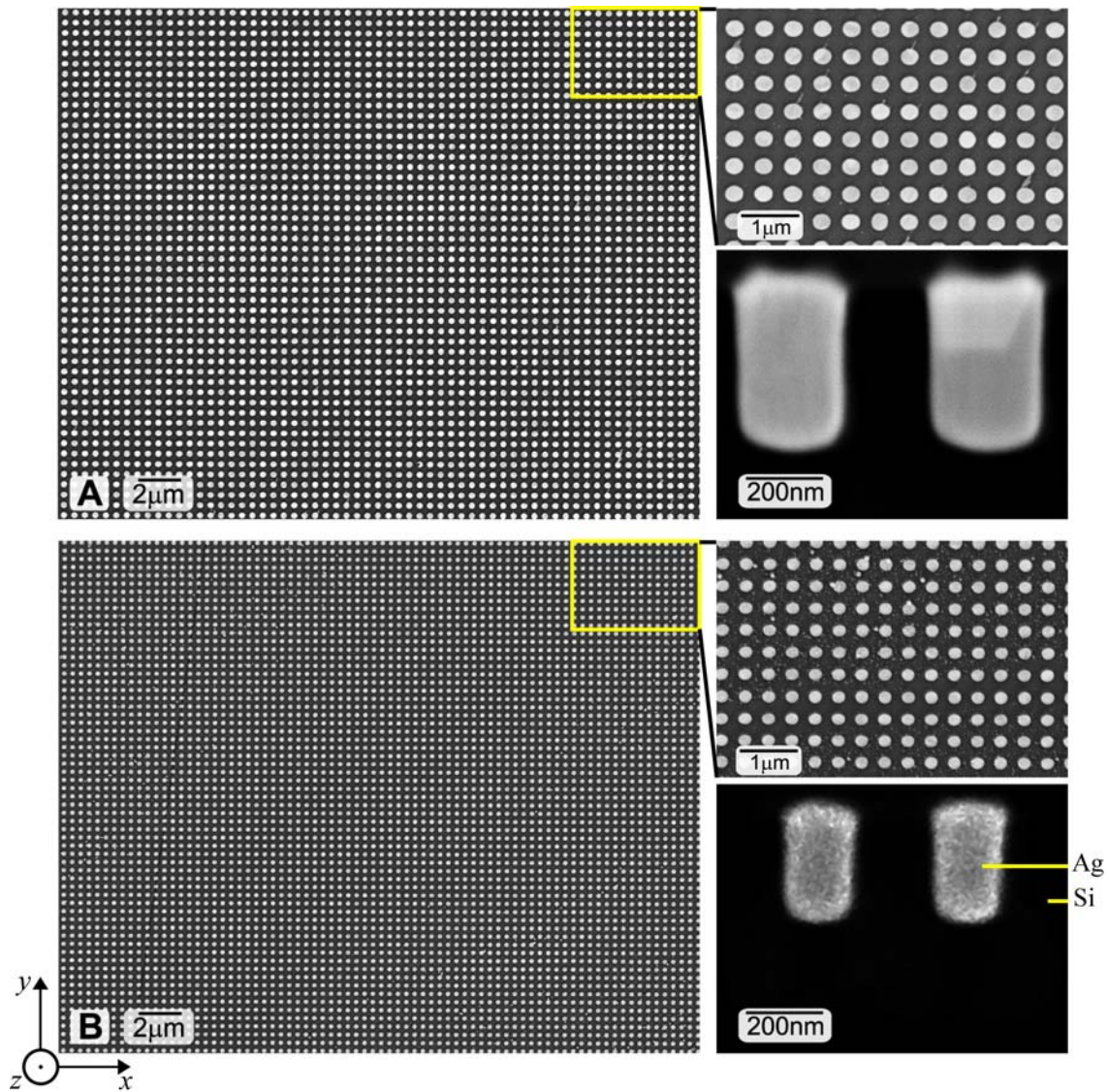


Fig. 4.3. SEM images of silver–silicon photonic crystals with total areas of $500 \times 500 \mu\text{m}$, showing a top overview, an enlarged top view and a FIB cross-section (image with tilt angle 54° and tilt correction 36°) for samples **A** and **B**. Sample **A**: Ag pillars with diameter $d = 285$ nm, period $a = 500$ nm and a depth of 470 nm (aspect ratio 1.65). A grain boundary is visible in the right pillar of the FIB cross-section. Sample **B**: Ag pillars with $d = 180$ nm, $a = 400$ nm and a depth of 325 nm (aspect ratio 1.8).

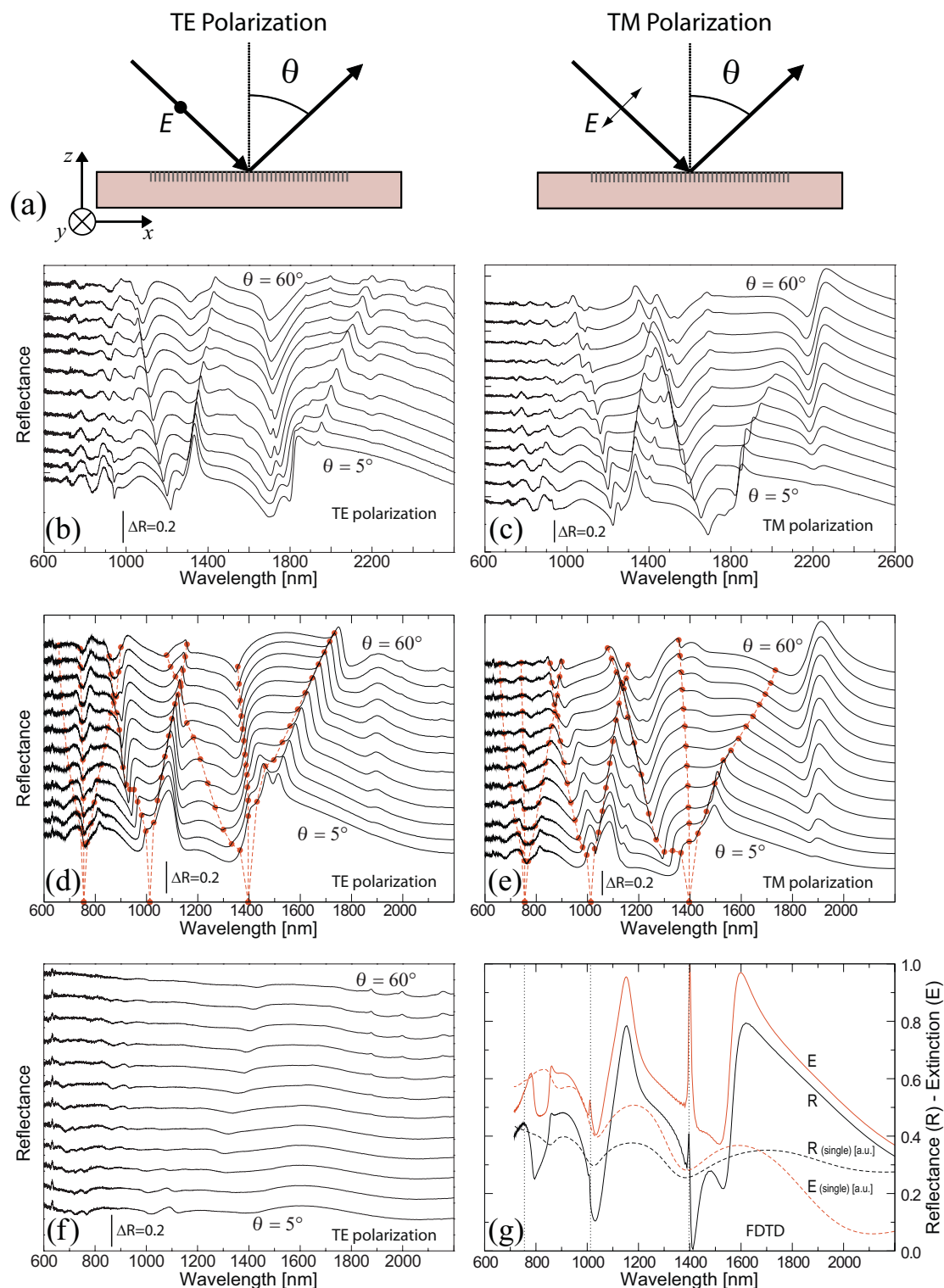


Fig. 4.4. (a) Sketch of the optical reflectance measurements. (b)-(c) Variable-angle reflectance spectra of the Si–Ag photonic crystal **A** of Fig. 4.3 for light with TE (perpendicular to incidence plane) and TM (parallel to incidence plane) polarization, measured along the Γ -X orientation (incidence plane normal to y -direction, see also Fig. 4.3), with the incident angle θ varying from 5° to 60° in steps of 5° . Spectra are shifted vertically for clarity; the ΔR bar gives a scale for the reflectance. (d)-(e) Reflectance spectra of the Si–Ag photonic crystal **B**, with the simulated position of the collective resonances marked by red full circles. (f) Optical reflectance spectra of the Si photonic crystal **B** without silver

filling (empty holes in silicon) measured analogously to (d), not showing significant resonances. (g) FDTD simulation of the normal ($\theta = 0^\circ$) reflectance (R) and extinction (E) for a single Ag nanorod (dashed line) and a regular array of nanorods (solid line) embedded in Si, taking into account a 2.5-nm-thick native oxide (SiO_2) layer between Ag and Si, with the parameters of Sample **B**.

The optical response in the infrared region of the Si–Ag photonic crystals of Fig. 4.3 is shown in Fig. 4.4. The angle-resolved reflectance spectra are characterized for both transverse-electric (TE) and transverse-magnetic (TM) polarizations by the presence of sharp and asymmetric resonances, which show a clear dispersion in energy as a function of the incidence angle (i.e. as a function of the in-plane wavevector of incident light). The resonances are analogous in both samples, but in the array of **B** the resonances are shifted towards higher frequencies due to the smaller pillars and period (note the different scale on the horizontal axis).

This peculiar optical response is indeed very similar to that observed in all-dielectric slab photonic crystals [24-25], where the sharp resonances in reflectance spectra are directly related to the excitation of quasi-guided photonic modes in the periodic structure. The strong resonant features observed in our array of metal nanoparticles are related to both the excitation of localized surface plasmon-polariton resonances (LSPRs) of the individual Ag nanorods, and collective surface plasmon-polariton resonances (CSPRs) supported by the nanoparticle array (coupling among the periodic nanorods) [26-27]. In an attempt to identify the nature of the various observed resonances, Finite-Difference Time-Domain (FDTD) simulations were performed by M. Agio (Nanooptics Group of ETHZ, involved in the INIT collaboration project). The wavelength of the CSPRs observed is set by the Rayleigh cut-off for diffraction into the substrate

$$\lambda = a \frac{n^2 - \sin^2 \theta}{i \sin \theta + \sqrt{i^2 \sin^2 \theta + (i^2 + j^2)(n^2 - \sin^2 \theta)}}, \quad (4.1)$$

where n is the index of refraction of the Si substrate, θ is the angle of incidence, and a is the array period. The integers i and j refer to the diffraction order along the x and y axes.

The full circles in Figs. 4.4d and 4.4e label the position of the CSPRs for the Sample **B** as given by Eq. (4.1) for the first diffraction orders $(i, j) = (0, \pm 1), (\pm 1, 0)$,

$(\pm 1, \pm 1)$, $(0, \pm 2)$, $(\pm 2, 0)$. Their vertical position corresponds to the value of the measured reflectance at the wavelength of the CSPR. The full circles on the horizontal axis refer to the case $\theta = 0^\circ$. Note that the position and dispersion of the experimental curves agrees well with the values of Eq. (4.1) only if the dispersion of Si is taken into account (for photon energies below its bandgap of 1.1 eV, silicon also possess an imaginary component of the dielectric constant corresponding to absorption) [12]. The linewidth, lineshape and strength of the CSPRs depend on several parameters and need further investigation to be correctly simulated. Contrary to previous work [26-27], which used Au-nanoparticle arrays on low-index substrates such as glass and indium tin oxide (ITO), the current samples made of Ag nanorods in a high-index material enable the mapping of several CSPRs due to different diffraction orders in the near-infrared spectral range. The reflectance curves also contain information on the LSPRs. Because their spectral position overlaps with the diffraction-related CSPRs it is difficult to isolate them, also because the high-index substrate makes them quite broad except for the isolated LSPR around 1900 nm. The latter corresponds to an excitation along the z -axis of the nanorods when the incident angle increases and the light is TM polarized (Fig. 4.4e). The absence of resonances originating from the periodic dielectric structure was confirmed by equivalent measurements performed on the same samples before silver filling (empty air holes), which showed a nearly flat optical response (Fig. 4.4f).

For a precise description of all resonances, an investigation of several samples with a systematic variation of single parameters would be required, such as the pillar depth (leading to a shift of the excitation along the pillar z -axis but maintaining the transversal x - y excitation nearly unchanged) and the periodicity (which changes the coupling among the nanorods, i.e. the CSPRs, and only marginally the LSPRs due to a variation of the average refractive index in the upper region of the sample containing the metallic pillars). To better understand the role of the other LSPRs, FDTD simulations [28] of arrays and isolated nanorods were performed using normal incident light. Fig. 4.4g compares the extinction and reflection spectra computed using the nominal parameters of Sample **B** (solid curves) with those of a single silver nanorod under the same conditions (dashed curves). Due to the symmetry of the square lattice, both TM and TE modes show the same extinction at normal incident light; in fact, the measured curves at $\theta = 5^\circ$ are similar. The CSPRs (vertical dotted

lines) are clearly not present in the single-nanoparticle spectra. The LSPRs are broad, as expected, and their peak position and linewidth alter [26] when they are coupled with the CSPRs in the array. The experimental TE and TM curves obtained for $\theta = 5^\circ$ should be similar to the FDTD results for normal incidence. While the position of the resonances indeed shows good agreement, the lineshape and linewidth match only approximately. Possible explanations are the difficulty of knowing the exact geometric parameters, size dispersion, and other structural disorder in the sample. In fact, the simulations show a significant influence on the resonances even for small changes in the sample parameters. For example, the presence of just 2-3 nm of silicon oxide (a low-index material, with $\varepsilon = 2.1$) between silicon and silver, which is expected because the silicon mold readily oxidizes when exposed to air, showed a strong effect on the resonances, as shown in Fig. 4.5. Reflectance maxima and minima are drifted to different wavelengths and there are large discrepancies in the peak intensities, particularly evident in the region 1200-1400 nm.

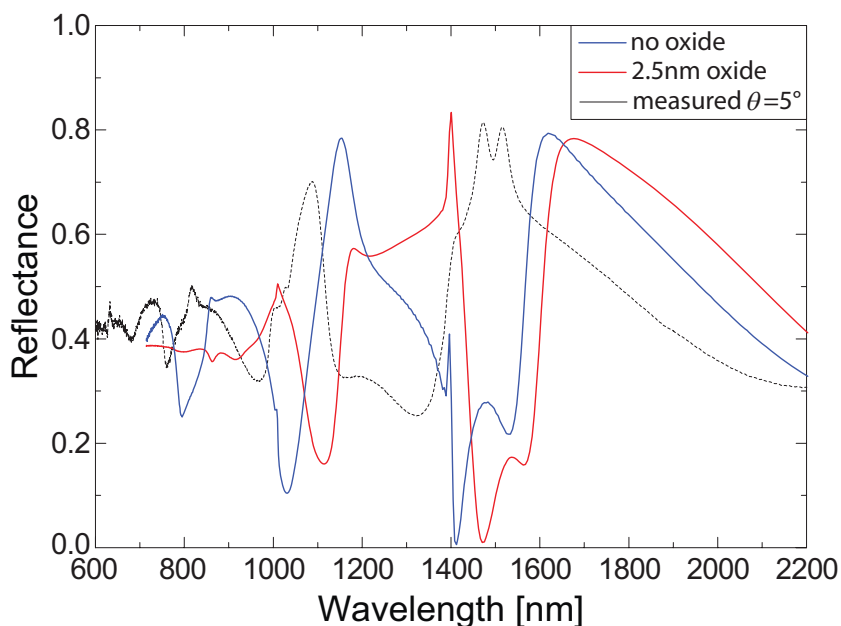


Fig. 4.5. FDTD simulations of the reflection under normal illumination ($\theta = 0^\circ$) for the silver–silicon photonic crystal **B** with either a sharp interface between the two materials (no oxide) or a 2.5-nm-thick SiO_2 layer between silicon and silver, and comparison with measurement at $\theta = 5^\circ$.

4.4. Conclusions

The samples presented in this chapter demonstrated the great potential of direct imprinting for large-scale production of high-quality arrays of silver micro- and nanopillars. The process is especially attractive for the possibility it presents to achieve very high aspect ratios with dense silver (and gold) structures, rendering feasible the fabrication of two-dimensional metallo-dielectric composites which can be simulated with relative ease. It was also shown that silicon is an appropriate mold material and survives the imprinting pressure and excess silver removal even in cases of dense arrays with deep holes. Reflectance measurements of Si–Ag photonic crystals produced by imprinting showed that these exhibit strong CSPRs, confirming the uniformity and high quality of the periodic metallic structures. This is very encouraging for the technique's application in the production of optical devices.

4.5. References

- [1] J. D. Joannopoulos, S. G. Johnson, J. N. Winn, R. D. Meade, *Photonic Crystals, Molding the Flow of Light* (Second edition), Princeton University Press 2008.
- [2] J. D. Joannopoulos, P. R. Villeneuve, S. Fan, *Nature* 386 (1997) 143-149.
- [3] Z. Vértesy, Zs. Bálint, K. Kertész, J. P. Vigneron, V. Lousse, L. P. Biró, *J. Microscopy*, 224 (2006), 108-110.
- [4] J. Smajic, C. Hafner, D. Erni, *Opt. Expr.* 11 (2003) 12 1378-1384.
- [5] J. N. Anker, W. P. Hall, O. Lyandres, N. C. Shah, J. Zhao, R. P. Van Duyne, *Nature Mat.* 7 (2008) 442.
- [6] V. G. Veselago, *Sov. Phys. Usp.* 10 (1968) 509-514.
- [7] J. B. Pendry, A. J. Holden, D. J. Robbins, W. J. Stewart, *IEEE Trans. Microwave Theory Tech.* 47 (1999) 2075-2084.
- [8] D. R. Smith, W. J. Padilla, D. C. Vier, S. C. Nemat-Nasser, S. Schultz, *Phys. Rev. Lett.* 84 (2000), 4184-4187.
- [9] J. B. Pendry, *Phys. Rev. Lett.* 85 (2000) 3966-3969.
- [10] J. B. Pendry, D. Schurig, D. R. Smith, *Science* 312 (2006) 1780-1782.

- [11] J. H. Weaver, H. P. R. Frederikse, in *CRC Handbook of Chemistry and Physics* 87th Ed. (2006) 12 116-140.
- [12] E. D. Palik (ed.) *Handbook of optical constants of solids* (Academic Press, 1997).
- [13] V. Lehmann, *J. Electrochem. Soc.* 140 (1993) 10 2836-2843.
- [14] A. Birner, U. Grüning, S. Ottow, A. Schneider, F. Müller, V. Lehmann, H. Föll, U. Gösele, *Phys. Status Solidi A* 165 (1998) 111-117.
- [15] T. Kim, J. Kim, S. J. Son, S. Seo, *Nanotechnology* 19 (2008) 295302.
- [16] Y. Hirai, T. Ushiro, T. Kanakugi, T. Matsuura, *Proc. SPIE* 5220 (2003) 74-81.
- [17] S. Zhang, Y. -S. Park, J. Li, X. Lu, W. Zhang, X. Zhang, *Phys. Rev. Lett.* 102 (2009) 023901.
- [18] E. Plum, J. Zhou, J. Dong, V. A. Fedotov, T. Koschny, C. M. Soukoulis, N. I. Zheludev, *Phys. Rev. B* 79 (2009) 035407.
- [19] H. van der Lem, A. Moroz, *J. Opt. A: Pure Appl. Opt.* 2 (2000) 395-399.
- [20] F. M. Wang, H. Liu, T. Li, Z. G. Dong, S. N. Zhu, X. Zhang, *Phys. Rev. E* 75 (2007) 016604.
- [21] X. Zhang, B. Sun, H. Guo, N. Tetreault, H. Giessen, R. H. Friend, *Appl. Phys. Lett.* 90 (2007) 133114.
- [22] M. Madou, *Fundamentals of Microfabrication*, 2nd edition, CRC, Boca Raton, USA, 2002.
- [23] M. Hauder, J. Gstöttner, L. Gao, D. Schmitt-Landsiedel, *Microelectr. Eng.* 64 (2002) 73-79.
- [24] V. N. Astratov, D. M. Whittaker, I. S. Culshaw, R. M. Stevenson, M. S. Skolnick, T. F. Krauss, R. M. De La Rue, *Phys. Rev. B* 60 (1999) R16255.
- [25] M. Patrini, M. Galli, F. Marabelli, M. Agio, L. C. Andreani, D. Peyrade, Y. Chen, *IEEE J. Quantum Electron.* 38 (2002) 885-890.
- [26] V. G. Kravets, F. Schedin, A. N. Grigorenko, *Phys. Rev. Lett.* 101 (2008) 087403.
- [27] B. Auguie, W. L. Barnes, *Phys. Rev. Lett.* 101 (2008) 143902.
- [28] The FDTD simulations take into account the material dispersion of silver and silicon through appropriate dispersion models.

5. Mechanical properties: Deformation behavior of silver submicrometer-pillars prepared by nanoimprinting¹

Scaling in material properties is of great importance in microsystems and microelectronics where the device dimensions continuously shrink. Recently, compression tests of micron-sized pillars produced using a focused-ion beam (FIB) have become standard in the investigation of scaling effects. The influence of the fabrication process on the mechanical properties of the samples has, however, not been conclusively resolved. In this study, 130 silver pillars were fabricated using the nanoimprinting technique, which does not pose the issues associated with FIB milling, namely surface amorphization and gallium contamination. Displacement-controlled compression tests on pillars with diameters of 130 - 3000 nm reveal for submicrometer samples an inverse proportionality of flow strength to diameter, which is associated with a wide strength distribution and a deformation taking place in large discrete strain bursts. The largest pillars show instead near bulk-like behavior. Unlike studies on other fcc materials, mechanical twinning is also an important deformation mechanism in Ag due to its very low stacking fault energy. In addition, occasional preexisting twin boundaries constituted preferential planes for localized deformation if favorably sloped. Despite the absence of ion-induced artifacts, scaling laws and absolute values of strength are comparable to those obtained via FIB milling.

¹S. Buzzi, M. Dietiker, K. Kunze, R. Spolenak, J. F. Löffler, “Deformation behavior of silver submicrometer-pillars prepared by nanoimprinting”, Phil. Mag. 89 (2009) 869-884.

5.1. Introduction

When the dimensions of a material are reduced from the macro (bulk) to the micro scale, some of its properties may change, as described in section 1.4. One of these “size effects” which has been extensively investigated over the last few years is the dependence of the strength on sample dimensions, resulting in the general observation of an increase in strength with decreasing size. This effect was observed for thin metallic wires by Taylor [1] as early as 1924, and was widely studied fifty years ago in investigations of the tensile strength of metallic whiskers. Above a critical size, whiskers show an inverse proportionality of the strength to the diameter ($\sigma \sim d^{-1}$), accompanied by larger scattering for small samples, indicating that deformation is controlled by dislocation nucleation or activation of dislocation sources [2-5].

Recently many researchers have focused on the deformation behavior of micropillars subjected to uniaxial compression [6-14]. In addition to the advantage of having a relatively simple setup, this technique makes possible the investigation of material properties without introducing strong strain gradients, often considered to be the source of the size effects observed in other experiments such as nanoindentation or microtorsion [15]. The micropillars are usually produced by milling a metallic film or bulk material with a focused-ion beam (FIB), a technique which enables the fabrication of precise microstructures in a wide range of materials. Besides the disadvantage of employing sequential and therefore slow processing, this fabrication technique is known to damage the sample surface by amorphization, dislocation generation and implantation of gallium ions, although the effective extent of this damage is still being debated [10, 16, 17]. Because the surface plays a crucial role in dislocation behavior at very small dimensions, it is suspected that the size effects observed in these experiments are affected by the preparation method. On the other hand, investigations of pillars not produced by FIB milling are very limited and are not coherent: Greer *et al.* [8] found a very strong size dependence on the part of the strength in electroplated gold pillars with dimensions between 650 nm and 2 μm (see also Fig. 5.7, discussed later). In contrast, Bei *et al.* [11] investigated submicrometer pillars of a molybdenum solid solution produced by directional solidification of a eutectic superalloy and selective etching and observed a constant flow stress

comparable to the theoretical strength, i.e. no size effects. They explained this result with the low probability of pre-existing dislocations in pillars smaller than 1 μm , which are thus defect-free, in analogy to small whiskers.

In this chapter we present an investigation into the mechanical properties of silver micro- and submicrometer pillars produced by direct nanoimprinting. By virtue of the parallel production of large numbers of microparts, this process has great potential for use in the fabrication of metallic microcomponents, as is nowadays the case for macroscopic parts. Application to small components requires a more complete understanding of size effects in the forming process, in order to enable reliable design and fabrication at small scales [18, 19]. With an appropriate choice of the embossing parameters we were nevertheless able to produce micropillars of various dimensions (Chapter 3). The results on embossed micropillars presented here can therefore be used directly in the future to dimension metallic components produced by this industrial process. In this study we focus on silver, a metal very similar to gold but not yet investigated by uniaxial microcompression, which is characterized by a low stacking fault energy of 22 mJ m^{-2} [20].

Compared to FIB-prepared pillars, embossed micropillars have the advantage of possessing non-amorphous surfaces and the potential for better statistics due to the rapid production of large numbers of pillars. On the other hand, grain orientation in the pillars cannot be fully controlled. Grain boundaries are also present and play an important role in deformation behavior for pillar diameters above a few hundreds of nanometers. In this chapter we also characterize in detail the evolution of the crystallographic grain orientations in micropillars subjected to uniaxial compression by high-resolution orientation mapping using electron backscattered diffraction (EBSD), making it possible to differentiate between the two concurrent deformation mechanisms of dislocation slip and mechanical twinning.

5.2. Experimental procedure

5.2.1. Sample preparation

The silver micropillars were produced by embossing of a $5 \times 5 \times 0.5 \text{ mm}^3$ silver plate in a mold consisting of a microstructured silicon wafer (Fig. 3.5, see Chapter 3). The silicon mold was structured by e-beam lithography and reactive ion etching (RIE). The hole depth in the silicon is determined by the combined effect of etching time and structure width, as discussed in section 1.2, resulting in an aspect ratio of up to 3.5 for the smallest pillars. In order to easily locate the pillars in the nanoindentation system, rings or lines were etched around the holes (Fig. 5.1). Shortly before embossing, the silver plates were etched for 60 s in 30% nitric acid to remove any surface contamination.

The embossing process was performed under vacuum at a pressure of 300 MPa at 400-500°C. After mounting of the silver plate, the compression chamber was preheated for 45 min at the embossing temperature to achieve constant conditions. The pressure was increased to 300 MPa, and maintained for 10 min at peak temperature and also during cooling to 80°C. After mold removal, the samples were glued to SEM aluminum sample stubs with a thin layer of silver paste (G3692, Plano GmbH, Germany).

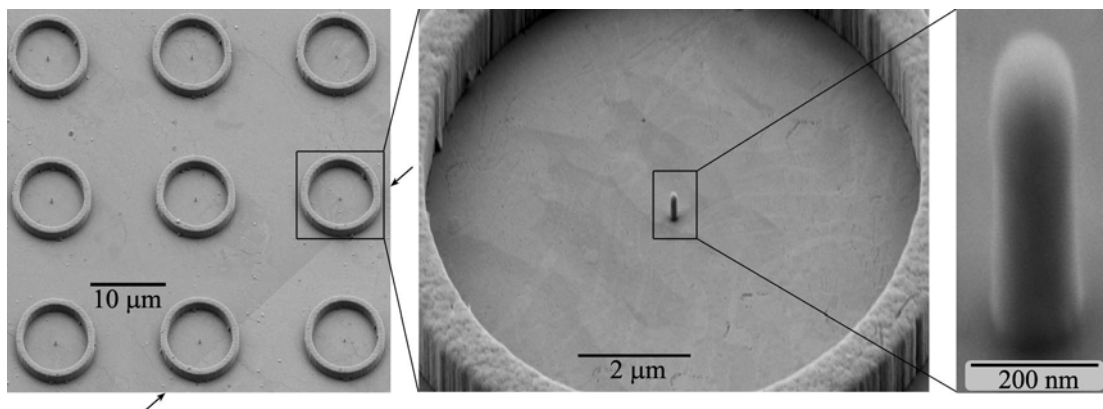


Fig. 5.1. Embossed silver pillars ($d = 130\text{-}170 \text{ nm}$, with zoom on a 130 nm pillar) after mold removal, surrounded by $10 \mu\text{m}$ rings to facilitate their localization in the nanoindentation system (SEM image tilted 50° , with tilt correction). A diagonal twin boundary in the base material is visible in the overview picture (marked by arrows).

Three samples were investigated in this study. Sample A consisted initially of a (100) single crystalline silver plate. This sample was embossed at 500°C in a mold with hole diameters of between 130 and 1050 nm (Fig. 5.1). Sample B consisted of the same material and was embossed at 400°C in a mold with larger and deeper holes (up to 3 μm diameter). Sample C consisted of polycrystalline silver (Ag 99.9985%, Alfa Aesar, USA) and was embossed at 400°C in the mold with large holes (analogous to Sample B). After pillar production, all the samples showed a polycrystalline base plate with randomly-oriented large grains and twins of several tens of micrometers due to recrystallization during embossing (see Fig. 3.13 and Fig. 5.2a, discussed later).

All pillars belonging to the same sample were subjected to identical preparation conditions; except for grain size and orientation they are considered equivalent. Possible differences among the pillars may, however, arise from different starting dislocation densities, resulting from size effects during pillar production.

5.2.2. Compression tests and characterization

Flat punch nanoindentation was performed using a triboindenter (Hysitron Inc., USA) with a 5 μm diamond flat punch. After a drift calibration step, most indentations were performed at a constant loading rate of 10 nm s^{-1} (“displacement control mode”) up to ~20% strain, followed by a holding step of 1s and unloading at a rate of 50 nm s^{-1} . Engineering stress-strain curves were calculated from the raw data (displacement-load) and the highest stress values measured at a strain below 5% were defined as flow strength $\sigma_{0.05}$.

Each pillar of Samples A and B (typically 6 pillars for each investigated size) was characterized before and after indentation by SEM, which was used for both imaging and measuring the dimensions. Further analysis was performed by EBSD on the top surfaces of the pillars, and the scans are presented here as processed orientation maps indicating grain shapes and crystal orientations. Selected pillars were further studied by slicing shallow-angle cross-sections using FIB, where crystal orientation contrast was visualized by SEM SE-images and measured in-situ by EBSD. Details on the characterization techniques are given in Chapter 2.

5.3. Results

5.3.1. Sample preparation

Even when starting with a single-crystalline plate, the base material lost its original orientation during embossing and dynamically recrystallized in large, randomly oriented grains (mainly twins, see Figs. 3.13 and 5.2a). The recrystallization took place only during the embossing process, since an XRD measurement of a plate after the pre-heating step alone (i.e. without pressure) indicates that the plate was still single-crystalline.

Before uniaxial compression, all pillars with diameters above 1 μm were polycrystalline, and the grains often twinned. The grain size showed large scattering, but the number of grains per surface area indicates similar sizes for pillar diameters of between 1 and 3 μm . By contrast, pillars smaller than 0.5 μm were usually single-crystalline or consisted of one dominant grain with a small side twin (Fig. 5.2b). The grain orientation changed during embossing compared to the initial (100) plate orientation represented in Fig. 5.2c. While pillars above 0.5 μm did not show any preferential orientation, half of the smaller Sample A pillars had a similar orientation close to $(hkl) [uvw] = (521) [1-55]$, shown in Fig. 5.2d. There is no correlation between the pillar top orientation and the local substrate orientation, a further indication that the substrate did not recrystallize before embossing.

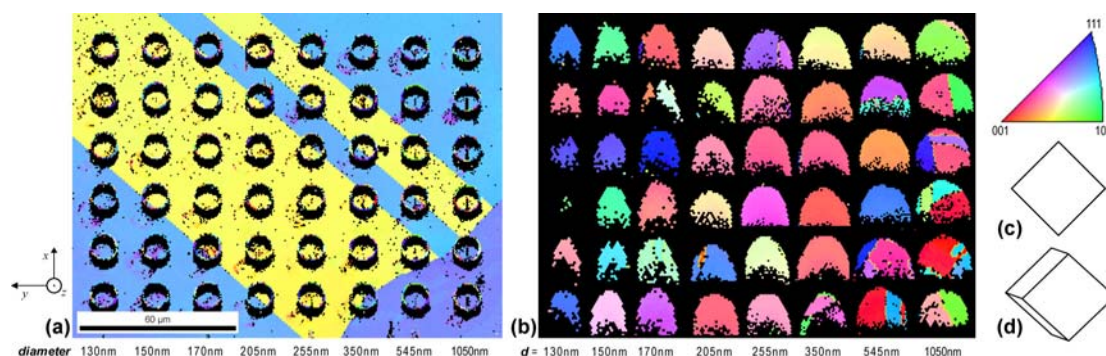


Fig. 5.2. (a) Crystal orientation map giving an overview of Sample A. The pillars are located in the center of the rings. Large diagonal twins are visible in the substrate material, and another grain forms the bottom right region. (b) Maps of the pillar tips before uniaxial compression (various scales). In both (a) and (b) the colors represent the grain orientation relative to the normal direction according to the color key shown in the standard stereographic triangle. Twin boundaries are marked with yellow line segments. (c) Schematic top view of the original plate orientation (100) [011] of Samples A and B before pillar production by embossing. (d) Schematic top view of the most common orientation of the pillars with diameter below $0.5\ \mu\text{m}$, corresponding to (521) [1-55].

5.3.2. Compression tests

A comparison of SEM images and EBSD maps before and after uniaxial compression of the pillars showed several deformation mechanisms. Six examples illustrating the variety of the compression responses are presented in Fig. 5.3. Deformation occurred by dislocation slip (5.3a, 5.3c, 5.3d, 5.3e, 5.3f) and twinning (5.3b, 5.3d). Slip was often concentrated on a single or just a few parallel slip systems, which sometimes corresponded to pre-existing twin boundaries (5.3d). Other pillars showed deformation distributed over the whole pillar, resulting in orientation gradients (5.3c, 5.3f), a phenomenon more frequent in large pillars. The selected pillars of Fig. 5.3 show one dominant deformation mechanism which makes possible a clearer comparison, but it should be noted that most pillars deformed through a combination of multiple mechanisms. To describe the observed deformation phenomena we distinguish between *single slip* (dislocation slip on one or several parallel planes belonging to the same slip system) and *multiple slip* (deformation on non-parallel planes), and we use the terms *localized*, *coarse* (repeatedly localized) and *distributed dislocation slip* to describe how the deformation is concentrated within the pillar volume.

The differentiation between twinning and localized dislocation slip was achieved by EBSD measurements: in case of dislocation slip no abrupt orientation change

between the two sides of the slip was found (see, e.g., 5.3a), while twin formation showed adjacent grains which share a (111) plane and have a misorientation of 60° around [111] (e.g. 5.3b).

The stress-strain response of pillars with diameters below $\sim 0.6 \mu\text{m}$ showed elastic loading segments followed by large discrete strain bursts in which the stress collapses (Figs. 5.3a-5.3c). In contrast, pillars larger than $2 \mu\text{m}$ presented a continuous curve with a gradual transition from elastic to stable plastic deformation (5.3f), which corresponds to the typical plot of polycrystalline bulk samples. Pillars of intermediate size (5.3d, 5.3e) showed transitional behavior with many small strain bursts.

Strain hardening was observed in large pillars; in the plots of Fig. 5.3 it was also enhanced by the use of engineering stress-strain curves, which do not take into account the increase in contact area during compression. Instead, no significant hardening was observed in the submicrometer pillars; unambiguous measurements are, however, difficult to perform due to the large strain bursts.

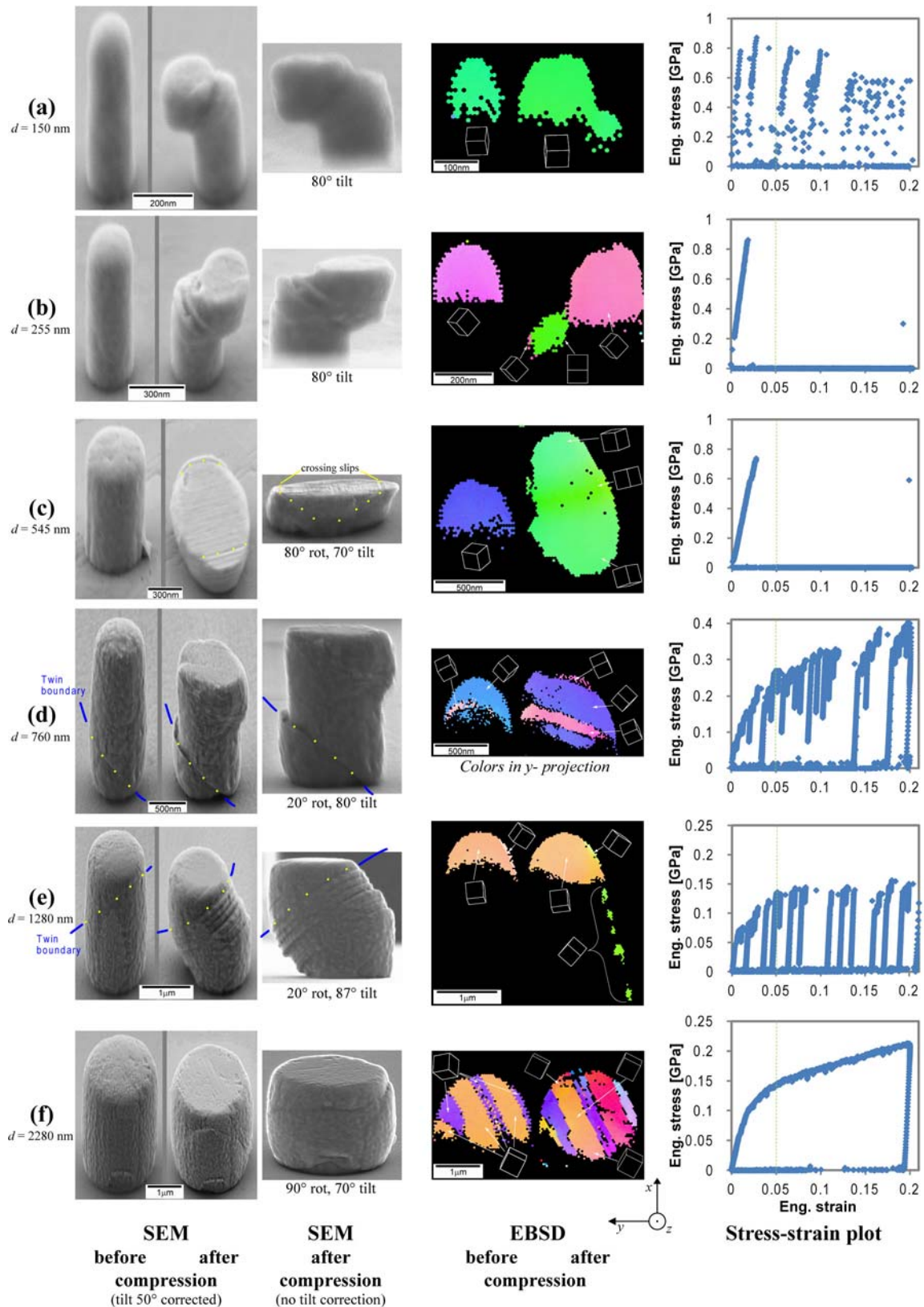


Fig. 5.3. Selected examples of pillars subjected to 20% uniaxial compression strain (a-c from Sample A, d-f from Sample B). Colors in orientation maps relate the normal direction z (pillar axial direction) to the standard stereographic triangle of Fig. 5.2. (a) 150 nm \times 530 nm pillar deformed by localized single dislocation slip. (b) 255 nm \times 720 nm pillar deformed

primarily by twinning. (c) $545 \text{ nm} \times 770 \text{ nm}$ pillar deformed mainly by distributed single dislocation slip. (d) $760 \text{ nm} \times 1850 \text{ nm}$ pillar deformed by localized deformation at a pre-existing twin boundary, in addition to some distributed dislocation slip and twin formation (EBSD map with y -color projection for better contrast among the twins). (e) $1.28 \mu\text{m} \times 2.13 \mu\text{m}$ pillar deformed by coarse single dislocation slip. (f) $2.28 \mu\text{m} \times 2.30 \mu\text{m}$ pillar deformed mainly by distributed multiple dislocation slip.

In order to visualize size effects in the strength, the $\sigma_{0.05}$ values of all 130 pillars investigated were plotted as a function of their initial diameter (see Fig. 5.4). A least squares fitting with a power function (without weighting) was performed, as well as a fitting based on the source-limited model suggested by Von Blanckenhagen *et al.* [21, 22].

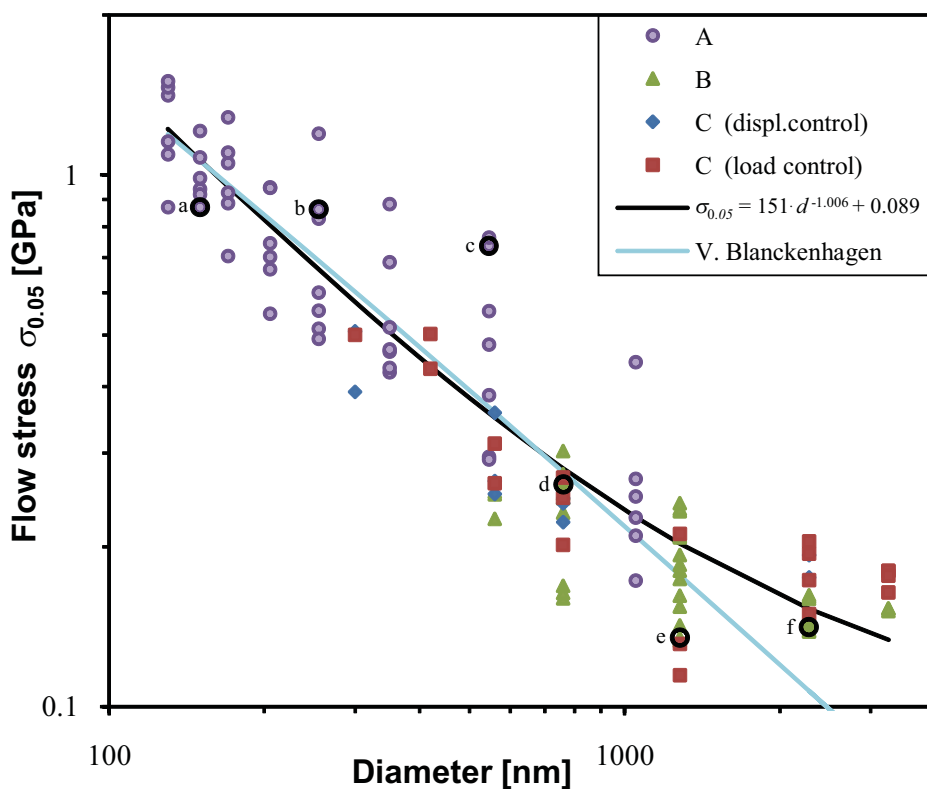


Fig. 5.4. Flow stress $\sigma_{0.05}$ at 5% strain versus pillar diameter d in a log-log representation. The fitting by a power law function is also indicated, as well as the trend obtained with the source-limited model of Von Blanckenhagen *et al.* [21, 22] (see discussion). The values of the pillars shown in Figs. 5.3 a-f are highlighted.

5.4. Discussion

5.4.1. Deformation behavior of single pillars

The mechanical response of the pillars subjected to uniaxial compression showed large variability even in pillars of the same size: deformation was sometimes localized, and sometimes distributed over the whole pillar volume, and it was carried out by dislocation slip with or without twinning. Several parameters play a role in determining which deformation mechanism is being activated, such as diameter, aspect ratio, crystal orientation, and the presence of surface defects, dislocations or grain (twin) boundaries. It is therefore extremely challenging to deduce the mechanism of a single pillar, except for pillars with diameters of 2 μm or larger, which always deformed rather homogeneously. In addition, the stress-strain plot alone is not sufficient to identify the deformation mechanism: a single large strain burst after elastic loading can, for example, be caused by twinning (Fig. 5.3b), dislocation slip distributed over the whole pillar volume (5.3c), or localized dislocation slip (not shown here).

Dislocation slip

Dislocation slip is probably always an active phenomenon during deformation, at least in the rounded top part which becomes flat during compression (where local pressure is higher due to reduced contact area). Dislocation can be localized in one or a few parallel slip planes (5.3a, 5.3e), or it can be distributed over the whole volume, often on parallel slip systems (5.3c, 5.3f). Distributed slip resulted in gradual misorientation within the grains; EBSD orientation analysis showed a maximum misorientation of 14° across the top surface for 5.3c, the gradient being highest in the central region; while sample 5.3f showed up to 20° misorientation within the grains (vertical x direction) and 12° in horizontal y direction (compare sketched local lattice orientations in Fig. 5.3). The orientation gradient is generated by a pile-up of dislocations at crossing slip planes (5.3c, two crossing slip planes marked in the 70° -tilted image), at a twin boundary within the pillar (5.3f), at the interface between pillar and base material, or at the top interface between pillar and flat punch [13]. Orientation gradients were more frequently observed in large pillars with low aspect

ratio, in which only a reduced number of low inclined slip systems enable dislocations to cross the pillar from one side to the other and leave the pillar without piling up. The difference in microstructure between 5.3c (single-crystalline) and 5.3f (polycrystalline) generated a very different stress-strain response: the single crystal showed a single large strain burst after elastic loading up to a very large flow stress, while the polycrystal presented a continuous transition from elastic to stable plastic deformation. Pillar 5.3c was subjected to considerable plastic deformation, larger than the programmed 20% strain, presumably because of the large accumulated elastic energy which was released very fast once dislocation slip occurred, a phenomenon also observed in other high-strength pillars.

Dislocation slip was often observed on parallel planes (single slip), not only in pillars where a certain slip system exhibited a Schmid factor much higher than all others. This phenomenon is clearly visible in pillar 5.3e, where twin boundaries also influenced the activation of the slip systems. In fact, based on the SEM and EBSD images before and after compression (Fig. 5.3e) as well as FIB cross-sections after deformation (see Fig. 5.5c), we infer that the pillar was already composed of two main twins before testing: an upper (orange) grain (with a small side twin not involved in the deformation), and a large (green) twin below it (visible in the EBSD map of Fig. 5.3e only after compression because of the newly exposed surfaces on the right). The activated (111) slip plane is the same in both upper and bottom grains and is parallel to their joint twin boundary and to the thin (orange) twin in the lower (green) grain (Fig. 5.5). The Schmid factor for this system was large (0.47) in both twin members. However, this is not the most convenient slip system for the upper grain, which had a slip system with a Schmid factor close to the ideal value of 0.5 (both slip plane and direction with slope $\sim 45^\circ$), and was only one of the two equivalent systems with Schmid factor 0.47 for the lower grain (only the activated system is highlighted in Fig. 5.5a). Nevertheless, the slip system parallel to the twin boundary between the upper and the lower grain enabled the dislocations to cross the pillar without intersecting any grain boundaries, making this the most favorable slip system. It is possible that the slip system with Schmid factor 0.5 was initially activated. Indeed, dislocation pile-up at the twin boundary would explain the observed initial strain hardening (despite some hardening in the initial deformation stage originating from the reduced contact area), which disappeared once the

unhindered twin-parallel slip system was activated. In general, only pillars with deformation mechanisms hindering each other, such as in 5.3d and 5.3f, showed strain hardening, while this phenomenon was not observed in cases of parallel dislocation slip (5.3a, 5.3e), where no reciprocal dislocation hindering occurs. In silver, parallel slip is also favored by the splitting of mobile dislocations in two partial dislocations relatively distant from each other due to the low stacking fault energy ($\gamma_{st} = 22 \text{ mJ m}^{-2}$ [20]), so that mobile dislocations cannot easily change sliding system before leaving the pillar at the side walls.

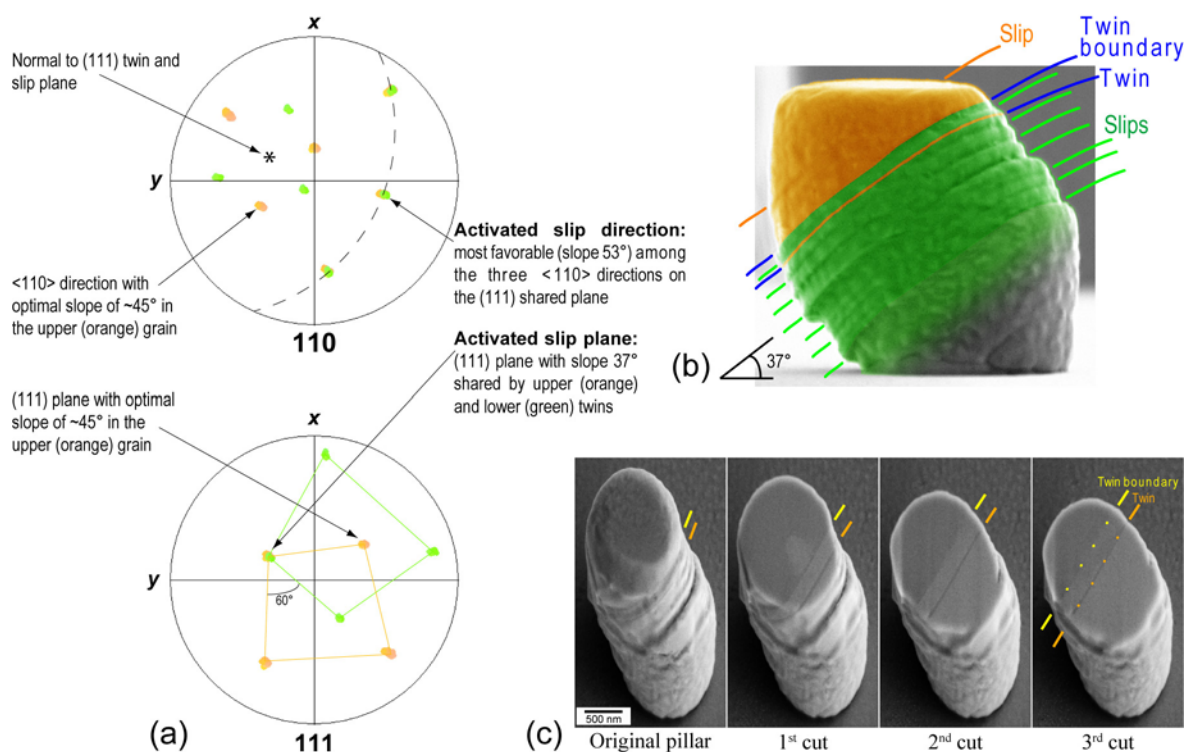


Fig. 5.5. (a) 110 and 111 pole figures of the $1.28 \mu\text{m}$ pillar of Fig. 5.3e, showing the existing $\langle 110 \rangle$ directions and (111) planes in the two main grains after pillar compression. The activated slip system on the (111) plane shared by both grains is indicated, as well as the system with the highest Schmid factor in the upper (orange) twin. (b) Lateral view of the pillar, with the twins colored according to the EBSD map of Fig. 5.3e; the slip planes in both twins, parallel to their twin boundary, are indicated. (c) Sequence of FIB cross-sections showing the twin boundary between the upper twin (orange in (b), on the left) and the bottom one (green in (b), on the right). Besides a single thin parallel twin already observed after the first cut in the bottom grain, no additional twins appear in deeper cuts, confirming that the repeatedly localized deformation is carried out by dislocation slip.

Deformation localized at twin boundaries

In some pillars, such as 5.3d, deformation was localized at favorably tilted ($\sim 45^\circ$) preexisting grain boundaries, which in all investigated cases turned out to be coherent twin boundaries. Further confirmation that they were indeed twin boundaries was obtained by combining FIB cutting with EBSD measurements (example shown in Fig. 5.6). Grain boundary sliding based on diffusion would require very low deformation rates at room temperature, not compatible with the experimental conditions. In addition, diffusion-controlled deformation mechanisms are generally favored for smaller dimensions (e.g. pillar diameter, grain size). For diffusional creep, strength scales proportionally to size. Because of the observed relation of scaling reciprocal to size, diffusion can be ruled out as a rate-limiting mechanism. Another deformation mechanism is therefore proposed, consisting of dislocation slip on the (111) plane forming the twin boundary. Slip on the twin plane is expected to be preferentially activated because the first partial dislocation does not introduce any additional stacking fault, therefore requiring no stacking fault energy, in contrast to slip on other planes. In addition, stress concentration is expected on the boundary plane because of the surface step produced by the boundary (which makes the twin boundary sometimes already visible by SEM in the non-deformed pillar: see Figs. 5.3d, 5.3e), such that the critical shear stress is reached earlier. Preexisting twin boundaries can therefore have a twofold effect on the deformation: if they have a favorable slope close to 45° they facilitate plastic deformation (high Schmid factor), while they hinder the dislocation motion if they are flat or nearly vertical (low Schmid factor, dislocation pile-up).

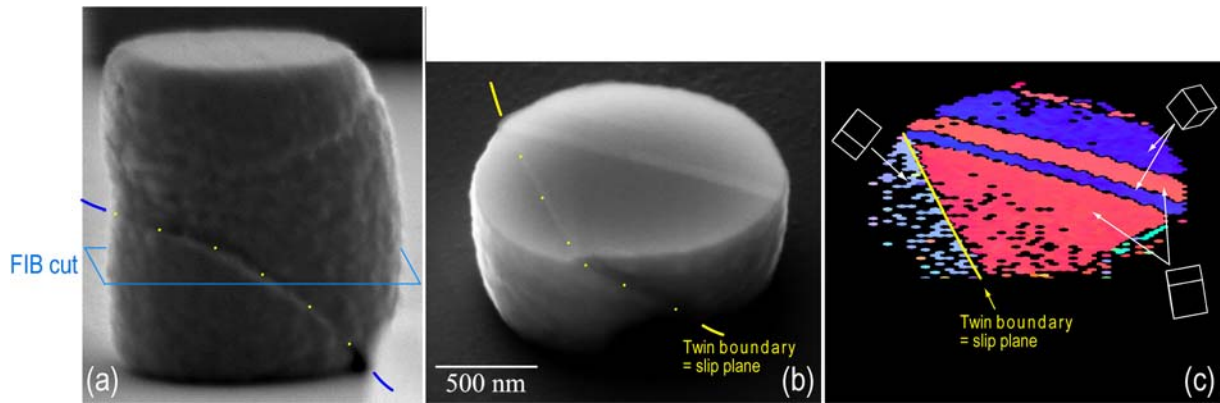


Fig. 5.6. Example of a 1.3 μm pillar in which deformation was localized on a preexisting twin boundary. (a) SEM image of the pillar after uniaxial compression; the slip plane corresponding to the twin boundary is indicated, as well as the FIB section plane. (b) Pillar SEM image after removal of the upper part by FIB cutting and (c) related EBSD map of the FIB-cut surface; some twin boundaries are visible, the left one also corresponding to the slip plane (EBSD map with y color projection for better twin contrast).

Twinning

In addition to dislocation slip, twinning is also a particularly favorable deformation phenomenon in silver because of the low stacking fault energy. The samples already showed twins in both pillars and base material after fabrication. Even if not reported in previous studies on gold nanopillars, this deformation mechanism may be effective in gold as well (its stacking fault energy of 45 mJ m^{-2} [20] is higher than in silver, but this is still a moderate value). Since both dislocation slip and twinning are preferentially on (111) planes, these mechanisms cannot be easily differentiated by geometrical arguments from SEM images (compare e.g. the similar shapes of 5.3a and 5.3b); further, the resulting stress-strain plots may be nearly identical.

Comparison with literature

The magnitude of the strain bursts and the stress reached in submicron pillars before the first burst took place were considerably larger compared to those in FIB-prepared pillars described in the literature [7-9]. In addition, due to the displacement control mode and the rapid load compensation of the indenter machine, the stress was observed to collapse during the bursts, analogous to what is observed in whiskers. Different behavior compared to that in whiskers is, however, observed after the first burst, where whiskers show strain hardening instead of a new elastic loading step

taking place in the embossed pillars. This phenomenon may be explained by dislocation starvation [8] in the considerably smaller pillars investigated here, where dislocations easily reach the pillar surface during a strain burst without interacting with each other and a new source needs to be activated after the previous is depleted. Nevertheless the difference between experiments on whiskers and our pillars may also simply originate from the different testing setup, with compression tests used here instead of tensile tests.

The reason for reduced early plasticity and larger strain bursts compared to those in FIB-prepared pillars may be partially due to the different surface quality, where the embossed pillars have fewer dislocation sources, requiring most dislocations to be nucleated at elevated stresses before plastic deformation can take place. An analogous phenomenon of suppression of sudden pop-in events in nanoindentation tests after FIB milling of surfaces has already been documented by Bei *et al.* [16] in molybdenum alloys, and recently confirmed by the same group [23] by comparing the mechanical response of FIB-prepared pillars and differently pre-strained non-FIB-prepared pillars. The main reason for the observed stress drop probably lies in the faster regulation of the present indenter machine, which could better resolve the stress-strain data during the extremely rapid bursts compared to what is used in displacement-controlled experiments in the literature [7-8].

Some defects, such as dislocations, were certainly introduced during pillar fabrication by embossing, especially in the final cooling step under pressure, in which some deformation took place to compensate for the different coefficient of thermal expansion between silver and silicon. The system examined here is therefore very similar to that of molybdenum pillars subjected to moderate pre-strain recently investigated by Bei *et al.* [14], or to that of whiskers larger than a critical size [2, 5]. The mechanical response of our samples is consistent with these reports: both show a large scattering in strength due to the stochastic presence of defects with variable activation energy, as well as intermediate behavior between a sudden strain burst at theoretical strength (typical of small, dislocation-free pillars) and stable plastic flow, characteristic of large pillars with higher defect densities.

The pillars investigated here were all subjected to similar preparation conditions, but different fabrication parameters would of course lead to dissimilar defect

structures. For example, if no pressure is applied during the cooling step after imprinting, a lower dislocation density leading to higher strengths may be expected. Thus, by controlling the preparation parameters, pillars with optimized properties may be obtained.

5.4.2. Flow strength as a function of pillar diameter

Submicrometer pillars

The correlation of the flow stress ($\sigma_{0.05}$) with the pillar diameter, shown in Fig. 5.4, confirms the frequently-observed trend of increased strength for smaller pillars. The least squares fitting indicates a power relationship very close to $\sigma_{0.05} \sim 1/d$ and approximates well the trend of the submicrometer pillars. The same inverse proportionality on the diameter was observed for tensile tests on whiskers with diameters of a few micrometers [2, 4, 5]. This is a slightly stronger size dependence than that usually observed in uniaxially compressed FIB-prepared pillars, where a proportionality between $d^{-0.4}$ and d^{-1} is reported [7-10]. The differences in the exponent are, however, partially caused by the different fitting methods, such as taking into account an offset corresponding to the bulk strength (89 MPa in our fitting) or the chosen error minimization strategy. In fact, a comparison of embossed silver pillars with FIB-prepared gold samples from the literature [7-9], shown in Fig. 5.7, indicates the same data trend, at least for submicrometer pillars. Silver and gold are very similar metals and are therefore expected to show analogous behavior; even their lattice constant is nearly identical, enabling a reasonable comparison. The slightly higher absolute values of the strength in silver, normalized by the respective anisotropic shear modulus $G_{(111)\langle 110 \rangle}$, are due to a generally larger elastic limit, which indicates a lower density of easily activating dislocation sources in the embossed pillars. Even if for silver a thin oxide layer cannot be completely excluded, this would definitely be thinner than a few nanometers. Otherwise the very surface-sensitive EBSD measurements would not have shown such sharp patterns, which were also observed several months after sample preparation, as already mentioned in Chapter 4.

The inverse size dependence of the strength can be used as a rule of thumb in dimensioning submicron metallic structures produced by embossing. Nevertheless,

the stochastic abundance and activation of defects resulting in considerable scattering of strength requires large test series and a statistical approach such as the Weibull distribution, often used for brittle materials, in order to accurately predict the behavior of structures with these dimensions.

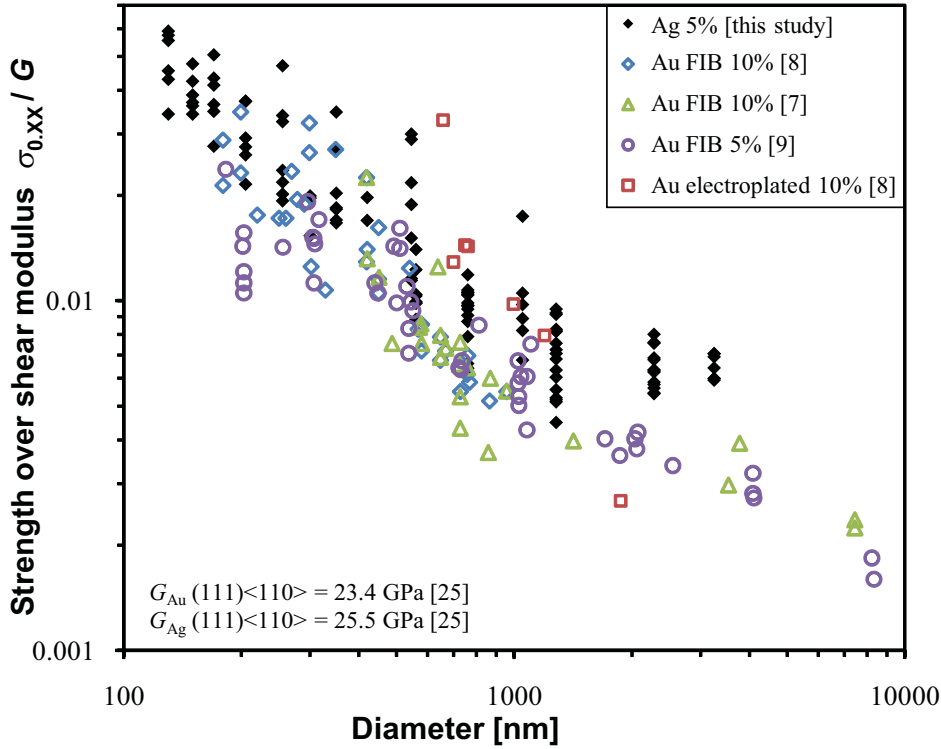


Fig. 5.7. Flow stress at 5% or 10% strain versus diameter normalized to the respective shear modulus G of embossed silver pillars (this study) and FIB-milled gold pillars.

The observed inverse relationship can be explained by the dislocation nucleation model suggested by Von Blanckenhagen *et al.* [21, 22]. The model is based on the Orowan stress [25], an equation indicating that the stress necessary to activate a Frank-Read source is inversely proportional to the distance of the pinning points, i.e.

$$\tau_{\text{cr}} = a G b s^{-1}, \quad (5.1)$$

where a is a constant on the order of unity ($a = 2$ in the original Orowan equation), G is the shear modulus (46 GPa [26]), b is the Burger's vector (2.9 \AA [26]), and s corresponds to the distance between the pinning points.

Brenner [3] already applied this equation in attempting to understand the inverse strength dependence of the whiskers, but observed that for an explanation of the measured strengths the pinning points had to be surprisingly close to each other. He

therefore concluded that dislocations probably nucleate at surface defects. By using the extended form of the Orowan stress, which includes a logarithmic term [27, 28], and assuming a Taylor factor of 3, the normal stress on the pillars according to the model of Von Blanckenhagen *et al.* is given by

$$\sigma_{cr} = \frac{3Gb}{2\pi s} \ln\left(\frac{\alpha s}{b}\right), \quad (5.2)$$

where α is a fitting parameter on the order of unity, which in our fitting was kept fix at $\alpha = 1$.

For small structures it is assumed that the maximum source size is proportional to the smallest structure size, which corresponds to the film thickness h or the pillar diameter d . Von Blanckenhagen *et al.* [22] showed with discrete dislocation dynamic simulations that in thin films the most favorable source size s lies between $h/4$ and $h/3$. Due to differences in geometry and surface conditions (the model is based on thin films on a substrate, with dislocation pile-up at the boundaries, while in pillars one expects easy dislocation escape at the lateral surfaces) we used the source size as a variable in the fitting and obtained the best data approximation for $s = d/4.86$, which is a reasonable value. The model therefore reveals a nearly inverse relationship between flow strength and pillar diameter, describing well the experimental results of the submicron pillars. Von Blanckenhagen and colleagues also indicated that s should be a fraction of either the critical dimension (here the diameter) or the grain size, whichever is smaller. In the polycrystalline pillars larger than $1 \mu\text{m}$ the grain size is nearly constant and smaller than the diameter. By using the grain size for s instead of the diameter, their constant strength over diameter can also be at least qualitatively explained. This phenomenon of nearly constant strength for pillars above $1 \mu\text{m}$ is discussed in more detail in section 4.2.2.

Using a different simulation approach, Tang *et al.* [12] also obtained an inverse dependence of the strength on the diameter, based on dislocation starvation in small pillars due to rapid escape of dislocations through the free surfaces (assuming a constant source density). As this approach also confirms our experimental results, at least qualitatively, no conclusions on the plausibility of one model over the other can be drawn.

The smallest pillars approach the theoretical strength, with values of up to 1.5 GPa, which if multiplied with the Schmid factor correspond to $\sim 1/36$ of the silver anisotropic shear modulus (25.5 GPa [24]). Their strength does not yet deviate from the $1/d$ trend, indicating that the plateau at theoretical strength would probably be reached at pillar diameters of around 100 nm or smaller. Assuming a dislocation density of 10^{12} m^{-2} one expects dislocation-free pillars for sizes below 1 μm , i.e. dimensions ten times larger. The discrepancy probably originates from the fabrication method involving deformation, which is expected to introduce larger dislocation densities and surface defects in the pillars compared to whiskers or pillars produced by selective etching [2-5, 11, 14, 23].

Supermicrometer pillars

A trend change around the theoretical critical diameter of 1 μm was nevertheless observed: the inverse size dependence of the strength disappears and the flow stress becomes almost independent of the pillar size. This phenomenon corresponds to a change in the pillar stress-strain plots, which show a gradual transition from a few large strain bursts, typical for submicron, single-crystalline pillars (Figs. 5.3a-c), towards a smooth transition from elastic to plastic behavior (Fig. 5.3f) characteristic of macroscopic, polycrystalline pillars. The same transition was reported in whiskers, but at diameters one to two orders of magnitude larger [5]. Microindentations on the silver base material near the pillars showed a hardness value of 390 MPa, which corresponds to a strength of 130 MPa (using a Tabor factor of 3). The flow stress at 5% strain is somewhat higher, comparable to the strength of the largest pillars and higher than what was obtained by fitting all data with a single power-law function (89 MPa, see Fig. 5.4). Even if lower bulk strength could be expected for pure silver, one should consider that during fabrication the silver plate was also stressed during the cooling step to compensate for the difference in thermal expansion with the silicon mold, leading to some hardening because of cold-working.

The transition from a $\sim 1/d$ proportionality of the strength towards nearly constant values above a diameter of 1 μm is particularly accentuated in the pillars studied, such that the strength of large pillars clearly differs from that of FIB-milled samples. The transition in the trend may have multiple explanations. (i) In contrast to FIB-

prepared samples, the larger pillars are mainly polycrystalline, with the grain size remaining relatively constant for pillars with diameters between 1 and 3 μm . It could therefore represent the transition from a deformation-controlled mechanism by dislocation starvation for submicrometer pillars to grain-boundary-controlled behavior (Hall-Petch) for larger ones. (ii) The transition is probably accentuated by the low aspect ratio (~ 1 and smaller) of the 2.3 and 3.2 μm pillars (and the 1050 nm pillars of sample A). The pillar deformation is therefore significantly constrained by the substrate and flat punch (boundary conditions), resulting in higher stress and strain hardening. (iii) Finally, the dislocation starvation model would partially explain the slope change even without the change in pillar crystallinity. The basic idea of the model suggested by Greer and coworkers [7] is that in small pillars the dislocations can easily reach the surface, resulting in very low dislocation densities. According to Gilman's description [29] of dislocation multiplication via multiple cross-slip, a minimum dislocation breeding distance is necessary for multiplication, which can be estimated for silver to be approximately 1 μm . For smaller pillars this mechanism is thus not activated. A transition in the deformation behavior from discrete bursts in submicrometer pillars towards stable plasticity with strain hardening in larger pillars may therefore be expected.

5.5. Conclusions

The analysis of uniaxially-compressed silver micro-pillars produced by embossing showed the activation of various deformation mechanisms. In addition to dislocation slip, twinning was often observed, favored by the low stacking fault energy of silver. In some polycrystalline pillars localized deformation along twin boundaries took place, probably by dislocation slip on the (111) plane forming the twin boundary.

The mechanical response is similar to that of FIB-milled pillars, but with a more discrete behavior on the part of the stress-strain responses of submicrometer pillars, which show elastic loading up to larger flow stresses and more extended strain bursts, thus indicating a lower number of dislocation sources, resulting presumably from the different surface quality. The flow strength of submicrometer pillars was found to be inversely proportional to the diameter, comparable to literature data of gold pillars produced by FIB. Despite the variety of the deformation mechanisms observed, the inverse relationship can be successfully explained by models which consider plasticity limited only by the reduced number of dislocations or dislocation sources, as suggested by Von Blanckenhagen *et al.* [21] and Tang *et al.* [12]. Both the very discrete stress-strain behavior and the inverse dependence of strength on the diameter are analogous to what has been observed in whiskers, but the sample dimensions here are one to two orders of magnitude smaller: in embossed pillars the theoretical strength is expected to be reached only for diameters of 100 nm and below. This indicates that pillars produced by embossing have a defect density lying between that of FIB-prepared pillars and that of whiskers or pillars produced by selective etching, and which is comparable to that of large whiskers. Polycrystalline pillars larger than 1 μm instead showed a nearly constant strength, indicating a transition to macroscopic (bulk) behavior with the strength controlled by polycrystal plasticity.

We conclude that the inverse size dependence of the strength can be used as a rule of thumb for dimensioning submicron metallic structures produced by embossing, a process which has high potential for use in large-scale fabrication of metallic microcomponents.

5.6. References

- [1] G. F. Taylor, Phys. Rev. 23 (1924) 655-660.
- [2] S. S. Brenner, J. Appl. Phys. 27 (1956) 12 1484-1491.
- [3] S. S. Brenner J. Appl. Phys. 28 (1957) 9 1023-1026.
- [4] K. Yoshida, Y. Gotoh, M. Yamamoto, J. Phys. Soc. of Japan, 24 (1968) 5 1099-1107.
- [5] M. N. Shetty, J. Phys. Soc. of Japan, 24 (1968) 6 1264-1268.
- [6] M. D. Uchic, D. M. Dimiduk, J. N. Florando, W. D. Nix, Science 305 (2004) 986-989.
- [7] J. R. Greer, W. C. Oliver, W. D. Nix, Acta Mater. 53 (2005) 1821-1830.
- [8] J. R. Greer, W. D. Nix, Phys. Rev. B 73 (2006) 245410.
- [9] C. A. Volkert, E. T. Lilleodden, Phil. Mag. 86 (2006) 5567-5579.
- [10] D. Kiener, C. Motz, T. Schöberl, M. Jenko, G. Dehm, Adv. Eng. Mater. 8 (2006) 11 1119-1125.
- [11] H. Bei, S. Shim, E. P. George, M. K. Miller, E. G. Herbert, G. M. Pharr, Scripta Mater. 57 (2007) 397-400.
- [12] H. Tang, K. W. Schwarz, H. D. Espinosa, Acta Mater. 55 (2007) 1607-1616.
- [13] D. Kiener, C. Motz, G. Dehm, J. Mater. Sci. 43 (2008) 7 2503-2506.
- [14] H. Bei, S. Shim, G. M. Pharr, E. P. George, Acta Mater. 56 (2008) 4762-4770.
- [15] N. A. Fleck, G. M. Muller, M. F. Ashby, J. W. Hutchinson, Acta Metall. Mater. 42 (1994) 2 475-487.
- [16] H. Bei, S. Shim, M. K. Miller, G. M. Pharr, E. P. George, Appl. Phys. Lett. 91 (2007) 111915.
- [17] J. R. Greer, H. Espinosa, K. T. Ramesh, E. Nadgorny, Appl. Phys. Lett. 92 (2008) 096101.
- [18] U. Engel, R. Eckstein, J. Mater. Proc. Tech. 125-126 (2002) 35-44.
- [19] M. Geiger, M. Kleiner, R. Eckstein, N. Tiesler, U. Engel, Annals of CIRP 50 (2001) 445-462.
- [20] L. E. Murr, *Interfacial Phenomena in Metals and Alloys*, Addison-Wesley, Reading, 1975, p. 146.
- [21] B. Von Blanckenhagen, P. Gumbsch, E. Arzt, Model. Simul. Mater. Sci. Eng. 9 (2001) 157-169.

- [22] B. Von Blanckenhagen, P. Gumbsch, E. Arzt, *Phil. Mag. Lett.* 83 (2003) 1 1-8.
- [23] S. Shim, H. Bei, M. K. Miller, G. M. Pharr, E. P. George, *Acta Mater.* 57 (2009) 503-510.
- [24] G. Simmons, H. Wang, *Single crystal elastic constants and calculated aggregate properties: a handbook*, MIT Press, Cambridge, 1970.
- [25] E. Orowan, *Symposium on Internal Stresses in Metals and Alloys*, Inst. Metals, London (1948) 451-453.
- [26] Q. Ma, D. R. Clarke, *J. Mater. Res.* 10 (1995) 4 853-863.
- [27] M. F. Ashby, *Acta Metall.* 14 (1966) 5 679-681.
- [28] A. J. E. Foreman, *Phil. Mag.* 15 (1967) 137 1011-1021.
- [29] J. J. Gilman, *Micromechanics of Flow in Solids*, McGraw-Hill, New York, 1969, p.187.

6. Conclusions and outlook

6.1. General conclusions

6.1.1. Metal nanoimprinting

A process based on metal forming has been developed which is capable of producing microstructures of silver and gold with sizes down to 130 nm and aspect ratios up to 13 over large areas. The lower size limits were determined by the minimal cavity dimension of the molds tested, since the smallest holes were also completely filled; this means that the nanoimprinting technique still has unexplored potential for reproducing further smaller structures (the feasibility of smaller sizes was actually demonstrated, at least for low-aspect-ratio structures, by the accurate reproduction of mold nanoroughness; see Fig. 3.1). Silicon was shown to be an appropriate mold material and generally used, but it was also demonstrated that other materials with sufficient mechanical, chemical and thermal stability can be equally deployed.

Both silver and gold recrystallized during imprinting due to the forming temperature, deployed above the metal recrystallization temperature to achieve maximum formability. In particular, several twins formed, encouraged by the low stacking fault energy of these metals. The tips of small pillars with diameters below 0.5 μm generally consisted of a single grain with a clear preferred lattice orientation, which appeared to depend on both the original grain orientation of the metallic plate and the geometry of the mold pattern. Pillars larger than 1 μm were, in contrast, always polycrystalline. If the imprinting parameters were varied, certain samples showed incomplete filling in some structures, with smooth sloped faces probably corresponding to crystalline faces. The scattering in the filling is attributed to the dependence of the metal formability on the grain orientation, which is only relevant where there are difficult forming conditions, such as in very small structures with high aspect ratio combined with non-optimal imprinting parameters. Appropriate forming parameters were, however, found, minimizing the incidence of this phenomenon. The process is therefore suitable for producing plates with complex

structured surfaces, e.g. in microfluidics or optics, as well as large numbers of microparts.

6.1.2. Suitability for optical applications

The results achieved in terms of structure size and aspect ratio more than met the original fabrication goals of the collaborative INIT metamaterials project. Combined with the excellent uniformity of silver pillars embedded in the dielectric, the samples produced indicate that nanoimprinting is a suitable technique for fabricating two-dimensional optical devices such as metal-containing photonic crystals. The high quality of these devices was demonstrated by the strong resonances obtained in optical reflectance measurements.

6.1.3. Mechanical properties

The room-temperature deformation behavior of micro- and submicrometer imprinted pillars was investigated by uniaxial compression.

Pillars with diameters of 2 μm or above showed a continuous transition from elastic to plastic deformation, with strain hardening and a nearly isotropic deformation. This corresponds to the typical response of macroscopic, polycrystalline metallic samples. In contrast, small pillars with a diameter below 0.5 μm and composed of one or very few grains (twins) presented inhomogeneous (localized) deformation with elastic compression stages alternating with sudden large strain bursts. Pillars of intermediate sizes showed mixed behavior.

A similar transition around the same pillar diameter of $\sim 1 \mu\text{m}$ was also noted in observations of the size dependence of the flow strength. In submicrometer pillars the strength scaled inversely to the pillar diameter, but was nearly size-independent for larger samples. The deformation of the submicrometer pillars has a strong affinity with that of large whiskers, indicating that in both cases the samples contain few preexisting defects, whose stochastic number, position and activation energy define the deformation behavior of the single pillar. In the literature FIB-milled gold pillars have usually shown a similar scaling law for strength, but less inhomogeneous deformation of the single submicrometer pillars. This may be explained by a higher density of surface defects caused by ion milling.

In addition to dislocation slip, which is the ordinary deformation mechanism in ductile metals, deformation twinning was also observed, facilitated by the low silver stacking fault energy. In addition, conveniently-tilted (111) planes corresponding to preexisting coherent twin boundaries were observed to be particularly favorable for localized dislocation slip.

When dimensioning metallic nanostructures having a mechanical function one should therefore consider a much higher strength compared to their bulk counterparts; their strength, at least for samples prepared by nanoimprinting, can be roughly estimated with the size dependence described in this thesis.

6.2. General outlook

It is typical in scientific research that investigations into one open question often throw up several new intriguing questions and unexpected phenomena which themselves require further analysis. The present study was no exception to this, and if every correlated topic meriting further investigation were listed here, this section would risk becoming longer than the conclusions section. But this is also a sign of an interesting research subject.

Regarding the nanoimprinting process, one open question remains the smallest size which can be accurately reproduced by this technique. New e-beam lithography tools at ETHZ (FIRST lab) and EPFL should make possible the fabrication of molds with smaller structures, or other mold fabrication techniques or commercial molds (e.g. nano-porous Al_2O_3) could be tested. The forming parameters may need further optimization to obtain complete filling with smaller, high-aspect-ratio structures. For industrial application, special efforts should be made to increase the processing rate by focusing on a different setup (e.g. applying isostatic pressure). In addition, if the application does not require freestanding structures with very high aspect ratio, attempts should be made to recycle the molds for several imprints. An increased production rate would also supply better statistics for detailed investigation of the texture evolution in the imprinted material and the occasional scattering in the filling of the smallest structures.

A more detailed characterization of the imprinted material is also desirable, since it would lead to a better understanding of small-scale deformation mechanisms at elevated temperatures and of the properties of the obtained structures. In particular, transmission electron microscopy (TEM) and atom probe tomography (APT) should supply valuable information on local material purity in the nanopillars, dislocation density and the potential presence of grain boundaries within the structures, which may have important consequences for optical and mechanical properties.

From the optical point of view, samples with higher aspect ratio should be characterized and their period, shape and pillar dimensions be systematically varied in order to better understand their optical effect. These experiments should generate significant improvements in the simulation of two-dimensional metallo-dielectric periodic structures, facilitating better comprehension of the parameter influences and rapid evaluation of promising designs. The silicon wafer can afterwards be substituted by a composed dielectric with an embedded waveguide, in order to fully exploit the effect of the periodic metallic structures. Once these conditions have been achieved, more sophisticated devices produced by nanoimprinting will also become suitable candidates for detailed investigations where, for example, chiral elements are introduced or the optical properties are locally altered by adding inhomogeneities to the periodicity. It is predicted that the experience gained via these investigations will lead to the design and fabrication of devices with ground-breaking applications, for example in sensing technology.

In the context of mechanical properties, both smaller and annealed pillars (and maybe also samples which were cooled without pressure after imprinting) should be tested; below a certain dimension they are expected to show a size-independent strength corresponding to the theoretical value. The influence of purity on strength and ductility should also be investigated. These results may then be exploited to produce micro- and nanoparts with mechanical properties which are optimally tuned to fit the desired application, this achieved by controlling the purity of the original metallic plate and the possible diffusion of atoms from the mold material.

Appendix

Curriculum Vitae

STEFANO BUZZI

19.06.1979

Via V. Vela 12, 6500 Bellinzona, Switzerland

Email: buzzist@ticino.com

Phone: +41 78 789 67 55

- 01/2005-04/2009 PhD at the Laboratory of Metal Physics and Technology, Department of Materials Science, ETH Zurich, Switzerland. Topic: "Large-scale imprinting of silver submicrometer structures and studies of their optical and mechanical properties"
- 2003-2004 Scientific collaboration at the University of California, Santa Barbara (UCSB), Materials Department. Topic: "Crack reduction in ceramic thin films fabricated by sol-gel for use as buffer layers in superconducting wires"
- 1998-2003 Diploma in Materials Science and Engineering, ETH Zurich, Switzerland. Average marks of 5.6. Diploma Thesis: "Investigation of buffer layers for $\text{CuIn}_x\text{Ga}_{1-x}\text{Se}_2$ solar cells" (Thin Film Physics Group, Institute of Solid State Physics)
- 1994-1998 Scientific Maturity (University entrance), Liceo di Bellinzona. Mark 1st of 66 students

Publications

- S. Buzzi, M. Galli, M. Agio, J.F. Löffler, "*Silver high-aspect-ratio micro- and nanoimprinting for optical applications*", Appl. Phys. Lett. 94 (2009), in press.
- S. Buzzi, M. Dietiker, K. Kunze, R. Spolenak, J.F. Löffler, "*Deformation behavior of silver submicrometer-pillars prepared by nanoimprinting*", Phil. Mag. 89 (2009) 869-884.
- S. Buzzi, F. Robin, V. Callegari, J.F. Löffler, "*Metal direct nanoimprinting for photonics*", Microelectr. Eng. 85 (2008) 419-424.
- S. Buzzi, K. Jin, P.J. Uggowitzer, S. Tosatti, I. Gerber, J.F. Löffler, "*Cytotoxicity of Zr-based bulk metallic glasses*", Intermetallics 14 (2006) 729-734.

Conference contributions

S. Buzzi, F. Robin, V. Callegari, Y. Ekinci, J. F. Löffler, “*Direct Nanoimprinting of Metals*”, International Conference on Micro- and Nano-Engineering (MNE), Copenhagen, Denmark, 2007 (talk).

S. Buzzi, F. Robin, V. Callegari, Y. Ekinci, J. F. Löffler, “*Silver direct nanoimprinting for photonics*”, MicroNanoFabrication Annual Review Meeting, EPF Lausanne, Switzerland, 2007 (invited talk).

S. Buzzi, F. Robin, V. Callegari, Y. Ekinci, J. F. Löffler, “*Silver direct nanoimprinting for photonics*”, Materials Research Society (MRS) Spring Meeting, San Francisco, USA, 2007 (talk).

S. Buzzi, K. Jin, S. Tosatti, I. Gerber, P. J. Uggowitzer, J. F. Löffler, “*Bulk metallic glass formation in Ni-free Zr-based alloys and studies of their biocompatibility*”, European Congress on Advanced Materials and Processes (EUROMAT), Prague, Czech Republic, 2005 (talk).

S. Buzzi, K. Jin, S. Tosatti, I. Gerber, P. J. Uggowitzer, J. F. Löffler, “*Biokompatibilität von Zr-basierten metallischen Gläsern*”, German Society for Materials (DGM) General Assembly, Hanau, Germany, 2005 (poster).

S. Buzzi, K. Jin, S. Tosatti, I. Gerber, P. J. Uggowitzer, J. F. Löffler, “*Electrochemistry and biocompatibility of Zr-based bulk metallic glasses*”, German Physical Society (DPG) Spring Meeting, Berlin, Germany, 2005 (talk).

